

# **Search for supersymmetry in $\sqrt{s} = 13$ TeV p-p collisions using the $\alpha_T$ variable with the CMS detector**

Matthew Citron

Imperial College London  
Department of Physics

A dissertation submitted to Imperial College London  
for the degree of Doctor of Philosophy

The copyright of this thesis rests with the author and is made available under a Creative Commons Attribution Non-Commercial No Derivatives licence. Researchers are free to copy, distribute or transmit the thesis on the condition that they attribute it, that they do not use it for commercial purposes and that they do not alter, transform or build upon it. For any reuse or redistribution, researchers must make clear to others the licence terms of this work.

## Abstract

The search for BSM physics is one of the primary physics objectives of the LHC. This thesis describes the  $\alpha_T$  search for supersymmetry using a dataset of  $12.9 \text{ fb}^{-1}$  collected during the 2016 proton-proton runs by the CMS detector. The search uses a final state containing significant hadronic activity in the form of jets, missing energy, and no leptons or photons. Dedicated dimensionless variables ensure that backgrounds with fake missing energy are mitigated. A detailed description is given of the selections used to mitigate backgrounds while maintaining acceptance to a wide range of signal models and of the techniques used to ensure a robust determination of the residual backgrounds and systematic uncertainties. No evidence for BSM physics is observed and simplified models are therefore used to interpret the results of the search. Stringent new limits are placed on a range of supersymmetric topologies and a procedure to allow the search to be re-interpreted for any BSM physics model is presented.

Additionally, the upgrade of the Level-1 trigger jet and energy sum algorithm is studied. The upgraded trigger hardware is exploited to ensure effective performance in conditions exceeding the design specification of the LHC.



## Declaration

I, the author of this thesis, hereby declare the work contained in this document to be my own. All figures labelled ‘CMS’ are sourced directly from CMS publications, including those produced by the author and have been referenced as such in the figure caption. Figures marked ‘CMS Preliminary’ are sourced from an unpublished or preliminary public document. All figures and studies taken from external sources are referenced appropriately throughout this document.

The studies for the trigger upgrade presented in Chapter 5 are the result of my own work carried out within the UK CMS Trigger group. I have been a major contributor to all areas of the  $\alpha_T$  analysis presented in Chapters 6, 7, and 8 as part of the Imperial College London and CERN SUSY groups. The aspects of the search which were my primary responsibility are the inclusion of the  $H_T$  shape described in Section 7.5 and the statistical interpretations described in Chapter 8. Finally, I have carried out the work to facilitate re-interpretations described in Chapter 9 with a CMS collaborator.

Matthew Citron



## Acknowledgements

Many thanks to all the people I have worked with over the course of the last 3 and a half years. In particular, thanks to Rob Bainbridge for his constant help and support and to my  $\alpha_T$  colleagues Mark Baber, Shane Breeze, Stefano Casasso, Adam Elwood, Lucien Lo, Christian Laner, Bjoern Penning and Alex Tapper. Thanks also to Nick Wardle and Jad Marrouche for all their statistical and L1 jet related help and to my supervisor Oliver Buchmueller for his guidance throughout my PhD. I'm grateful to my fellow PhD students, Louie Corpe, Adinda de Wit, Lucien Lo and Federico Redi for many fruitful discussions. Finally, thanks to my parents for all their patience, support and proofreading.



# Contents

<b>List of figures</b>	<b>xv</b>
<b>List of tables</b>	<b>xxiii</b>
<b>1 Introduction</b>	<b>1</b>
<b>2 Theoretical overview</b>	<b>3</b>
2.1 The standard model . . . . .	3
2.1.1 Gauge symmetries . . . . .	5
2.1.2 Gauge symmetries of the standard model . . . . .	6
2.2 Physics beyond the standard model . . . . .	10
2.3 Supersymmetry . . . . .	11
2.3.1 The minimally supersymmetric standard model . . . . .	12
2.3.2 Natural supersymmetry . . . . .	13
2.3.3 R-parity . . . . .	14
2.3.4 Experimental SUSY signatures at the LHC . . . . .	15
2.3.5 Simplified models . . . . .	16
<b>3 The LHC and CMS experiment</b>	<b>19</b>
3.1 The Large Hadron Collider . . . . .	19
3.1.1 LHC run conditions . . . . .	20
3.2 The CMS detector . . . . .	21
3.3 Tracker . . . . .	23
3.4 Electromagnetic calorimeter . . . . .	24
3.5 Hadronic calorimeter . . . . .	26
3.6 Solenoid magnet . . . . .	27
3.7 Muon system . . . . .	28
3.8 Data acquisition system . . . . .	29
3.8.1 Level-1 trigger . . . . .	29
3.8.2 High Level Trigger . . . . .	31

3.9	Simulation . . . . .	31
<b>4</b>	<b>Reconstruction</b>	<b>33</b>
4.1	Detector reconstruction . . . . .	33
4.1.1	Track reconstruction . . . . .	33
4.1.2	Vertex reconstruction . . . . .	34
4.1.3	Calorimeter reconstruction . . . . .	35
4.2	Physics object reconstruction . . . . .	36
4.2.1	Electron and photon reconstruction . . . . .	36
4.2.2	Muon reconstruction . . . . .	37
4.2.3	Particle Flow . . . . .	38
4.2.4	Pileup estimation . . . . .	41
4.2.5	Isolation . . . . .	41
4.2.6	Isolated tracks . . . . .	42
4.3	Jet reconstruction . . . . .	43
4.3.1	Jet clustering . . . . .	43
4.3.2	Jet energy corrections . . . . .	44
4.3.3	B tagging . . . . .	45
4.3.4	Energy sums . . . . .	46
4.4	Physics objects for the $\alpha_T$ analysis . . . . .	48
4.4.1	Jets . . . . .	48
4.4.2	Photons . . . . .	50
4.4.3	Electrons . . . . .	51
4.4.4	Muons . . . . .	52
4.4.5	Isolated tracks . . . . .	52
4.4.6	Energy sums . . . . .	52
4.4.7	Summary . . . . .	53
<b>5</b>	<b>The Level-1 trigger upgrade</b>	<b>55</b>
5.1	Legacy system and upgrade . . . . .	55
5.2	The time multiplexed trigger architecture . . . . .	56
5.3	L1 jet algorithm . . . . .	58
5.3.1	GCT jet clustering . . . . .	58
5.3.2	TMT jet clustering . . . . .	58
5.3.3	Energy sums . . . . .	61
5.4	Pileup subtraction . . . . .	61
5.4.1	Global $\rho$ subtraction . . . . .	62

5.4.2	Doughnut subtraction . . . . .	62
5.4.3	Seed threshold and zero suppression . . . . .	64
5.4.4	Calibration . . . . .	65
5.5	Jet performance . . . . .	68
5.5.1	Matching efficiency . . . . .	68
5.5.2	Resolution . . . . .	68
5.5.3	Rates and efficiencies . . . . .	70
5.5.4	Summary . . . . .	73
5.6	Cross-trigger study . . . . .	73
<b>6</b>	<b>The <math>\alpha_T</math> search</b>	<b>77</b>
6.1	Backgrounds for hadronic searches . . . . .	78
6.1.1	The QCD multijet background . . . . .	78
6.1.2	Electroweak backgrounds . . . . .	79
6.2	Suppression of the QCD multijet background . . . . .	81
6.2.1	$\alpha_T$ . . . . .	82
6.2.2	$\Delta\phi_{\min}^*$ . . . . .	85
6.2.3	$H_T/\cancel{E}_T$ . . . . .	87
6.2.4	Forward jet veto . . . . .	87
6.3	Preselection . . . . .	88
6.3.1	Kinematic selections . . . . .	88
6.3.2	Event filters . . . . .	88
6.4	Analysis selections . . . . .	90
6.4.1	Hadronic signal region . . . . .	90
6.4.2	Control regions . . . . .	91
6.5	Categorisation . . . . .	92
6.5.1	Categorisation in $n_{\text{jet}}$ . . . . .	93
6.5.2	Categorisation in $n_b$ . . . . .	93
6.5.3	Categorisation in $H_T$ . . . . .	94
6.5.4	Categorisation in $\cancel{H}_T$ . . . . .	94
6.5.5	Summary . . . . .	94
6.6	Trigger strategy . . . . .	95
6.6.1	Hadronic signal and control regions . . . . .	95
6.6.2	Electroweak control regions . . . . .	96
6.7	Summary . . . . .	98

<b>7 Background estimation for the <math>\alpha_T</math> search</b>	<b>99</b>
7.1 Datasets and simulated samples . . . . .	100
7.1.1 Data . . . . .	100
7.1.2 Simulated samples . . . . .	100
7.2 Corrections to simulation . . . . .	101
7.2.1 Pileup reweighting . . . . .	101
7.2.2 Top $p_T$ reweighting . . . . .	101
7.2.3 Lepton and photon scale factors . . . . .	102
7.2.4 B tag scale factor correction . . . . .	102
7.2.5 Trigger efficiency . . . . .	103
7.2.6 Sideband corrections . . . . .	103
7.3 Background estimation . . . . .	104
7.3.1 Electroweak background prediction . . . . .	104
7.3.2 QCD background prediction . . . . .	106
7.4 Systematic uncertainties in the transfer factors . . . . .	109
7.4.1 Variation method . . . . .	109
7.4.2 Closure test method . . . . .	111
7.4.3 Summary . . . . .	116
7.5 Systematics on the $H_T$ modelling . . . . .	119
7.5.1 Validation using control regions in data . . . . .	119
7.5.2 Deriving systematics on the $H_T$ shape . . . . .	121
7.5.3 Inclusion of systematic sources from simulation . . . . .	123
7.6 Summary . . . . .	124
<b>8 Statistical results and interpretation</b>	<b>127</b>
8.1 Likelihood model . . . . .	127
8.2 Results of the fit to data . . . . .	129
8.3 Interpretation . . . . .	134
8.3.1 Procedure for deriving limits . . . . .	134
8.3.2 Signal model contribution and systematic uncertainties . . . . .	135
8.3.3 Upper limits on signal production cross section . . . . .	136
8.4 Summary . . . . .	138
<b>9 Facilitating re-interpretation</b>	<b>139</b>
9.1 Aggregation . . . . .	140
9.1.1 The aggregated region likelihood . . . . .	140
9.1.2 Definition of aggregated regions . . . . .	140

9.1.3	Results using aggregated regions for the $\alpha_T$ analysis . . . . .	141
9.2	Simplified likelihood . . . . .	144
9.2.1	Definition of the simplified likelihood . . . . .	145
9.2.2	Results for the $\alpha_T$ analysis . . . . .	146
9.3	Summary . . . . .	147
<b>10</b>	<b>Conclusions</b>	<b>149</b>
<b>A</b>	<b>Transfer factors</b>	<b>151</b>
	<b>Bibliography</b>	<b>153</b>



# List of figures

2.1	Graphical representation of the production and decay of supersymmetric particles for the simplified models considered in this thesis [21]. . . . .	17
3.1	Schematic layout of the LHC showing the position of the four main detectors as well as the RF systems [29]. . . . .	20
3.2	Integrated luminosity measured online versus day delivered to CMS (blue) and recorded by CMS (orange) during stable beams for p-p collisions at $\sqrt{s} = 13 \text{ TeV}$ [32]. . . . .	21
3.3	Cross section of CMS showing the paths of various particle types through different segments of the detector [33] . . . . .	22
3.4	A quarter cross section of the CMS tracker showing the pixel and strip components [36] . . . . .	24
3.5	A quarter cross section of the CMS muon system showing the DTs in the barrel region ( $ \eta  < 1.2$ ) and the CSCs in the endcap region $1.2 <  \eta  < 2.4$ . RPCs are layered with the DTs and CSCs in the range $ \eta  < 1.6$ to provide an independent but complementary measurement [27]. . . . .	28
3.6	Diagram of the CMS DAQ system showing the data flow from the detector through the L1 trigger and the HLT. The approximate rate into each system as well as the maximum time for a decision are indicated [44]. . .	30
4.1	(a) PV efficiency as a function of the number of associated tracks. (b) PV resolution in the z coordinate as a function of the number of associated tracks for three track $p_T$ scenarios [60] . . . . .	35

4.2	The overall uncertainty in the corrections applied to MC from Equation 4.7 is shown in the orange solid curve. The pileup uncertainty dominates for $p_T < 50\text{GeV}$ while for higher values of $p_T$ the absolute and relative scale dominate [73]. . . . .	46
4.3	Distribution of the CSVv2 discriminator for jets defined using the anti- $k_t$ algorithm in a muon enriched jet sample. The markers correspond to the data. The stacked, coloured histograms indicate the contributions of the different jet flavours in the simulation [75] . . . . .	47
4.4	Distribution of $\cancel{E}_T$ in $Z \rightarrow \mu\mu$ candidate events. The markers show the data while the filled coloured histograms show the breakdown in difference processes for the simulation. The lower panel shows the data/MC ratio including both statistical and systematic uncertainties [76]. . . . .	49
5.1	Comparison of the GCT (left) and TMT architectures (right) showing the flow of information to the final global decision. The colours indicate the data from each bunch crossing [82] . . . . .	57
5.2	A representation of the CMS collaboration logo digitised with the input resolution of the L1 calorimeter trigger up to $ \eta  < 3$ using (a) the legacy system ( $18 \times 14$ pixels) and (b) the TMT ( $72 \times 56$ pixels). . . . .	57
5.3	The $9 \times 9$ veto conditions used to define jets. The inequalities ensure jet energies are not double counted . . . . .	59
5.4	Comparison of the L1 jet finding algorithm with the anti- $k_T$ algorithm using TT inputs. Distributions of $p_T$ and $\eta$ are shown for the leading and fourth jet. . . . .	60
5.5	Dependence of $\rho_{\text{global}}$ on the number of interactions . . . . .	63
5.6	$\Delta R$ distribution between the seed and constituent TTs using data from Run 1 [84]. . . . .	63
5.7	The rings used to sample the local pileup energy density for the doughnut (a) and chunky doughnut (b) pileup subtraction. The median two strips (in energy density) are used in each case. . . . .	64
5.8	Dependence of $\rho_{\text{chunky}}$ on the number of interactions . . . . .	65

5.9	Fitted response for a QCD dijet sample in the range $0 < \eta < 0.75$	67
5.10	Calibrated response in the QCD dijet sample used to derive the calibration factors. The calibration is seen to be effective for the range $p_T^{L1} > \sim 20 \text{ GeV}$ .	67
5.11	Matching efficiencies for jets showing effect of seed and pileup subtraction at low energies for all jets (a) and for the fourth jet (b). In (b) a comparison with the GCT is shown.	69
5.12	(a) Resolution as a function of the number of interactions. (b) Gradients of linear fits to resolution as a function of number of interactions in bins of $p_T^{gen}$	69
5.13	Efficiency as a function of $p_T^{\text{Gen}}$ for (a) a L1 threshold of 150 GeV on the leading jet and (b) a L1 threshold of 100 GeV on the fourth leading jet.	70
5.14	Rate (Hz) against efficiency for (a) L1 leading jet with a threshold of 150 GeV, (b) L1 second leading jet with a threshold of 110 GeV and (c) L1 fourth leading jet with a threshold of 50 GeV.	71
5.15	The dependence of the rate for a threshold of $p_T^{L1} = 30 \text{ GeV}$ on the number of simultaneous interactions	72
5.16	Rate (Hz) against efficiency for (a) L1 $H_T$ and (b) L1 $\cancel{H}_T$ , both with a threshold of 200 GeV	72
5.17	(a) The L1 jet energy compared to offline in early 2016 data for a wide range of jet energies. (b) Resolution for the L1 jet energy compared to offline in early 2016 data for several different pileup scenarios [87].	73
5.18	Efficiency of the dijet selection for hadronic offline requirement $200 < H_T < 300 \text{ GeV}$ and $\alpha_T > 0.65$ in a band of rate of 5.5 to 7.5 kHz	74
5.19	Efficiency of the multijet selection for hadronic offline requirement $200 < H_T < 300$ and $\alpha_T > 0.65$ in a band of rate of 5.5 to 7.5 kHz	75
6.1	The $\alpha_T$ variable inputs and values for three types of event: balanced and well measured jets (left), balanced jets with a mismeasured jet (middle) and well measured jets recoiling against true $\cancel{E}_T$ (right). The solid cones signify the reconstructed jet momentum while the dashed cones represent the true momentum. The calculation of $\alpha_T$ is described in the text.	84

6.2	The $\alpha_T$ distribution observed in data compared to simulation. The statistical uncertainties for the QCD multijet and electroweak backgrounds are represented by the hatched areas. The final bin of each distribution contains the overflow events. The events below $\alpha_T = 0.55$ use unbiased triggers with a loose preselection while events above $\alpha_T = 0.55$ use the signal region triggers and selection. . . . .	85
6.3	The $\Delta\phi_{\min}^*$ variable inputs and values for a mismeasured balanced three jet event. The third jet minimises the $\Delta\phi_i$ and is used to calculate $\Delta\phi_{\min}^*$ as described in the text. . . . .	86
6.4	The $\Delta\phi_{\min}^*$ distribution observed in data compared to simulation for a selection $H_T > 800 \text{ GeV}$ . The statistical uncertainties for the multijet and SM expectations are represented by the hatched areas. . . . .	87
6.5	The $\cancel{E}_T$ filters remove the long tail in the reconstructed $\cancel{E}_T$ caused by detector, reconstruction and beam effects in the data [76]. . . . .	89
6.6	Signal trigger efficiency in the $H_T$ dimension measured with a muon sample for a representative category for each topology. . . . .	97
6.7	Trigger efficiency as a function of photon $p_T$ for an inclusive selection. . . . .	98
7.1	The relative change in the $t\bar{t}/W$ simulation compared to the relative change in the $\mu + \text{jets} \rightarrow (t\bar{t}/W)$ transfer factor when varying the top $p_T$ uncertainty to $+1\sigma$ . . . . .	105
7.2	Expected number of QCD multijet events determined from simulation, binned according to $n_{\text{jet}}$ and $H_T$ , that (a) satisfy and (b) fail the requirement $H_T/\cancel{E}_T < 1.25$ . Also shown in (c) is the transfer factor for QCD multijets from hadronic control to signal region, again determined from simulation. Finally, (d) shows the expected number of electroweak background events ( $V+\text{jets}$ and $t\bar{t}$ , plus other residual non-multijet backgrounds) that fail the $H_T/\cancel{E}_T < 1.25$ requirement, again determined from simulation and binned according to $n_{\text{jet}}$ and $H_T$ . . . . .	107

---

7.3	The QCD yields taken from the simultaneous fit binned according to $n_{\text{jet}}$ and $H_T$ are shown in (a). Shown in (b) is the result of multiplying the observed multijet events predicted in (a) by the translation factor from the sideband to the signal region determined with simulation (shown in Figure 7.2). This gives a data-driven expectation of the quantity of multijet background events in the signal region. Finally, (c), shows the ratio of expected multijet background events in the signal region divided by non-multijet backgrounds. The multijet background is therefore shown to be at the percent level. . . . .	108
7.4	Ratio of the measurement of $R_{H_T/E_T}$ , the pass/fail ratio for the $H_T/E_T$ selection, from data and Monte Carlo in the $\Delta\phi_{\min}^* < 0.5$ sideband in ( $H_T$ , $n_{\text{jet}}$ ) bins. . . . .	109
7.5	Tests in data probing the $\alpha_T$ (top row) and $\Delta\phi_{\min}^*$ (bottom row) extrapolation for each $n_{\text{jet}}$ category (open symbols) overlaid on top of the systematic uncertainty estimates used for each of the seven $H_T$ bins (shaded bands). The symmetric (asymmetric) jet topologies are shown in the left (right) plot. . . . .	113
7.6	Data-driven tests probing the W polarisation effects. These are shown for each $n_{\text{jet}}$ category (open symbols) overlaid on top of the systematic uncertainty estimates used for each of the seven $H_T$ bins (shaded bands). The symmetric (asymmetric) jet topologies are shown in the left (right) plot. . . . .	114
7.7	Data-driven tests probing the use of the $\mu + \text{jets}$ control sample to predict the $Z + \text{jets}$ background for each $n_{\text{jet}}$ category (open symbols) overlaid on top of the systematic uncertainty estimates used for each of the seven $H_T$ bins (shaded bands). The symmetric (asymmetric) jet topologies are shown in the left (right) plot. . . . .	115
7.8	Data-driven tests probing the $Z/\gamma$ ratio for each $n_{\text{jet}}$ category (open symbols) overlaid on top of the systematic uncertainty estimates used for each of the seven $H_T$ bins (shaded bands). The symmetric (asymmetric) jet topologies are shown in the left (right) plot. . . . .	116

7.9 Data-driven tests probing the W and $t\bar{t}$ admixture in each $n_{\text{jet}}$ category (open symbols) overlaid on top of the systematic uncertainty estimates used for each of the seven $H_T$ bins (shaded bands). The symmetric (asymmetric) jet topologies are shown in the left (right) plot. . . . .	116
7.10 The data/simulation distribution against $\mathcal{H}_T$ for an inclusive selection on category and $H_T$ showing the results of a linear fit. A large bias is observed as well as a low p-value for the constant fits. . . . .	120
7.11 The data/simulation distribution against $\mathcal{H}_T$ for example categories and control regions. The large bias in the linear component seen in Figure 7.10 is mitigated. . . . .	122
7.12 The pull distribution of the linear parameter from the flat hypothesis showing no significant bias. . . . .	123
7.13 The pull distribution of the linear parameter from the flat hypothesis across all $H_T$ bins and categories. There are no significant pulls for the $H_T$ binned fits while the $H_T$ inclusive case shows very large pulls as expected.	124
7.14 The distributions of the p-value for the linear fit. . . . .	125
7.15 Expected relative uncertainties per 100 GeV shown for $t\bar{t}/W$ in (a) are consistent with observed uncertainties shown in (b). . . . .	125
7.16 Expected relative uncertainties per 100 GeV shown for $Z_{\text{inv}}$ in (a) are consistent with observed uncertainties shown in (b). . . . .	126
7.17 Simulation derived systematic variations on the $\mathcal{H}_T$ distribution compared to the linear OP data-driven systematic for two representative categories. . . . .	126
8.1 Top panel: event yields observed in data (solid circles) with their associated Poisson uncertainties represented by error bars are compared to SM predictions with associated uncertainties (black histogram with shaded band) from a CR-only fit as a function of $n_b$ and $H_T$ for the monojet topology in the signal region. Bottom panel: the significance of deviations (pulls) observed in data with respect to the SM expectations from the CR-only (red circles) and full fit (blue circles). The pulls are indicative only and cannot be considered independently. . . . .	130



---

9.2 Limit planes shown for both the full signal regions (left) and the aggregated regions (right). . . . .	144
9.3 (a) The value of $q(r)$ for the $\alpha_T$ search derived with the simplified likelihood using the full covariance matrix, derived with the simplified likelihood assuming no correlations between the background yields and derived with the full likelihood. (b) Expected and observed exclusion contours for the $\alpha_T$ search derived with the simplified likelihood using the full covariance matrix, derived with the simplified likelihood assuming no correlations between the background yields and derived with the full likelihood. The colour scale shows the ratio of $r_{95}$ calculated with the simplified likelihood using the full covariance matrix to the value using the full likelihood. . . . .	147
A.1 The $\mu + \text{jets}$ transfer factors as a function of $H_T$ and jet category. . . . .	151
A.2 The $\mu\mu + \text{jets}$ and $\gamma + \text{jets}$ transfer factors as a function of $H_T$ and jet category. . . . .	152

# List of tables

2.1	The fundamental spin-1/2 fermions observed in nature separated into their three generations. Each particle shown also has an antiparticle with opposite charge and identical mass . . . . .	4
2.2	The fundamental spin-1 vector bosons observed in nature and the force which they mediate. . . . .	4
2.3	Chiral supermultiplets in the MSSM [16] . . . . .	13
2.4	Gauge supermultiplets in the MSSM [16] . . . . .	13
4.1	Jet identification requirements. . . . .	50
4.2	Photon identification requirements. . . . .	51
4.3	Electron identification requirements. . . . .	52
4.4	Kinematic selections for physics objects. . . . .	53
6.1	$\alpha_T$ thresholds versus lower bound of $H_T$ bin in units of GeV. For all $H_T$ bins satisfying $H_T > 800$ GeV, no $\alpha_T$ cut is applied. No $\alpha_T$ requirement is imposed in the monojet bins. . . . .	90
6.2	Summary of the lower bounds of the first and final bins in $H_T$ (the latter in parentheses) in units of GeV as a function of $n_{\text{jet}}$ and $n_b$ . Intermediate $H_T$ bins are taken from the values shown in Table 6.1. . . . .	95
6.3	Trigger thresholds of the Level-1 and final PF-trigger decision for the HLT paths for the hadronic signal region. Except for those on $\alpha_T$ , all thresholds are in GeV . . . . .	96

7.1	Sideband corrections for SM backgrounds derived with fit to sidebands in data. . . . .	104
7.2	Summary of the systematics on the transfer factors considered in the analysis, with representatives ranges of uncertainties and the correlation assumed, for the predictions of the $t\bar{t} + \text{jets}$ , $W + \text{jets}$ and $Z \rightarrow \nu\bar{\nu}$ background components. . . . .	118
8.1	Representative magnitudes of systematic uncertainties in the experimental acceptance for a simplified model that assumes the pair production of bottom squarks and their decay to a b quark and a $\chi^0$ . . . . .	136
8.2	Summary of the mass limits obtained for the four classes of simplified models. The limits indicate the strongest observed (expected) mass exclusions for the gluino or squarks, and $\chi_1^0$ [23]. . . . .	138
9.1	To define the aggregated regions for the $\alpha_T$ search the $H_T$ dimension is merged to $\geq 200$ GeV and $n_b$ to two categories of $n_b < 2$ and $\geq 2$ . The merged $n_{jet}$ categories are summarised in this table. Each category is further binned using eight $H_T$ bins with lower bounds from 100 to 800 GeV.	141



# Chapter 1

## Introduction

In the 20th century, great advances have been made in understanding the properties and interactions of the fundamental particles that make up our universe. The standard model (SM) of particle physics provides an extraordinarily successful description of the phenomena that have been observed in a plethora of experiments.

Despite these successes, the SM is known to be incomplete. From a theoretical perspective, the theory cannot provide a description of gravitational interactions on a microscopic scale [1]. In addition, multiple astronomical observations have supported the existence of a weakly interacting dark matter particle that comprises around five times more of the mass in the universe than particles predicted in the SM [2].

Supersymmetry (SUSY) is an additional symmetry between bosonic and fermionic particles that is among the best motivated of theories that can resolve these and other issues of the SM. The features of the SM and SUSY models are detailed in Chapter 2.

The Large Hadron Collider (LHC) is a proton-proton (p-p) collider designed to probe the SM with collisions at the highest ever centre of mass energy (13 TeV). The Compact Muon Solenoid (CMS) detector is among two general purpose detectors designed to provide precise measurements of the energy, position and momenta of the particles produced in these collisions. The LHC and CMS have run successfully at a lower centre of mass energy (7-8 TeV), discovering the Higgs boson and providing the strongest constraints on a range of SUSY models. The LHC and CMS are described in Chapter 3 while the reconstruction of the data collected by CMS is detailed in Chapter 4.

The Level-1 trigger system is a crucial component of the CMS detector, responsible for making the initial decision on whether an event should be recorded for full analysis. As the data taking conditions become more extreme, the hardware and algorithms used

---

by this system must be fully upgraded. The jet finding and energy sum algorithms are particularly important for SUSY analyses. The Level-1 Trigger upgrade is described in Chapter 5.

The  $\alpha_T$  analysis is a search for SUSY using data recorded by the CMS detector. Sensitivity to beyond standard model (BSM) physics requires strong rejection of backgrounds while maintaining acceptance to signal. Experimental signatures of SUSY include significant hadronic activity in the form of jets and significant ‘missing energy’. In Chapter 6, the strategy of the  $\alpha_T$  search is described, which uses dimensionless variables to mitigate the otherwise dominant backgrounds containing fake missing energy. Inclusive sensitivity to a wide range of models is achieved by finely categorising events according to their energy, missing energy, number of jets and number of b tagged jets.

In order to extract a possible signal contribution, the background components passing selection and associated systematic uncertainties must be robustly determined. In Chapter 7, the procedures for determining backgrounds containing true and fake missing energy are detailed. The systematic uncertainties are determined using tests with both data and simulation.

The compatibility of the data with the SM hypothesis is assessed using a maximum likelihood fit as detailed in Chapter 8. As no evidence is observed for BSM physics, the results are interpreted using simplified supersymmetric models which evaluate the reach of the search for different SUSY event topologies.

Finally, the results of searches cannot be interpreted in the plethora of models to which they may be sensitive. A procedure is given to facilitate the re-interpretation of the  $\alpha_T$  search, such that its impact on any BSM physics may be approximated. This procedure is applicable to many searches and is described fully in Chapter 9.

# Chapter 2

## Theoretical overview

In this chapter the current best theory of particle physics, the standard model, is outlined. Outstanding problems are detailed and used to motivate BSM physics and, in particular, SUSY. The features of supersymmetric theories are outlined and the possible experimental signatures which would enable such a theory to be discovered are detailed.

Natural units, Einstein summation convention and Feynman slash notation are used throughout. Electric charges are in units of the charge of the electron.

### 2.1 The standard model

The SM of particle physics is a quantum field theory (QFT) whose excitations correspond to the elementary particles forming all known matter and the mediators of all known forces [3].

The known matter in the universe is composed of spin-1/2 fermions, summarised in Table 2.1. These are split into quarks which carry colour charge (see Section 2.1.2) and leptons which do not. In terms of their quantum numbers, each of the three generations of quarks and leptons vary only in mass from the other generations. The SM contains spinor fields which give rise to these fermions.

The interactions between particles in the universe are mediated by spin-1 bosons, summarised in Table 2.2. The gluon and photon are massless while the W and Z bosons are massive. The mechanism for determining the masses of these particles, discussed in Section 2.1.2, gives rise to a further fundamental spin-0 particle, the Higgs boson.

**Table 2.1:** The fundamental fermions observed in nature separated into their three generations. Each particle shown also has an antiparticle with opposite charge and identical mass [4].

Generation	Leptons			Quarks		
	Particle	Mass	Electric Charge	Particle	Mass	Electric Charge
1	$e^-$	511 keV	-1	u	2.3 MeV	$+\frac{2}{3}$
	$\nu_e$	$\sim 0$	0	d	4.8 MeV	$-\frac{1}{3}$
2	$\mu^-$	105.7 MeV	-1	c	1.275 GeV	$+\frac{2}{3}$
	$\nu_\mu$	$\sim 0$	0	s	95 MeV	$-\frac{1}{3}$
3	$\tau^-$	1.777 GeV	-1	t	173.2 GeV	$+\frac{2}{3}$
	$\nu_\tau$	$\sim 0$	0	b	4.18 GeV	$-\frac{1}{3}$

**Table 2.2:** The fundamental spin-1 vector bosons observed in nature and the force which they mediate [4].

Force	Particle	Mass	Electric Charge
Electromagnetism	$\gamma$	0	0
Weak	$W^\pm$	80.4 GeV	$\pm 1$
	Z	91.2 GeV	0
Strong	g	0	0

The SM contains vector and scalar fields which give rise to the spin-1 and spin-0 bosons respectively.

The symmetries of the SM determine the properties of the particles and their interactions. There are two classes of symmetries:

- Space-time symmetries corresponding to translations and rotations of the space-time coordinates. The SM satisfies the Poincaré group of space-time transformations that define special relativity.
- Gauge symmetries corresponding to transformations of the fields within the SM.

The mechanism by which the gauge symmetries give rise to the properties and interactions of the particles in the SM is detailed in the remainder of this section.

### 2.1.1 Gauge symmetries

The derivation in this section follows that in [5]. Consider a Lagrangian containing a fermionic field,  $\psi$ ,

$$\mathcal{L} = \psi(x)^\dagger (i\gamma^\mu D_\mu - m)\psi(x) = \psi(x)^\dagger (i\cancel{D} - m)\psi(x), \quad (2.1)$$

where  $\psi(x)^\dagger$  is the hermitian conjugate of  $\psi(x)$ ,  $D_\mu$  is the ‘covariant derivative’ and  $\gamma^\mu$  are the Dirac matrices. Consider a local gauge symmetry defined by symmetry operator  $U(x)$  such that

$$\psi(x) \rightarrow U(x)\psi(x), \quad (2.2)$$

$$\psi^\dagger(x) \rightarrow \psi^\dagger(x)U^\dagger(x). \quad (2.3)$$

In the remainder of this section the dependence on  $x$  is implicit. In order to ensure gauge invariance, the covariant derivative must transform as

$$D_\mu \psi \rightarrow UD_\mu U^\dagger U\psi \rightarrow U\psi. \quad (2.4)$$

This may be achieved by introducing a vector gauge field,  $A_\mu$ , such that  $D_\mu = \partial_\mu + igA_\mu$ . To satisfy Equation 2.4, such that the Lagrangian is gauge invariant,  $A_\mu$  must transform under the ‘adjoint action’,

$$A_\mu \rightarrow UA_\mu U^\dagger + \frac{i}{g}(\partial_\mu U)U^\dagger. \quad (2.5)$$

Having introduced this vector field, a new gauge invariant term may be added to the Lagrangian,

$$\mathcal{L} = \psi^\dagger (i\cancel{D} - m) \psi - \frac{1}{4} F^{\mu,\nu} F_{\mu\nu}, \quad (2.6)$$

where  $F^{\mu\nu}$  is the field strength tensor of the vector field,

$$F_{\mu\nu} = -\frac{1}{g} [D_\mu, D_\nu] = \partial_\mu A_\nu - \partial_\nu A_\mu - g [A_\mu, A_\nu]. \quad (2.7)$$

By writing the fields and covariant derivatives in terms of the generators of the group,  $t_a$ , such that  $A_\mu = A_\mu^a t_a$ , the field strength tensor can be written as

$$F_{\mu\nu}^a t_a = (\partial_\mu A_\nu^a - \partial_\nu A_\mu^a - g f_{bc}^a A_\mu^b A_\nu^c) t_a, \quad (2.8)$$

where  $f_{bc}^a$  are the structure constants of the group defined by the commutation of the group generators [6]. Non zero structure constants introduce self interactions of the gauge fields. No gauge invariant term quadratic in  $A_\mu^a$  (mass term) can be added to the Lagrangian and therefore the vector field is massless.

Gauge symmetries of the Lagrangian therefore result in massless vector bosons that are ‘mediators’ of the resultant forces. The properties of the forces depend on the details of the gauge symmetry. In the next section, the gauge symmetries of the SM are discussed.

### 2.1.2 Gauge symmetries of the standard model

The gauge symmetry group of the SM is given by [5]:

$$G_{SM} = SU(3)_c \otimes SU(2)_L \otimes U(1)_Y. \quad (2.9)$$

The  $SU(3)_c$  gauge symmetry is unbroken and therefore the associated ‘strong force’ is mediated by a massless vector boson, the gluon.  $SU(3)_c$  is generated by the eight Gell-Mann matrices which give rise to eight colour charges. The quarks carry a single colour charge, the gluon is doubly charged and all other fundamental particles in the SM are colour singlets. The strong force is short range as the gluon is self-interacting.

The strong coupling constant,  $\alpha_s$ , reduces with energy (asymptotic freedom) making calculations non-perturbative [7]. The energy required to separate colour singlets of quarks is sufficient to generate additional quark/antiquark pairs (hadronisation) and therefore quarks are ‘confined’ into colour singlet hadrons of two (mesons) or three (baryons) quarks. High energy collisions of protons, such as those at the LHC, result in the production of highly collimated emissions of hadrons (jets) due to the liberation of quarks [8].

The gauge symmetry of the electroweak sector of the SM is  $SU(2)_L \otimes U(1)_Y$ . These symmetries lead to the electromagnetic and weak forces mediated by the  $\gamma$  and W/Z bosons respectively.

The Lagrangian for this sector may be written as

$$\mathcal{L}_{Ewk} = \mathcal{L}_{gauge} + \mathcal{L}_{fermion} + \mathcal{L}_{Higgs} + \mathcal{L}_{Yuk}, \quad (2.10)$$

the terms of which are discussed in this section. The weak force distinguishes between left and right-handed chiralities and therefore the fermionic fields are split into  $\psi_{L/R} = (1 \pm \gamma^5)\psi$ . The fermion term may then be written for each of the three generations of quarks and leptons as:

$$\mathcal{L}_{fermion} = i\psi_L^\dagger \not{D} \psi_L + i\psi_R^\dagger \not{D} \psi_R. \quad (2.11)$$

The left-handed fields transform as doublets under the  $SU(2)_L$  symmetry while the right-handed fields are singlets. For the first generations of quarks and leptons  $\psi$  may therefore be written as

$$\begin{aligned} \psi_L &= \begin{pmatrix} u_L \\ d_L \end{pmatrix}, & \begin{pmatrix} \nu_{eL} \\ e_L \end{pmatrix}, \\ \psi_R &= u_R, d_R, & e_R. \end{aligned} \quad (2.12)$$

The generators of  $SU(2)_L$  are  $T^i = \tau^i/2$ , where  $\tau^i$  are the three Pauli matrices. The covariant derivative therefore acts on the left and right-handed components of  $\psi$  as

$$D_\mu \psi_L = (\partial_\mu + igW_\mu^i T^i + ig'YB_\mu) \psi_L \quad D_\mu \psi_R = (\partial_\mu + ig'YB_\mu) \psi_R \quad (2.13)$$

where  $g$  and  $g'$  are the coupling constants of the  $SU(2)_L$  and  $U(1)_Y$  groups respectively,  $W^i$  are the three gauge bosons that couple to the weak isospin,  $T$ , and  $B$  is the gauge boson coupling to hypercharge,  $Y$ . The hypercharge values are chosen such that the sum of the hypercharge and the third component of weak isospin corresponds to the electric charge,

$$Q = T^3 + Y. \quad (2.14)$$

For the gauge section of the Lagrangian, the  $SU(2)_L$  and  $U(1)$  symmetries give rise to two field strength tensors,

$$G_\mu^\nu = \partial_\mu W_\nu^i - \partial_\nu W_\mu^i - g\epsilon^{ijk}W_\mu^j W_\nu^k, \quad (2.15)$$

$$F_\mu^\nu = \partial_\mu B_\nu - \partial_\nu B_\mu. \quad (2.16)$$

This leads to

$$\mathcal{L}_{gauge} = -\frac{1}{4}F^{\mu\nu}F_{\mu\nu} - \frac{1}{4}G^{i\mu\nu}G_{\mu\nu}^i. \quad (2.17)$$

The Lagrangian invariant under these gauge symmetries, however, does not correspond to the observed universe. No mass terms can be included for either the gauge bosons or the fermions while maintaining gauge invariance. As shown in the remainder of this section, such masses must be introduced via the breaking of the electroweak gauge symmetry in the Higgs sector of the Lagrangian.

The Higgs sector of the Lagrangian is given by,

$$\mathcal{L}_{Higgs} = (D^{\mu u}\phi)^\dagger(D_\mu\phi) - V(\phi) \quad (2.18)$$

where the complex scalar field,  $\phi$ , is in the spinor representation of  $SU(2)_L$ . The covariant derivative of  $\phi$  is

$$D_\mu \phi = (\partial_\mu + igW_\mu^i T^i + ig' \frac{1}{2} B_\mu) \phi \quad (2.19)$$

and the potential,  $V$ , is given by

$$V(\phi) = -\mu^2 \phi^\dagger \phi + \lambda \left( \phi^\dagger \phi \right)^2 \quad (2.20)$$

where  $\mu^2$  and  $\lambda$  are positive constants. The potential is minimised for any  $\phi$  satisfying  $\phi^\dagger \phi = \frac{\mu^2}{2\lambda} \equiv v^2/2$ . While the potential satisfies the electroweak gauge symmetry, the minimum will not and may be chosen as

$$\langle \phi \rangle = -\frac{1}{\sqrt{2}} \begin{pmatrix} 0 \\ v \end{pmatrix}. \quad (2.21)$$

From Equation 2.14, the scalar field has zero electric charge and electromagnetism is an unbroken symmetry. The symmetry group has therefore been broken from  $SU(2)_L \otimes U(1)_Y \rightarrow U(1)_Q$ . Taking the unitary gauge to remove unphysical ‘Goldstone bosons’ [9], the scalar field may be expanded around this minima as

$$\phi = -\frac{1}{\sqrt{2}} \begin{pmatrix} 0 \\ v + H \end{pmatrix}. \quad (2.22)$$

The physical W, Z and  $\gamma$  (labelled A) gauge bosons are combinations of the bosons defined above,

$$W^\pm = \frac{1}{\sqrt{2}}(W_\mu^1 \mp iW_\mu^2), \begin{pmatrix} Z_\mu \\ A_\mu \end{pmatrix} = \begin{pmatrix} \cos(\theta_W) & -\sin(\theta_W) \\ \sin(\theta_W) & \cos(\theta_W) \end{pmatrix} \begin{pmatrix} W_\mu^3 \\ B_\mu \end{pmatrix} \quad (2.23)$$

where  $\theta_W \equiv \text{atan}(g'/g)$  is the weak mixing angle. From Equation 2.22 and the first term of Equation 2.18, the masses may be identified as

$$M_W^\pm = \frac{1}{2}gv, M_Z = \frac{gv}{2\cos\theta_W}, M_A = 0 \quad (2.24)$$

The masses of the fermions are derived from the Yukawa term in the Lagrangian,

$$\mathcal{L}_{Yuk} = -\frac{1}{\sqrt{(2)}}(v + H)(f_{mn}e_L^\dagger e_R + h_{mn}d_{Lm}^\dagger d_{Rn}' + k_{mn}u_{Lm}^\dagger u_{Rn}) + \text{hermitian conjugate} \quad (2.25)$$

where  $f_{mn}$ ,  $h_{mn}$  and  $k_{mn}$  are the Yukawa coupling matrices between the different generations. These may be diagonalised via unitary transformations to generate mass terms for the quarks and leptons. The neutrino is massless in the SM as there is no right-handed component. This contradicts the observation of oscillations between neutrino flavours [10], however, extensions which predict non-zero neutrino masses are possible [11].

The same unitary transformations also introduce mixing between quark generations from the terms including covariant derivatives in the Lagrangian. The mixings are summarised in the CKM matrix and occur as no basis of mass eigenstates is simultaneously diagonal for up and down type quarks [12]. Flavour changing interactions between quarks are mediated by the  $W^\pm$  boson while interactions via the  $Z$  and  $\gamma$  bosons are flavour preserving. There are no flavour changing interactions predicted for the leptons.

## 2.2 Physics beyond the standard model

The SM describes the properties and interactions between all known particles. These properties have been measured and the predictions of the SM verified in a multitude

of experiments. However, the theory cannot be complete as there remain fundamental problems which the standard model does not resolve. Several of the largest such problems are described below.

On a theoretical level, a renormalisable theory of gravity cannot be included within the SM [1]. While negligible at electroweak energy scales, quantum gravitational effects become increasingly important as energies approach the planck scale,  $M_{\text{planck}} \sim 10^{18} \text{ GeV}$ .

Measurements from cosmology and astrophysics have highlighted several areas the SM fails to adequately describe Nature. The vacuum energy density of the universe ('cosmological constant'),  $\Lambda$ , may be expected to be approximated by  $M_{\text{planck}}^4$  by dimensional arguments. However, cosmological measurements of  $\Lambda$  imply  $\Lambda/M_{\text{planck}}^4 \sim 10^{-120}$  [13]. This discrepancy is related to the failure to include gravity in a quantum field theory.

Astrophysical observations [2] imply the existence of a weakly-interacting particle (WIMP) that forms the majority of the matter within the universe. The SM has no viable candidates for this particle. In addition, the matter-antimatter asymmetry observed in the universe requires charge-parity violating processes far in excess of those occurring in the SM.

The discovery of the Higgs boson at  $m_h \sim 125 \text{ GeV}$  raises the 'hierarchy problem'. In QFT, the corrections to  $m_h$  are related to the heaviest particle in the theory and therefore one may expect  $m_h \sim M_{\text{planck}}$ . In addition, quantum corrections from SM particles require fine-tuning in the SM to stabilise  $m_h$  (the 'technical hierarchy problem', see Section 2.3.2).

These problems form the motivation for the existence of a BSM physics model that can resolve some or all of the outstanding issues in the SM. SUSY is a particularly well motivated BSM theory that can resolve the hierarchy problem, provide a DM candidate and include a quantum theory of gravity.

## 2.3 Supersymmetry

There are many possibilities for extending the SM, including new particles/interactions, new (internal) gauge symmetries, extra spacial dimensions and/or new space-time (external) symmetries. SUSY is an external symmetry that relates fermions and bosons by extending the Poincaré algebra [14]. The Coleman-Mandula theorem shows that any such extension through new bosonic generators (such as those responsible for Lorentz trans-

formations and translations) forbids non-zero scattering amplitudes [15]. Supersymmetry therefore introduces fermionic generators,  $Q$ , such that (heuristically),

$$Q |\text{Boson}\rangle \sim |\text{Fermion}\rangle \quad Q |\text{Fermion}\rangle \sim |\text{Boson}\rangle. \quad (2.26)$$

Particles connected by the SUSY generator are in ‘supermultiplets’. This generator commutes with all gauge symmetries of the SM and so particles within each supermultiplet have identical electric, weak isospin and colour charges. In addition, the SUSY generator commutes with the mass operator, implying particles within each supermultiplet have identical masses. The supersymmetric partners of the known SM particles, ‘sparticles’, have not been observed and therefore SUSY must be a broken symmetry.

### 2.3.1 The minimally supersymmetric standard model

The minimally supersymmetric standard model (MSSM) is the simplest supersymmetric extension of the SM [16]. The fermions in the SM are ‘chiral’ (left and right-handed pieces transform differently) with two fermionic degrees of freedom per helicity state. The number of bosonic and fermionic degrees of freedom must be equivalent in each supermultiplet and therefore the simplest supermultiplet is the chiral supermultiplet containing the fermion and two real scalar fields.

The gauge bosons in the SM (before electroweak SUSY breaking) are massless spin-1 vector bosons and therefore have two bosonic degrees of freedom (one per helicity state) and can be included in a ‘gauge’ supermultiplet with a spin-1/2 fermionic partner (‘gaugino’).

The SM Higgs does not reside in a single chiral supermultiplet as this introduces a gauge anomaly into the theory [16]. This anomaly may be avoided by including two Higgs chiral supermultiplets with opposite hypercharge. The SM Higgs is a linear combination of the neutral components of these supermultiplets.

The particle content of the MSSM (before symmetry breaking) is summarised in Table 2.3 for the chiral supermultiplets and Table 2.4 for the gauge supermultiplets. The neutral higgs and electroweak gaugino sectors combine to form mass eigenstates labelled

**Table 2.3:** Chiral supermultiplets in the MSSM [16]

Name	spin-0	spin-1/2
squarks, quarks (3 families)	$(\tilde{u}_L \tilde{d}_L)$	$(u_L d_L)$
	$(\tilde{u}_R^*)$	$(u_R^\dagger)$
	$(\tilde{d}_R^*)$	$(d_R^\dagger)$
sleptons, leptons (3 families)	$(\tilde{\nu} \tilde{e}_L)$	$(\nu_L e_L)$
	$(\tilde{e}_R^*)$	$(e_R^\dagger)$
	$(H_u^+ H_u^0)$	$(\tilde{H}_u^+ \tilde{H}_u^0)$
Higgs, higgsinos	$(H_d^0 H_d^-)$	$(\tilde{H}_d^0 \tilde{H}_d^-)$

**Table 2.4:** Gauge supermultiplets in the MSSM [16]

Name	spin-1/2	spin-1
gluino, gluon	$\tilde{g}$	$g$
winos, W bosons	$\tilde{W}^\pm \tilde{W}^0$	$W^\pm W^0$
bino, B boson	$\tilde{B}^0$	$g$

‘neutralinos’ ( $\chi^0$ ), while the charged higgs and electroweak gaugino sectors combine to form ‘charginos’ ( $\chi^\pm$ ). Gravity may also be included in the theory by adding a spin-2 graviton and a spin-3/2 superparticle called the gravitino [16].

The mass scale of the sparticles is dependent on the mechanism of SUSY breaking. As discussed below, naturalness arguments motivate the lightest sparticle masses at the TeV scale.

### 2.3.2 Natural supersymmetry

In the SM, the Higgs mechanism requires couplings to each fermion,  $f$ , of the form  $-\lambda_f f^\dagger f \phi$ . If BSM physics is expected to alter the high energy behaviour of the theory at a scale  $\Lambda_{\text{UV}}$ , the quantum corrections to the Higgs boson mass,  $\delta m_H^2$ , will be

$$\Delta m_H^2 = \frac{|\lambda_f|^2}{8\pi^2} [-\Lambda_{\text{UV}}^2] + \mathcal{O}(\log(\Lambda_{\text{UV}})) \quad (2.27)$$

which is quadratically divergent [17]. The correction is proportional to the size of the coupling of the Higgs to the fermion and is therefore largest for the top quark in the SM. Assuming the cut-off scale is at  $M_{\text{planck}}$ , the quantum corrections must be fine-tuned to  $\sim 30$  orders of magnitude to predict the observed Higgs mass.

In a BSM theory containing complex scalars,  $s$ , the Lagrangian will gain a term  $-\lambda_s |\phi|^2 |s|^2$ . Assuming, for simplicity, each component of the complex scalar has mass  $m_s$ , the correction to the Higgs mass will be

$$\Delta m_H^2 = \frac{\lambda_s}{8\pi^2} [-\Lambda_{\text{UV}}^2] + \mathcal{O} \log(\Lambda_{\text{UV}}), \quad (2.28)$$

If SUSY is a symmetry of nature, each fermion can be related to a complex scalar such that  $|\lambda_f|^2 = -\lambda_s$  and the quadratic divergence is naturally cancelled. In unbroken SUSY, logarithmic divergences also vanish [17]. Experimental observations imply the sparticle masses cannot be equal to their SM partners and therefore an additional SUSY breaking term is required in the Lagrangian. This must be a ‘soft’ breaking, such that  $\lambda_f^2 = -\lambda_s$  still holds to cancel the quadratic divergence. To avoid fine tuning of the logarithmic divergence, the lightest sparticles should have masses around the TeV scale. The LHC provides the first experimental probe of this energy scale.

### 2.3.3 R-parity

The general MSSM ‘super potential’ contains terms which violate baryon number,  $B$ , and lepton number,  $L$ . Such terms lead to predictions of proton decay in the order of seconds. The proton lifetime is constrained experimentally to  $> 10^{34}$  years [18], therefore, to forbid such a process, an extra symmetry called ‘R-parity’ is defined as,

$$R \equiv (-1)^{3(B-L)+2S} = \begin{cases} +1 & \text{SM particles} \\ -1 & \text{superpartners} \end{cases}, \quad (2.29)$$

where  $S$  is the spin [16]. R-parity has several physical implications including a stable lightest supersymmetric particle (LSP). This particle must be electrically and colour-neutral from cosmological constraints. Typically, it is taken to be the lightest neutralino in the MSSM and is an ideal WIMP candidate for DM. In addition, R parity requires that superpartners be formed in pairs in collisions and that each superpartner decays

to another superpartner in a chain that must end with the LSP. The LSP does not interact with any detector and therefore such collisions will produce signatures containing significant momentum imbalance.

### 2.3.4 Experimental SUSY signatures at the LHC

The LHC provides proton-proton collisions at  $\sqrt{s} = 13$  TeV. The sparticles have identical charges under the symmetries of the SM and, therefore, in a generic (natural) MSSM model coloured sparticles may be expected to have the highest production cross-section [19]. Assuming R-parity, these sparticles can be produced through:

- quark-antiquark scattering or gluon fusion to produce a gluino or squark pair
- quark and gluon scattering to produce a squark and gluino
- quark-quark scattering to produce a squark pair.

Each of the sparticles will decay in a chain to the LSP. In the decay, coloured SM particles are produced which will hadronise into jets. The signature produced by such processes will therefore be significant hadronic activity in the form of jets as well as momentum imbalance from the LSP. The energy in the final state and the momentum carried by the LSP are dependent on the masses of the sparticles.

The top makes the largest contribution to the Higgs boson mass divergence. In natural SUSY, the lightest sparticle is expected, therefore, to be the partner of the top. This leads to a signature of multiple top quarks in the final state. As discussed in Section 6.1.2, top quarks decay primarily to a b quark and W boson. The sparticles produced at the LHC may therefore be expected to lead to a final state containing multiple b quarks.

The SM contains processes which produces events with similar signatures to those of hadronic SUSY described above. These are described fully in Section 6.1.2, and, in order to be sensitive to SUSY signals, such background processes must be mitigated and any residual background contributions measured. The search described in this thesis relies on several techniques to mitigate and measure background processes as described in Chapters 6 and 7 respectively.

### 2.3.5 Simplified models

The MSSM contains up to 120 free parameters that affect the production and decay modes of the sparticles. It is therefore not possible to interpret the results of searches for SUSY in the full MSSM. In previous searches for SUSY, the constrained MSSM (the CMSSM), which leaves five free parameters, was used to interpret the results [20]. However, while parametrically simple, the decay chains of sparticles in the CMSSM are complicated, making such interpretations model-dependent.

To evaluate model-independent reach in terms of gluino and squark masses, searches are interpreted using simplified models that are defined by a fixed set of production and decay modes. Simplified models are effective models where the majority of the particle content in the theory are decoupled at high masses. Each of the simplified models considered in this thesis involves the direct pair production of only one sparticle type, which then decays directly to the LSP [21].

The T2 simplified models are simplified versions of squark-antisquark production. Each squark undergoes a two-body decay to a quark and the LSP. In this thesis, direct bottom squark production followed by decay to bottom quark and LSP as well as direct top squark production followed by decay to top quark and LSP are considered.

The T1 simplified models are a simplified versions of gluino pair production. Each gluino undergoes a three-body decay to a quark-antiquark pair and the LSP. In this thesis, decays to top-antitop as well as bottom-antibottom pairs are considered. As the three body decay proceeds via the virtual squark, these models are referred to as gluino-mediated squark production.

Figure 2.1 displays the decay chains for the models considered in this thesis. In the simplified models, the masses of the heavy sparticle and of the LSP are free parameters. The topology of the model is crucial in determining the reach of experimental searches. In cases where the mass splitting is large, the final state typically contains significant momentum imbalance and hadronic energy. If the mass splitting is small, ('compressed' models), the momentum imbalance and hadronic energy are suppressed. Additional phenomena, such as initial/final state radiation (ISR/FSR), where one or more incoming/outgoing partons radiates a jet, may be required for sensitivity to such models.

The simplified models may be used to approximate the impact of searches on a complete theory by determining the relevant simplified topologies contained in the full

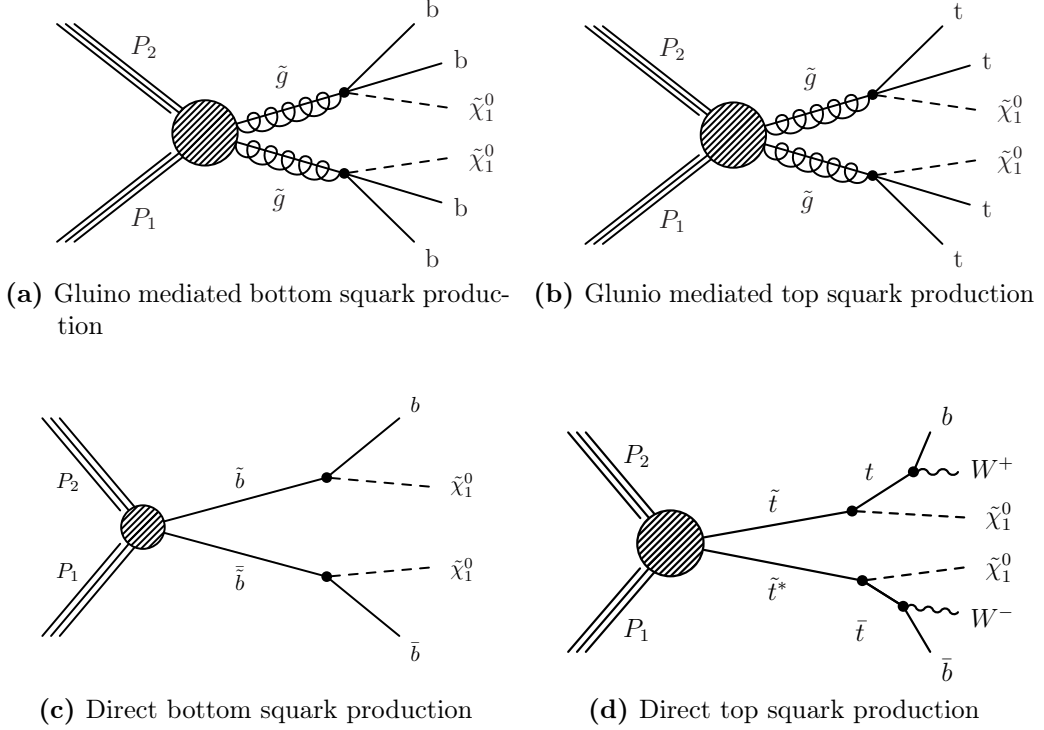


**Figure 2.1:** Graphical representation of the production and decay of supersymmetric particles for the simplified models considered in this thesis [21].

theory. The impact of searches for many different types of signatures may be combined using programs such as FastLim [22].

At the end of the 7 and 8 TeV centre of mass energy runs of the LHC, the furthest gluino mass excluded (see Section 8.3.1) for the gluino mediated top and bottom squark production simplified models was  $\sim 1300$  GeV while for direct top and bottom squark production, the highest squark mass excluded was  $\sim 700$  GeV [23]. As the centre of mass energy increases to 13 TeV, the production cross section for coloured sparticles at the TeV scale jumps by more than an order of magnitude [24], presenting an ideal opportunity for the discovery of TeV scale natural SUSY.



# Chapter 3

## The LHC and CMS experiment

### 3.1 The Large Hadron Collider

The LHC is a 27km circular circumference storage ring, accelerator and collider for both protons and Pb ions. It is situated in a stable environment in a tunnel 100 metres underneath the Franco-Swiss border near Geneva, Switzerland. A double-ring synchotron, it is designed to collide proton-proton pairs with a centre of mass energy of up to  $\sqrt{s} = 14 \text{ TeV}$  and a luminosity of up to  $10^{34} \text{ cm}^{-2} \text{ s}^{-1}$ . This makes the LHC the only collider in operation able to directly probe TeV scale physics.

The injected beams in the LHC are accelerated and stored for each physics run using a 400 MHz superconducting cavity system. The beams of protons or pB ions are merged at four sections around the ring to enable collisions at interaction points. At each of these four interaction points lies one of the four main experiments at the LHC; A Large Ion Collider Experiment (ALICE) [25], A Toroidal LHC Apparatus (ATLAS) [26], the Compact Muon Solenoid (CMS) [27] and Large Hadron Collider Beauty (LHCb) [28] which record the collisions. Figure 3.1 shows the layout of the LHC ring including the positions of the four main detectors. The proton beams are made up of many ‘bunches’ of approximately  $1.1 \times 10^{11}$  protons localised into less than 1 ns (or 30 cm) in the direction of motion. The beams are formed inside the Proton Synchrotron (PS) from bunches of protons 25 ns apart with an energy of 26 GeV. The protons are then accelerated in the Super Proton Synchrotron (SPS) to 450 GeV before being injected into the LHC at the points shown in Figure 3.1. Once injected into the LHC, radio frequency (RF) cavities provide around 275kW of RF power independently to each beam to accelerate the protons to half the operating centre of mass energy for collisions. The LHC operates

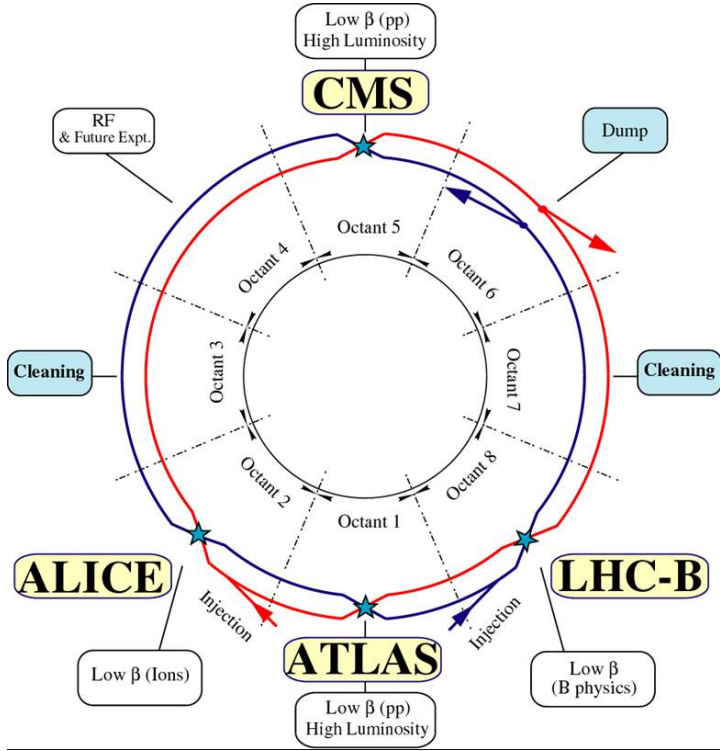


**Figure 3.1:** Schematic layout of the LHC showing the position of the four main detectors as well as the RF systems [29].

as a storage ring for the accelerated beams using 1232 superconducting dipole magnets in the eight arc segments. These provide magnetic fields of up to 8 T to steer the beams. High precision quadropole and higher order magnets at the interaction points are used to position and focus the beams to maximise the occurrence of high momentum collisions and therefore the luminosity. The average number of simultaneous collisions per bunch crossing, in time pileup (PU), for the work in this thesis was  $\approx 25$ . The luminosity in the LHC is not constant over a physics run, but decays due to the degradation of intensities and emittance of the circulating beams (mainly due to loss from collisions). Eventually, the beam is dumped and the acceleration process is restarted.

### 3.1.1 LHC run conditions

The first physics runs of the LHC from 2010 to 2013 (Run 1) reached energies of 3.5 and 4 TeV per beam and provided record-breaking integrated luminosities. The data collected allowed the discovery of the Higgs boson [30, 31] as well as enabling many new regions of parameter space to be probed. From 2013 to mid-2015 (Long Shutdown 1)

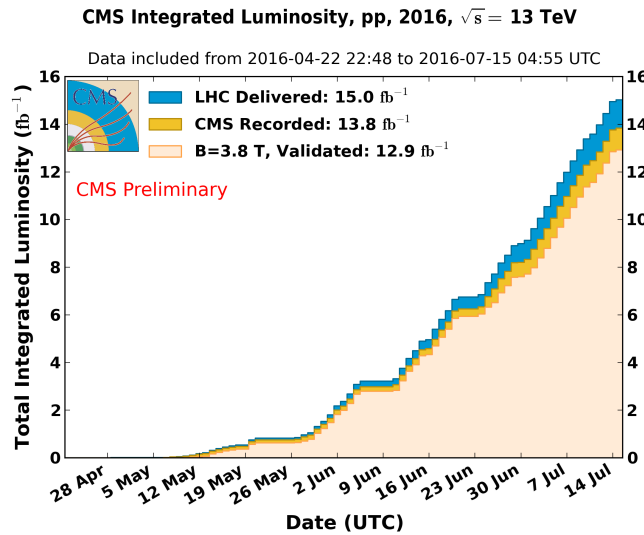


**Figure 3.2:** Integrated luminosity measured online versus day delivered to CMS (blue) and recorded by CMS (orange) during stable beams for p-p collisions at  $\sqrt{s} = 13 \text{ TeV}$  [32].

the LHC was shut down for upgrade to allow design energies to be reached. All magnet interconnectors were inspected and replaced, where necessary, and the dipole magnets underwent a quench training programme.

From 2015 to 2016 (Run 2, which will continue up to 2018) the LHC has been running with record beam energies of 6.5 TeV per beam and bunch spacings of 25 and 50 ns. As shown in Figure 3.2, by July 2016,  $16.0 \text{ fb}^{-1}$  of integrated luminosity was delivered to the CMS and ATLAS detectors, with  $13.8 \text{ fb}^{-1}$  recorded by CMS. The dataset is validated to ensure the exclusion of runs in which the data quality may be affected by detector subsystem. The luminosity of this ‘certified’ dataset is  $12.9 \text{ fb}^{-1}$  and it is this dataset, at a centre of mass energy of  $\sqrt{s} = 13 \text{ TeV}$ , which forms the basis for the work in this thesis.

## 3.2 The CMS detector

The Compact Muon Solenoid (CMS [27]) is one of two general-purpose detectors at the LHC which have performed exceptionally well during the physics runs of the LHC. The main design goals for CMS were to discover the Higgs boson as well as to search for generic models of new physics. To achieve this, CMS provides efficient identification and measurement of physics objects including muons, electrons, photons, taus and hadronic

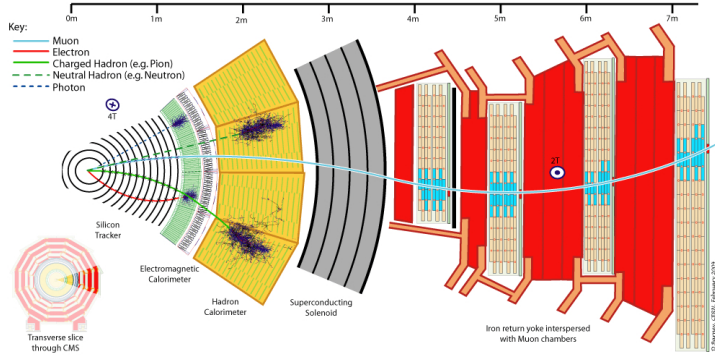


**Figure 3.3:** Cross section of CMS showing the paths of various particle types through different segments of the detector [33]

showers over a wide range of momenta and energies. Each major subsystem is made of a barrel and two endcaps to give coverage of almost  $4\pi$  in solid angle. This barrel design ensures global momentum imbalance can be effectively reconstructed, allowing the missing energy predicted in many new models of physics to be precisely measured. A more detailed description may be found in [27].

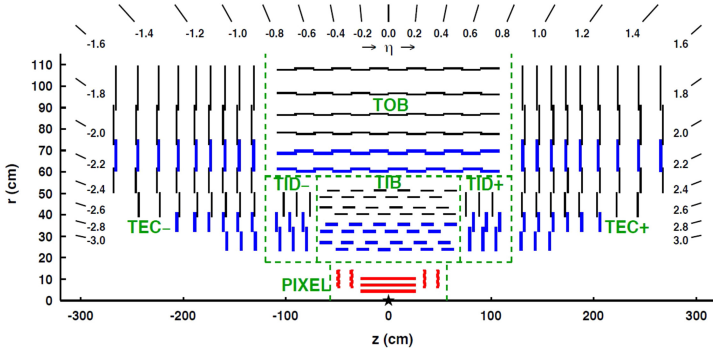
The coordinate system used by CMS takes the origin at the collision point. The z-axis points along the beam direction while the x-axis points radially inward towards the centre of the LHC and the y-axis points vertically upward. The polar angle,  $\theta$ , is measured from the z-axis and defines the pseudorapidity,  $\eta = -\ln(\tan(\theta/2))$ . This is used in preference to  $\theta$  as the difference between the pseudorapidity of two particles is invariant under boosts along the z-axis [29]. The  $\eta$  coverage of CMS is  $|\eta| < 5$ . The azimuthal angle,  $\phi$ , is defined from the x-axis in the x-y plane. This allows the definition of  $\Delta R = \sqrt{\Delta\phi^2 + \Delta\eta^2}$ , commonly used to measure the angular difference between objects. Transverse energies and momenta,  $E_T$  and  $p_T$  respectively, are defined as  $E_T = E \sin(\theta)$  and  $p_T = \sqrt{p_x^2 + p_y^2}$ . Momentum imbalances are measured as the negative vector sums of the momenta of the relevant objects in the x-y plane.

Figure 3.3 shows a cross section of CMS in the x-y plane as well as introducing the major detector components that will be described in detail in this section. The tracker lies closest to the beam and, as for the calorimetry subsystems, is situated within a magnetic field of 3.8T provided by the superconducting solenoid. It measures the curved trajectory of charged particles through this magnetic field to determine their momenta as well as the location of primary and secondary vertices. The tracker is followed by the electromagnetic calorimeter (ECAL), which measures energy deposited in electromagnetic showers from particles such as electrons and photons and is separated

in barrel and endcap components for the central and forward regions respectively. The hadronic calorimeter (HCAL) lies outside the ECAL and measures energy from nuclear interactions of hadronic particles. It is a sampling calorimeter made up of several layers of absorber and scintillator to allow hadron showers to be measured over a maximum of around 11 radiation lengths. The coverage of the hadron calorimeter is extended into the forward regions with the hadronic forward calorimeter (HF). Enclosing the calorimetry and tracking subsystems is the superconducting solenoid which generates the magnetic field. Outside the solenoid, the iron return yoke lies interspersed with muon chambers, forming the outermost components of the detector. Muons are minimally ionising particles (MIPs), depositing little energy within the detector, and typically reach the cavern containing the detector. The barrel muon system is composed of drift-tubes (DT) and resistive plate chambers (RPC). These provide high resolution hit timing and positioning to determine the muon trajectory. In the forward region the DTs are replaced by cathode strip chambers (CSC) which have greater resistance to the higher radiation flux occurring along the beamline.

### 3.3 Tracker

The CMS tracker is an all-silicon tracker with an area sensitive to charged particles of around  $200\text{ m}^2$ . It is designed to measure hits along the curved trajectories of charged particles that result from the high energy p-p collisions. A cross section of the tracker in the  $r$ - $z$  plane is shown in Fig 3.4. The tracker has coverage for  $|\eta| < 2.5$  and achieves an optimal efficiency in the barrel region  $|\eta| < 0.9$  [34, 35]. Close to the interaction vertex,  $r < 20\text{ cm}$ , where the particle flux is maximal ( $10^7/\text{s}$ ), is the pixel detector. This system consists of an inner region of 66 million silicon pixels of  $100\text{ }\mu\text{m} \times 150\text{ }\mu\text{m}$  in three overlapping layers and a forward region with two endcap discs on each side. For  $r > 20\text{ cm}$  the particle flux drops to enable the use of larger silicon microstrips. These range in size from at least  $10\text{ cm} \times 80\text{ }\mu\text{m}$  for the tracker inner barrel (TIB) region at intermediate values of  $r$  ( $20\text{ cm} < r < 55\text{ cm}$ ) to at least  $25\text{ cm} \times 180\text{ }\mu\text{m}$  for the outer barrel (TOB) region ( $55\text{ cm} < r < 110\text{ cm}$ ). The forward region for  $r > 20\text{ cm}$  is covered by endcap disks divided into the 9 disks of the tracker end cap (TEC) for the  $120\text{ cm} < |z| < 280\text{ cm}$  region and 3 tracker inner discs (TID) lying between the TIB and TEC. The TID and first 3 disks of the TEC have sensors of thickness  $320\text{ }\mu\text{m}$  while the remainder of the TEC disks have sensors of thickness  $500\text{ }\mu\text{m}$  [35].



**Figure 3.4:** A quarter cross section of the CMS tracker showing the pixel and strip components [36]

To measure the trajectories the tracker must effectively detect hits from charged particles. The efficiency for the hit reconstruction, defined as the fraction of particles with  $p_T > 1 \text{ GeV}$  passing through the fiducial regions of the sensors in a layer for which hits are recorded, ranges from 99% in the strip detector to 99.5% for the pixel detector. The position resolution for the hits also determines the track finding performance; for the pixel detector the resolution in the  $r\phi$  plane is  $\sim 10 \mu\text{m}$  and  $\sim 20 - 40 \mu\text{m}$  along the  $z$  direction while the  $r\phi$  resolution for the strip detector ranges from  $\sim 13 - 47 \mu\text{m}$ .

### 3.4 Electromagnetic calorimeter

The high precision measurement of the energy and position of electrons and photons resulting from processes such as Higgs boson decay is an important design goal of the CMS experiment. Additionally, a substantial energy fraction of jets, which are central to the analysis outlined in this thesis, is formed of photons whose properties cannot be measured in any other subsystem.

The CMS ECAL is formed of high density lead tungstate ( $\text{PbWO}_4$ ) crystals incorporating an ECAL barrel section (EB) and two ECAL endcaps (EE) outside the tracker [37]. The high density ( $8.28 \text{ g/cm}^3$ ), short radiation length (0.89 cm) and small Moliere radius (2.2 cm) of the crystal are optimal for a compact calorimeter with high granularity. In addition the crystals are radiation hard (up to 10 Mrad) and have a fast scintillation decay time (80% of the light is emitted within 25 ns) comparable to the smallest bunch spacing provided by the LHC.

The EB has an inner radius of 129 cm and covers the range  $|\eta| < 1.479$ . The crystals are arranged into 36 identical ‘supermodules’ which surround the beam line in a quasi-projective geometry (the gaps between crystal modules are offset by  $3^\circ$  with respect to the line from the nominal vertex position) and cover 0.0174 radians in  $\Delta\phi$  and  $\Delta\eta$  [27]. The crystals have a front face cross section of  $\sim 22 \times 22 \text{ mm}^2$  and a length of 230 mm. This allows electrons and photons to deposit most of their energy within a single crystal as the crystals have a depth equivalent to 25.8 radiation lengths and a breadth comparable to the Moliere radius.

The endcaps lie at a distance of 314 cm from the vertex and cover the range  $1.479 < |\eta| < 3$ . The crystals are structured into 2 ‘Dees’ which consist of semi-circular aluminium plates upon which structural units of  $5 \times 5$  ‘superclusters’ of crystals are cantilevered. These are arranged off-axis from the nominal vertex position. The identical crystals have a front face cross section of  $\sim 28.6 \times 28.6 \text{ mm}^2$  and a length of 220 mm (24.7 radiation lengths) [27].

The energy of the incoming electromagnetic particles is measured through the scintillation light produced in the crystals. The light yield of the crystals is reasonably low ( $30\gamma/\text{MeV}$ ) and so photodiodes with intrinsic gain that can operate within a magnetic field must be used to collect the scintillation light and amplify the signal [37]. Silicon avalanche photodiodes (APDs) are used as photodetectors in the barrel region while vacuum phototriodes (VPTs) are used in the endcaps as they are less sensitive to the high radiation conditions in the forward regions. The temperature sensitivity of both the crystals and photodiodes requires a stable temperature of  $\sim 291K$  with a target stability of  $0.1K$ .

The final component of the ECAL is the preshower (ES) which covers much of the endcaps ( $1.653 < |\eta| < 2.6$ ). In addition to its principle aim of identifying neutral pions, it assists in identifying electrons against MIPs and in determining the position of electrons and photons. The preshower is a two layer sampling calorimeter. Each layer consists of a lead radiator that initiates electromagnetic showers (of thicknesses equal to 2 and 1 radiation lengths for the first and second layer respectively) in front of silicon strip detectors, which measure the energy deposited and transverse shower profile [37].

The energy resolution of the ECAL can be parameterised as the summation of three independent sources as shown in Equation 3.1 [38],

$$\frac{\sigma_E}{E} = \frac{a}{\sqrt{E(\text{GeV})}} \oplus \frac{b}{E(\text{GeV})} \oplus c^2, \quad (3.1)$$

where the parameters  $a$ ,  $b$ ,  $c$  are the stochastic, noise and constant contributions respectively. These have been derived from an electron beam test as  $a = 2.8\%$ ,  $b = 12\%$  and  $c = 0.3\%$ . The stochastic term is very low as the shower is mainly contained within each crystal. The noise term is determined mainly by the preamplifier and pileup effects while the constant term originates mainly from intercalibration errors and crystal non-uniformity [37]. In physics runs additional effects due to radiation damage or material upstream of the beam must be controlled to a fraction of a percent [39]. The high resolution achieved by the CMS ECAL allows effective identification and energy measurement of electrons and photons, crucial to controlling electroweak backgrounds in the analysis described in this thesis.

### 3.5 Hadronic calorimeter

The HCAL is a sampling calorimeter which is designed to measure the hadronic properties of jets as well as provide good containment and hermeticity to ensure momentum imbalance from neutrinos or new physics particles can be effectively measured [40]. These quantities are critical for the analysis described in this thesis. The design of the HCAL is largely determined by the space limitations due to the ECAL at  $r = 1.77$  m and the solenoid at  $r = 2.95$  m.

The central region of the HCAL is formed by the HCAL barrel (HB) covering the region  $|\eta| < 1.3$  which sits between the ECAL and magnet. Brass is used as the absorbing material due to its relatively short interaction length (16.42 cm), ease of machining and because it is non-magnetic. The space taken by the active material is minimised through plastic scintillator tiles readout with embedded wavelength-shifting (WLS) fibres [27]. The detector is made up of 36 identical azimuthal wedges split into two barrels. The active scintillator tiles are divided into 2304 segments (towers), each covering  $\Delta\phi \times \Delta\eta = 0.0870.087$ , corresponding to the same area taken by the  $5 \times 5$  ECAL superclusters. The HB is extended to  $1.3 < |\eta| < 3.0$  by the HCAL endcap (HE). This is formed of 14 layers, with the first 6, covering  $|\eta| < 1.74$ , made from towers of

$\Delta\phi \times \Delta\eta = 0.087 \times 0.087$ . For  $|\eta| > 1.74$  the  $\Delta\phi$  size is 0.174 while the  $\Delta\eta$  increases from 0.09 to 0.178.

The hadronic outer (HO) sits outside the magnet in the region  $|\eta| < 1.26$  and is designed as a ‘tail-catcher’. It increases the effective thickness of the HCAL to over 10 interaction lengths, reducing the tails in the energy resolution as well as improving the  $E_T$  resolution. It is composed of iron absorbers and scintillator layers (with the same tile geometry as in the HB), divided into 12 30° sections [40].

Finally, coverage for  $3.0 < |\eta| < 5.0$  is provided by the HF installed 11.2m from the interaction point. This provides excellent measurement of forward hadronic activity as well as hermeticity for  $E_T$  measurements [40]. The HF is composed of a 1.65m thick steel absorber embedded with a grid of 0.6 mm quartz fibres, each separated by 5 mm, running parallel to the beam. The energy is measured using the Cherenkov light produced by particles, formed in the hadronic shower, travelling within the fibres. The HF is segmented into 13 towers in  $\eta$  with a size of  $\Delta\eta \approx 0.175$ , except for the lowest  $\eta$  tower with  $\Delta\eta \approx 0.1$ . The azimuthal segmentation of all towers is  $\Delta\phi = 0.175$ , except for the highest  $\eta$  tower with  $\Delta\phi = 0.349$ .

Similarly to the ECAL, the HCAL resolution was measured using a test beam of single charged pions to be given by the expression shown in Equation 3.2 [41],

$$\frac{\sigma_H}{E} = \frac{94.3\%}{\sqrt{(E)}} \oplus 8.4\%. \quad (3.2)$$

### 3.6 Solenoid magnet

The design specifications of the solenoid magnet are driven by the desire to unambiguously determine the sign of muons with momentum  $\sim 1$  TeV. This requires a resolution of 10% at  $p = 1$  TeV. To achieve this, the CMS experiment uses a niobium-titanium superconducting magnet with a length of 12.5 m and a diameter of 6 m which can operate in fields of up to 4 T. A field of 3.8 T provides sufficient bending power to achieve the design goal and so, to maximise its lifetime, the magnet is typically run at this field strength [27].

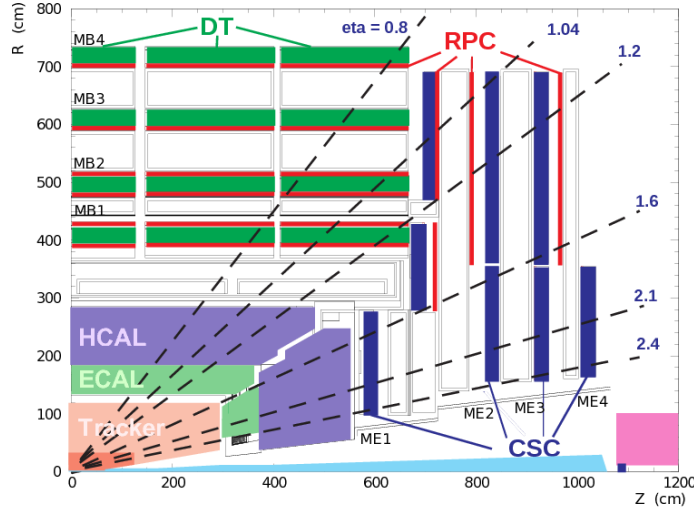


**Figure 3.5:** A quarter cross section of the CMS muon system showing the DTs in the barrel region ( $|\eta| < 1.2$ ) and the CSCs in the endcap region  $1.2 < |\eta| < 2.4$ . RPCs are layered with the DTs and CSCs in the range  $|\eta| < 1.6$  to provide an independent but complementary measurement [27].

### 3.7 Muon system

Effective identification and measurement of muons is critical to the design goals of the LHC and for the analysis described in this thesis. Centrally produced muons are measured three times: in the inner tracker, after the coil and in the return flux. Three types of detectors which rely on gas ionisation are used to identify and measure muons – drift tubes (DTs), cathode strip chambers (CSCs) and resistive plate chambers (RPCs) [27]. DTs are used in the central barrel region of  $|\eta| < 1.2$  where the neutron induced background is small, the muon rate is relatively low, and the magnetic field is low ( $\sim 0.4$  T) and uniform. In the endcap region of  $1.2 < |\eta| < 2.4$  these conditions are reversed and CSCs are used. RPCs are used in both the barrel and endcap region (covering the range  $|\eta| < 1.6$ ) as they provide a fast response with a good time resolution, allowing the bunch crossing to be unambiguously resolved, but much coarser position resolution than the DTs or CSCs [42]. The configuration of the muon systems is shown in Figure 3.5.

The performance of the muon system has been measured using early 7 TeV beam and cosmic muon data [43]. The efficiency of muon reconstruction is typically 96 – 99%. The muon system relies on the effective absorption of charged particles other than muons in the layers of the detectors. ‘Punch through’ of such particles is reduced to  $\sim 5\%$  for the first muon station and to  $\sim 0.2\%$  for further stations. The momentum resolution

was measured as  $\sim 1.8\%$  ( $10\%$ ) for muons of  $p_T = 20 \text{ GeV}$  ( $p_T = 1000 \text{ GeV}$ ) using 7 TeV beam and cosmic muon data.

## 3.8 Data acquisition system

Data acquisition (DAQ) is a major challenge for the CMS experiment as the collision rate far exceeds reasonable processing and storage capabilities that would be required if all data were to be fully reconstructed. It is critical for the CMS physics programme that possible signal events are selected swiftly and efficiently while keeping to constraints placed on data bandwidth, storage and latency. The LHC produces bunch crossings at a rate of up to 40 MHz but can only store  $\sim 1 \text{ kHz}$  for offline analysis [44]. The required rejection power of  $10^4$  is too large to be achieved in a single processing step while maintaining a high efficiency and so the task is split into two stages. The first step, Level-1 trigger (L1 trigger), is a hardware system that uses a small subset of the event information to accept or reject events. The L1 trigger reduces the rate of events which must be completely read from the detector buffers to a maximum of 100 kHz. Even with this reduction, 100 Gbytes/s must be transferred to the surface to be processed by the second step, the High Level Trigger (HLT), which reduces the rate to a peak of  $\sim 1 \text{ kHz}$  which is read to tape to be fully reconstructed. A schematic diagram of the DAQ process is show in Fig 3.6. The selections at both the L1 trigger and HLT steps are designed to optimise efficiency given the constraints of acceptable rate and latency.

### 3.8.1 Level-1 trigger

The L1 trigger system is the first step in selection for all data collected by the CMS detector. The event selection is timed using a local clock synchronised to the LHC bunch collision which initiates the partial readout and processing of detector subsystems and storage of data in the L1 trigger pipelines. The limited pipeline depth restricts the latency for L1 trigger decision to a budget of  $3.2 \mu\text{s}$ , of which  $\sim 2 \mu\text{s}$  must be used for transmission of data [45]. This necessitates the use of fast, high performance electronics and optical links to rapidly reconstruct the event and make the trigger decision. The timing restriction allows only a partial reconstruction using a reduced information set from the calorimetry and muon subsystems only. Dedicated electronics reconstruct physics objects in local regions of the detector that are passed to the global trigger, which

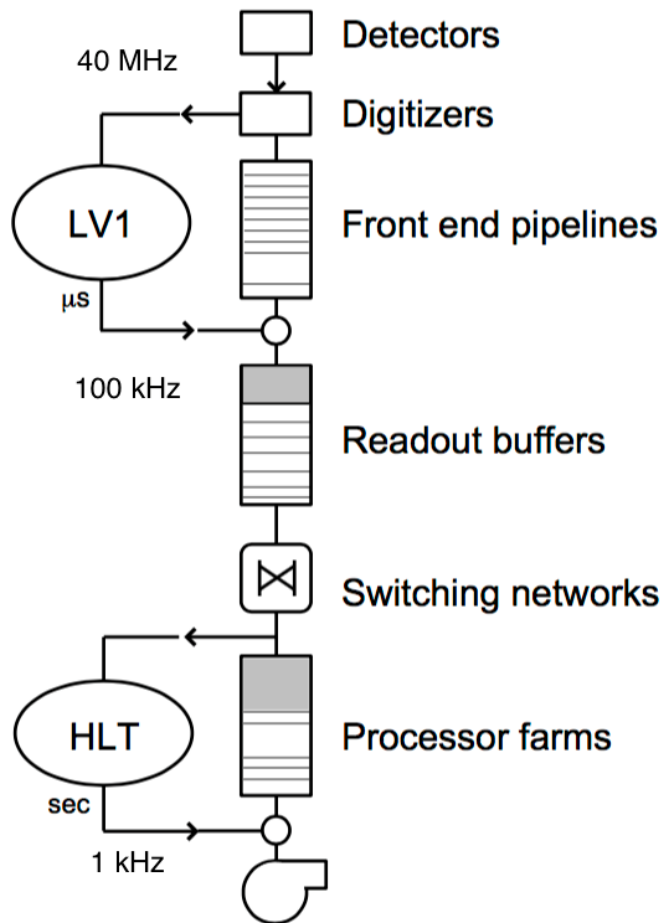


**Figure 3.6:** Diagram of the CMS DAQ system showing the data flow from the detector through the L1 trigger and the HLT. The approximate rate into each system as well as the maximum time for a decision are indicated [44].

constructs global quantities and makes the final trigger decision. The various requirements are known as trigger seeds. If accepted, the event is fully read and transmitted to the final triggering stage. The L1 trigger has undergone two stages of upgrade for the start of Run 2, described in detail in Chapter 5.

### 3.8.2 High Level Trigger

The HLT receives the full detector information read from the CMS detector. It is able to use this to perform a full reconstruction with all detector subsystems, allowing a performance similar to the offline reconstruction. However, though the maximum processing time per event is significantly greater than for the L1 trigger, latency constraints require the use of simplified reconstruction algorithms. The reconstruction is performed using modular trigger paths that each sequentially execute reconstruction and selection criteria [45].

Events which pass the HLT selection are transmitted to the CERN ‘Tier-0’ for permanent storage and reconstruction. The GRID computing infrastructure allows the offline reconstruction and processing to be distributed to dedicated computing sites across the globe [46]. Overall, despite these efforts to reduce data rate, several peta-bytes of data must still be recorded every year for offline analysis, in addition to a similar quantity of simulated events.

## 3.9 Simulation

To confront data from experimental observations with a theoretical hypothesis requires an accurate simulation of both background and signal processes and of their interactions with the CMS detector. This is extremely challenging at the LHC due to the wide range of particle multiplicities and momenta from the p-p collisions, often in non-perturbative regimes. The simulation of events at CMS is factorised into five stages: the hard scattering, fragmentation, hadronisation, decay and detector simulation. A generic review of simulation for particle physics can be found in [47].

The hard scattering models the interaction between the two collision partons. The energy carried by each is sampled from the parton density function depending on the hard-

scatter energy scale [48]. This process is simulated using the PYTHIA8 and MADGRAPH5 generators [49, 50].

The fragmentation and hadronisation is performed using dedicated showering and hadronisation algorithms with generators such as PYTHIA8 or HERWIG [49, 51]. The fragmentation is an iterative process of repeated radiation of soft gluons and quarks performed until the calculation becomes non-perturbative. The particles are then clustered into colourless bound state with different techniques used to connect the colour flow from initial partons to the final state partons, depending on the generator. Unstable particles formed at this stage then undergo further decay. Subsequent  $\tau$  lepton decay is simulated using the dedicated TAULA generator [52]. The particles formed during this stage are referred to as generator level particles.

The simulated background samples are normalised using cross sections calculated with PROSPINO [53] to next-to-leading order (NLO) and next-to-next-to-leading order (NNLO) in  $\alpha_s$ .

The effects of pileup are simulated by combining the generated output with a minimum bias sample with a mean of twenty simultaneous interactions. This is done in a 12 bunch crossing window of the signal event to include the effects of both out-of-time and in-time pileup.

The interactions with the CMS detector of the generated particles must be simulated. For the background processes a full detector simulation is performed using GEANT4 [54], while for the simulated samples the detector response is simulated using the CMS fast simulation package [55].

# Chapter 4

## Reconstruction

The precise measurement of particles produced in the high energy collisions at the LHC is necessary to effectively execute the CMS physics programme. This requires high-precision reconstruction and identification of physics objects in a challenging environment containing large numbers of different particles with a range of energies. The  $\alpha_T$  analysis relies directly on the reconstruction of jets and  $E_T$  for the signal region and on the reconstruction of leptons and photons to reject electroweak backgrounds and to define control regions. This requires the use of information from all detector subsystems and state-of-the-art techniques to allow the reconstruction, selection and calibration of these physics objects.

### 4.1 Detector reconstruction

The first stage in reconstructing the physics objects is to produce the necessary input information from the detector subsystems. This information may be tracks (trajectories) of charged particles or energy measurements from calorimeter depositions. Specialist algorithms that suppress backgrounds, mitigate the effects of pileup and provide high resolution energy, position and/or temporal measurements are used to optimise the precision of the measured quantities over a wide range of particle energies and momenta.

#### 4.1.1 Track reconstruction

Charged particle tracks are reconstructed from the hits, considering the efficiency and resolution, using the iterative combinatorial track finder (CTF) algorithm [56]. The CTF

performs six iterations to determine the tracks. Between each iteration any hits that are assigned to tracks in the previous iteration are removed from the collection. The final track collection is then filtered to remove fake tracks using information on the number of hits, the  $\chi^2$  of the track given the hits, and the compatibility of the track originating from a pixel vertex. The momentum resolution achieved is 0.7 (5)% at 1 (1000) GeV in the central region [56]. Using a dataset of pions and muons from an early run at the LHC the tracking efficiency was measured as 98% for tracks with  $p_T > 500$  MeV and > 99% for tracks with  $p_T > 2$  GeV [57].

#### 4.1.2 Vertex reconstruction

As described in Section 3.1, the LHC produced an average of 25 simultaneous collisions per bunch crossing during Run 2. It is essential to identify the Primary Vertex (PV) and the particles originating from it to allow particles from additional collisions to be rejected and to identify features such as displaced vertices. The tracks are initially clustered using a deterministic annealing (DA) algorithm based on the points of closest approach of the tracks to the beamspot [58]. The candidate vertices containing at least two tracks are then fitted using an adaptive vertex fitter (AVF) to compute the best estimates of vertex parameters [59]. Each track in the vertex is assigned a weight between 0 and 1 corresponding to the likelihood that that track belongs to the vertex. The tracks with weight near 1 are most consistent with the reconstructed vertex while those that are least consistent have small weights. The number of degrees in the fit, defined as

$$n_{dof} = -3 + 2 \sum_{i=1}^{\#tracks} wi, \quad (4.1)$$

is an important parameter for distinguishing real p-p interactions from misclustered vertices as it is strongly correlated with the number of tracks that are compatible with originating at the primary vertex [58]. The vertex position and resolution determined using the AVF have been measured in early LHC data and compared with simulation as shown in Fig 4.1.

The vertices are ordered according to the sum of the  $p_T^2$  of the tracks associated with each vertex and the vertex with the highest  $p_T^2$  taken as the primary vertex (PV). The position of the primary vertex can be used for object identification and rejection of

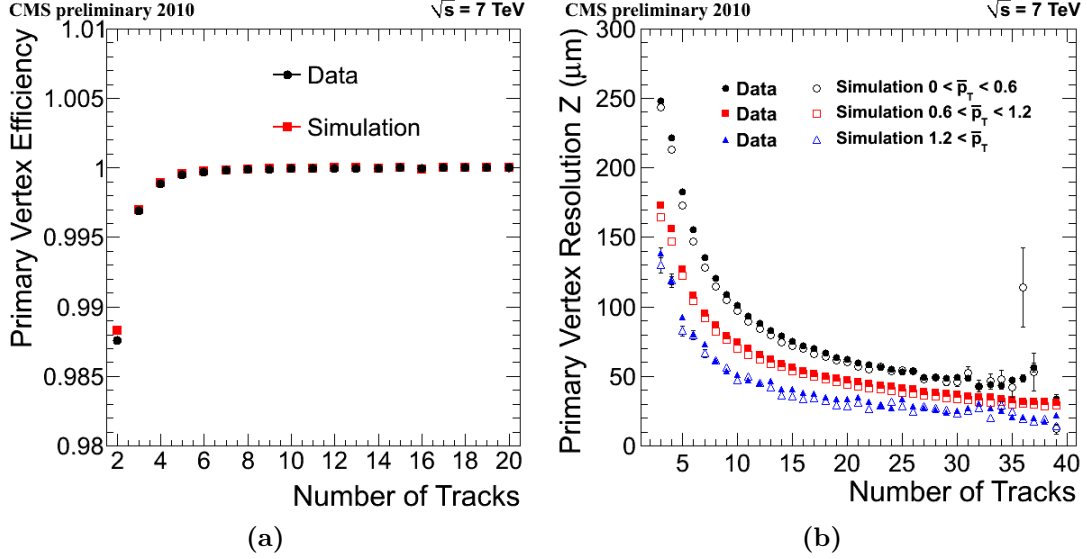


**Figure 4.1:** (a) PV efficiency as a function of the number of associated tracks. (b) PV resolution in the z coordinate as a function of the number of associated tracks for three track  $p_T$  scenarios [60]

pile-up. Many CMS analyses, including the one in this thesis, require that a good vertex is reconstructed from the tracks satisfying:

- a minimum number of degrees of freedom:  $n_{dof} > 4$
- the collision to occur with  $|z| < 24 \text{ cm}$  such that the primary vertex is near the interaction point in the longitudinal direction
- the collision to occur within a radial distance of  $|d_{xy}| < 24 \text{ cm}$  from the beamline

### 4.1.3 Calorimeter reconstruction

The calorimeters reconstruct the energies of incident particles from deposits made in the various subsystems. These deposits must be clustered and the measurement calibrated to provide details of the energy, position and timing of the incident particle. For neutral particles, the calorimeter subsystems provide the only measurement of the particle properties. For charged particles, the measurement complements that from the tracker and provides necessary redundancy in the case of track misreconstruction.

The ECAL crystals are calibrated with both absolute and relative calibrations. Nine EB superclusters and 500 EE crystals are calibrated using high energy electron beams to achieve a resolution of 0.5% (1%) for the EB (EE) components [38]. The remainder

undergo relative intercalibrations to achieve a resolution of 1.4% to 1.8% ( $\sim 5\%$ ) for the EB (EE) components. During LHC runs, the response of the crystals changes due to radiation-induced crystal-lattice defects that absorb the scintillation light. The crystal transparency is monitored to allow the impact on energy measurements to be assessed and corrected [38].

The HCAL components undergo a similar calibration to the ECAL crystals. Firstly a subset of the components are calibrated with a 50 GeV pion beam, which is then extended to the remainder of the subsystem using a Co source [41]. Additional corrections for the HCAL component are derived during LHC running [61].

## 4.2 Physics object reconstruction

The reconstructed tracks and calorimeter deposits form the inputs used to reconstruct particles and jets. These ‘physics objects’ form the basis of the selections used by many analyses. A combination of dedicated local reconstruction algorithms as well as the global event Particle Flow (PF) algorithm, described in Section 4.2.3 are used in reconstructing the physics objects. This section describes the reconstruction of muons, electrons and photons. The reconstruction of jets is described in Section 4.3. The reconstruction of the  $\tau$  lepton physics object, not used for the  $\alpha_T$  analysis, is detailed in [62].

### 4.2.1 Electron and photon reconstruction

Photons and electrons interact in a similar manner within the ECAL and therefore similar reconstruction techniques are used for both objects. Electrons are reconstructed by matching information in the tracker and ECAL using two complementary techniques, an ECAL-driven reconstruction described in this section (identical, aside from tracking requirements, to the photon reconstruction) and a tracker-driven reconstruction performed with the PF algorithm (see Section 4.2.3) which is optimal for low  $p_T$  electrons.

In the ECAL, both electron and photon candidates are formed by clustering energy deposits from electromagnetic showers. Around 50% of the photons convert into an electron-positron pair in the material traversed before reaching the calorimeter, leaving an energy deposit that is widely spread in  $\eta$  and  $\phi$  [63]. For unconverted photons, the deposits are fairly localised in  $\eta$  and  $\phi$ . Electrons radiate bremsstrahlung along their

trajectories due to the presence of the magnetic field and lose on average 33% of their energy in the central region and up to 86% at  $|\eta| = 1.4$ . Their energy deposits are widely spread in  $\phi$  but narrow in  $\eta$ . The hybrid clustering algorithm exploits this characteristic to reconstruct high energy electrons and photons in the barrel and endcap. The hybrid algorithm uses a seed crystal and clusters up to ten dominoes of  $1 \times 3$  or  $1 \times 5$  crystals ( $\phi \times \eta$ ) within  $\Delta\phi < 0.3$  from the seed. Any domino with an energy under 100 MeV is discarded. The dominoes are themselves clustered in  $\phi$ , provided each disconnected subcluster has a seed domino of energy  $> 350$  MeV. The combination of these subclusters is referred to as a supercluster. The reconstruction in the endcap follows a similar procedure using  $5 \times 5$  grids of crystals.

Superclusters that can be associated to tracks originating from the primary vertex are reconstructed as electrons. As electrons lose energy through the non-Gaussian bremsstrahlung process, the Kalman filter is inappropriate and so the specialist track reconstruction Gaussian-sum filter (GSF) algorithm is used. This allows the total energy of electrons to be reconstructed, including the component lost through bremsstrahlung. The photons are identified through inverting the track matching criteria of the supercluster. In the endcaps, additional information is used from the preshower when reconstructing the energy.

Additional selections are applied on all reconstructed electrons and photons to suppress backgrounds. For electrons these are mainly composed of misreconstructed jets, secondary electrons from photon conversions and semi-leptonic decays of heavy quarks. As electrons are mainly contained within the ECAL, a threshold on the ratio of energies in the ECAL and HCAL provides a strong veto of hadronic backgrounds. In addition, requirements are made on the matching track impact parameters such that the transverse distance from the primary vertex is  $d_{xy} < 0.0261$  ( $d_{xy} < 0.118$ ) and the longitudinal distance is  $d_z < 0.041$  ( $d_z < 0.822$ ) for the barrel (endcap). Several variables that rely on the shower shape and cluster width are used to reject fakes, including  $\sigma_{inj\eta}$  (the second moment of the log-weighted distribution of crystal energies calculated in the  $5 \times 5$  matrix around the most energetic crystal). The value of  $\sigma_{inj\eta}$  allows background processes to be rejected as its value is larger on average for neutral meson decay to two collimated photons.

#### 4.2.2 Muon reconstruction

As muons are MIPs they leave minimal energy deposits in the calorimetry subsystems and travel through the entire detector. The muons are reconstructed using a combination

of the inner tracker and muon systems. Two algorithms are used to give complementary efficiency across the momentum spectrum, the 'the outside-in' global muon algorithm and 'the inside-out' tracker muon algorithm [64].

The outside-in algorithm begins with muon tracks and for each attempts to identify a tracker match. Hits in muon chambers are used to define standalone-muon tracks. These are matched with tracker tracks by comparing parameters of the two tracks propagated onto a common surface. The hits from both systems are then combined and a global muon fit is performed using a Kalman filter. For muon tracks the momentum resolution is significantly improved by the global fit over a tracker-only fit for  $p_T < 200\text{GeV}$  [27, 65].

The inside-out algorithm selects all tracks satisfying  $p_T > 0.5\text{GeV}$  and  $p > 2.5\text{GeV}$ . These are then extrapolated to the muon system, taking into account effects from the magnetic field, multiple Coulomb scattering in the detector material and the average expected energy loses. If at least one muon segment matches the extrapolated track, the track qualifies as a tracker muon. Tracker muon reconstruction is more efficient than global muon reconstruction for low momenta of  $\sim p < 5\text{GeV}$ . This is due to requiring a hit in only a single segment of the muon system. Global muon reconstruction is more efficient for higher energy muons which are likely to pass through several muon stations [64].

In order to ensure the muons are prompt (produced in by the hard process such as vector boson decay) rather than non-prompt (produced from the in-flight decays of hadrons, taus or heavy quarks) and to reject fakes caused by the punch through of hadronic particles, additional selections are made. These include quality selection on the  $\chi^2$  of the muon track, a minimum number of valid hits as well as requirements on the impact parameters  $d_{xy} < 0.05\text{ cm}$  and  $d_z < 0.1\text{ cm}$  aimed at ensuring prompt muons.

Muons must be reconstructed through either the global or tracker muon algorithm. In combination, and including additional selections, these provide an efficiency of  $> 95\%$  for reconstructing a muon with  $p_T$  larger than a few GeV over the full  $\eta$  range covered by the muon system and a fake rate from hadrons of  $< 1\%$  [64].

### 4.2.3 Particle Flow

The particle flow (PF) algorithm combines the inputs from dedicated track reconstruction and calorimeter clustering algorithms using all detector subsystems to identify and reconstruct all stable particles in the event. Despite hundreds of different particle species

being produced by collisions at the LHC, only a small fraction have sufficient lifetimes and interactions with the detector to be directly measured. The predominant species measured by the CMS detector are:  $\gamma$ ,  $e^\pm$ ,  $\mu^\pm$ ,  $\pi^\pm$ ,  $K^\pm$ ,  $p^\pm$ ,  $K^0$  and  $n$ , classified by the PF algorithm into five categories of photons, electrons, muons, charged hadrons and neutral hadrons. The identification and measurement of the properties of these particles is optimised by taking advantage of the complementarity of different subsystems in various kinematic regimes and geometries. The output list of the individual particles is similar to that provided when generating simulated events and can be used as an input for further reconstruction processes such as building jets, determining  $\cancel{E}_T$ , determining jets originating from bottom quarks (b tag) and quantifying charged lepton isolation. The algorithm is described fully in [66, 67].

Effective track reconstruction forms the core of the PF algorithm. The CMS detector, with a strong magnetic field and large silicon tracker, is highly capable of the efficient track reconstruction required. In addition, the high granularity ECAL allows effective separation of photons from charged particles, even inside jets of several hundred GeV, and the entire calorimetry system is included within the solenoid, allowing the uninterrupted measurement of the particle energy flow.

The PF algorithm utilises a specific clustering algorithm for calorimeter deposits which is performed separately in each calorimeter subdetector. First, cluster seeds are identified as local cell maxima over a threshold energy. Second, these are grown into topological clusters by aggregating any cells with at least one side in common with a cell already in the cluster and with an energy above a given, detector subsystem dependent, threshold. Finally, the total energy in each topological cluster is shared between all encompassed seed clusters according to the cell-cluster distance to form a PF cluster for each seed. Along with reconstructed tracks, these PF clusters form the inputs required to build PF candidates.

The PF reconstruction uses a link algorithm to iteratively check compatibility of charged particle tracks and/or calorimetry clusters and/or muon tracks. These elements must be connected while avoiding any double counting. The link algorithm is performed on every pair of elements in the event and defines a distance between them that quantifies the quality of the link. This is used to produce blocks of elements linked directly or indirectly. The blocks are constructed depending on the subsystems being linked as described below:

- A link between a charged particle track and calorimeter deposit is made by extrapolating the last measured hit in the tracker through the calorimetry systems. The track is linked to a cluster if the calorimeter position is within the cluster boundaries. The link distance is defined as the distance in the  $(\eta, \phi)$  plane between the extrapolated track position and cluster position.
- Clusters caused by photons emitted by electrons (bremsstrahlung) are associated to the track by extrapolating the tangents to the track from the intersection points of the track with tracker layers to the ECAL. The distance measure is as defined above.
- Calorimeter clusters are linked between HCAL and ECAL or between ECAL and PS clusters by establishing whether the cluster in the more granular calorimeter is within the cluster of the less granular. The link distance is defined as the distance in the  $(\eta, \phi)$  plane between the cluster positions.
- Charged particles tracks are associated with muon tracks following the global muon algorithm defined in Section 4.2.2. In this case the  $\chi^2$  of the global fit defines the link distance.

With the blocks defined, the algorithm for reconstruction and identification of the set of particles from each block, which forms a global description of the event, proceeds as follows:

- First, each global muon is defined as a PF muon if its combined momentum is compatible with the momentum from only the tracker, within three standard deviations. The track is removed from the block and expected energy depositions along the path of the muon in the calorimeters are subtracted (measured with cosmic ray muons to be 3 GeV and 0.5 GeV respectively for the ECAL and HCAL).
- Electrons are then identified. Tracks are preidentified as electron tracks based on their characteristics within the tracker. Such tracks are refitted with a GSF and extrapolated to the ECAL. Several tracking and calorimetric variables are then used to perform a final identification of PF electrons. The track and ECAL clusters (including those from bremsstrahlung) are removed from the block.
- The remaining tracks undergo additional quality criteria and are connected to ECAL and HCAL clusters. If calorimetric deposits are linked with a track, a PF charged hadron is identified.
- The detection of neutral particles in addition to the PF charged hadron relies on a comparison of the momentum of the tracks and the calibrated energy in the calorimeters. The momentum and energy are calculated from the track momentum

under a charged pion hypothesis. If the calibrated calorimetric energy is significantly in excess of this energy, considering the calorimetric resolution, a PF photon and possibly a neutral hadron are also identified. If the energy excess is larger than the total ECAL energy, a PF photon is created with the ECAL energy and a PF neutral hadron is created taking its energy as the remainder of the excess. Otherwise, only a PF photon is created with the energy of the excess.

- Any remaining ECAL and HCAL clusters give rise to PF photons and PF neutral hadrons respectively.

#### 4.2.4 Pileup estimation

In reconstructing the hard process, it is important to remove contributions from additional vertices. The PF objects can be used to identify charged hadrons which do not originate from the primary vertex. However, the vertex for neutral particles cannot be determined. Instead, the ratio of neutral and charged particles can be measured in simulation and a correction factor determined. This is necessary as neutral particles compose  $\sim 50\%$  of the pileup in the barrel. An additional form of pileup subtraction relies on an estimate of the local energy density of pileup,  $\rho$ , which can then be used to correct physics objects covering an area,  $A$ , as

$$p_T^{\text{corr}} = p_T^{\text{raw}} - \rho \cdot A, \quad (4.2)$$

where the values for  $\rho$  are determined by partitioning the detector into a square grid of spacing 0.55 and calculating the median energy of the energy density of all PF candidates within each cell (grid  $\rho$ ) [68, 69]. This effective area (EA) correction mitigates the contributions of both charged and neutral pileup particles.

#### 4.2.5 Isolation

The level of hadronic activity around a lepton provides an effective method for distinguishing between prompt and non-prompt leptons. This is measured by the isolation of the lepton, defined by the fraction of energy in a cone around the lepton relative to the energy carried by the lepton itself. For the CMS collaboration, the standard method of

measuring isolation during Run 2 is PF isolation,  $I_{PF}^{rel}$ , defined within a cone of radius  $\Delta R$  as

$$I_{PF}^{rel} = \frac{1}{p_T^l} \left[ \sum_{PF_{PV}} p_T^{CH} + \sum_{PF} p_T^{NH} + \sum_{PF} p_T^\gamma - \sum_{PU} p_T^{\text{Neutral}} \right] \quad (4.3)$$

where  $p_T^l$ ,  $p_T^{CH}$ ,  $p_T^{NH}$ ,  $p_T^\gamma$  are the momenta of the lepton, charged hadrons, neutral hadrons and photon respectively. A subtraction of the neutral pileup must be made as neutral particles cannot be associated with the PV. The  $\Delta\beta$  correction and effective area (EA) correction are two methods used by CMS to estimate and correct for the neutral pileup contribution. The  $\Delta\beta$  correction estimates the energy from the neutral hadrons from the charged hadron component, based on simulation, as

$$\sum_{PU} p_T^{\text{Neutral}} = \frac{1}{2} \sum_{PF_{PU}} p_T^{CH} \quad (4.4)$$

while the EA method corrects the expected neutral pileup energy based on the footprint of the particle,  $A_{eff}$  and the grid pileup energy density computed from neutral particles,  $\rho_{grid}^{\text{Neutral}}$

$$\sum_{PU} p_T^{\text{Neutral}} = \rho_{grid}^{\text{Neutral}} \cdot A_{eff}. \quad (4.5)$$

the cone size may be fixed (relative isolation) or dependent on the  $p_T$  of the particle (mini-isolation). The use of mini-isolation accounts for the increasing collinearity of the hadronic decays of boosted particles.

#### 4.2.6 Isolated tracks

Unreconstructed prompt leptons form a large background for hadronic searches. Such lost leptons can be caused by both acceptance effects and misreconstruction of processes, including  $e^-$ ,  $\mu^-$  decays and hadronic decays of  $\tau$  leptons. Typically, even if not associated

to the lepton, the lepton track will still be reconstructed. Prompt leptons also tend to be isolated and, therefore, a veto of high energy isolated charged tracks can reject events containing misreconstructed leptons. Isolated tracks are defined from PF candidates associated with the PV and which pass track quality selection but are not identified as leptons.

## 4.3 Jet reconstruction

As the LHC is a hadron collider, most events will involve the production of quarks and gluons. As discussed in Chapter 2, these strongly interacting particles hadronise into collimated jets of particles. As described in the following section, the properties of the parton which originated the jet can be reconstructed by combining all of the particles forming the jet. In order for the properties of the jet to be theoretically tractable the reconstruction algorithm has to satisfy the requirements of infrared safety, insensitive to the addition of soft particles, and collinear safety, insensitive to collinear splitting of particles [8].

### 4.3.1 Jet clustering

To achieve infrared collinear safety, CMS uses a sequential recombination algorithm [70]. The input clusters can represent the momenta of particles, calorimeter energy deposits or previously clustered 4-vectors. These algorithms define inter-jet distances,  $d_{ij}$ , between each pair of clusters i and j, as well as beam-jet distances,  $d_{iB}$ , between each cluster and the beam

$$d_{ij} = \min \left[ p_{T_i}^r, p_{T_j}^r \right] \left( \frac{\Delta R_{ij}}{R} \right)^2, \\ d_{iB} = p_{T_i}^r \quad (4.6)$$

where the  $r$  parameter depends on the specific algorithm used,  $R$  determines the maximum distance for clustering pairs and  $p_{T_i}$  is the transverse momentum of the cluster. The algorithm then proceeds as follows:

- Calculate and rank all the distances,  $d_{ij}$  and  $d_{iB}$  for all clusters in the event.

- If the smallest distance is an inter-jet distance, combine clusters  $i$  and  $j$  into a new cluster and recalculate distances.
- If the smallest distance is a beam-jet cluster,  $i$  is considered to be a final state jet and is removed from the event. Distances are then recalculated.

These steps are repeated until no clusters remain. The algorithm used for the analysis in this thesis (and for most CMS analyses) is the anti- $k_T$  algorithm, for which  $r = 2$ . The size of the jets is  $R = 0.4$  which is optimal for capturing particles associated with a jet while being resilient against pileup. CMS uses jets with inputs from PF candidates (PF jets) and calorimeter deposits (calo jets) clustered using the FASTJET package [68]. PF jets allow improved resolution with respect to calo jets due to the significant position and energy resolution enhancement possible with use of the tracker. PF jets are therefore used in offline analysis while calo jets are used only in HLT reconstruction where latency restrictions forbid the formation of the PF candidates.

To reject jets that are badly reconstructed or originate from detector noise, additional selections are made. These include at least two PF candidates, the fraction of energy from neutral hadrons and photons  $< 99\%$ , charged hadron fraction  $> 0$  and charged particle multiplicity  $> 0$ . The rate of fake jets is reduced by 84% while maintaining  $> 99\%$  efficiency for jets from quarks and gluons.

### 4.3.2 Jet energy corrections

The energy of the clustered jets will not conform to the true partonic energy but instead is approximately distributed as a Gaussian around this value. This is due to variation in response in different sections of the detector, losses in uninstrumented sections of the detector, as well as random fluctuations in the particle composition during hadronisation. To recover the properties of the parton, jet energy corrections (JECs) are applied using the functional form [71]

$$p_\mu^{\text{corr}} = C_{\text{offset}}(p_T^{\text{raw}}) \cdot C_{\text{rel}}(\eta) \cdot C_{\text{abs}}(p'_T) \cdot C_{\text{res}}(p_T'', \eta) \cdot p_\mu^{\text{raw}}. \quad (4.7)$$

where  $C_{\text{offset}}$ ,  $C_{\text{rel}}$ ,  $C_{\text{abs}}$  and  $C_{\text{res}}$  represent offset, relative, absolute and residual corrections respectively,  $(p_\mu^{\text{raw}})$   $p_\mu^{\text{corr}}$  is the (uncorrected) corrected jet 4-momentum,  $p'_T$

is the  $p_T$  after the offset and relative corrections and  $p'_T$  is the  $p''_T$  after all corrections except the residual. The corrections are described in more detail below [72]:

- The  $C_{\text{offset}}$  is the first step in the chain. Its purpose is to remove energy contributions not associated with the hard scattering that instead originate from sources such as noise and pileup. The pileup contributions are removed using charged hadron subtraction (CHS), where PF candidates not associated with the PV are removed before clustering, and the jet area method. The jet area method removes neutral components of pileup from the jets by subtracting  $\rho \cdot A_j$  from the  $p_T^{\text{raw}}$ , where  $A_j$  is the active area of the jet and  $\rho$  is the average pileup energy density, determined from the median energy of PF candidates across the detector.
- The  $C_{\text{rel}}$  is used to make the energy response uniform in  $\eta$  for all jets using MC truth corrections derived from QCD dijet events.
- The  $C_{\text{abs}}$  is used to correct the energy response as a function of jet  $p_T$ . This is done using  $Z + \text{jets}$  and  $\gamma + \text{jets}$  events as the boson  $p_T$  is well known and can therefore be used to balance the  $p_T$  of the reconstructed jet.
- The  $C_{\text{res}}$  is used to correct residual differences between the responses in both  $p_T$  and  $\eta$  for data and MC and is applied in data only.

Each correction has associated systematic and statistical uncertainties. These are added in quadrature to define the overall jet energy uncertainty. The overall uncertainty is shown in Fig 4.2.

### 4.3.3 B tagging

For Run 2, the combined secondary vertex version 2 (CSVv2) algorithm is used to tag jets as originating from b quarks. The algorithm exploits the long lifetime of the b hadron, the secondary vertex of its decay and the possible presence of a muon or electron (produced in  $\sim 20\%$  of the b hadron decays). The input variables are combined with a neural net and the secondary vertex information is obtained using the Inclusive Vertex Finder (IVF) algorithm [74].

The dominant backgrounds for tagging b quarks are jets originating from c quarks and to a lesser extent jets from lighter quarks and gluons. The distribution of the CSVv2 discriminator is shown for PF jets in Figure 4.3 using 13 TeV data and simulation. The value of the discriminator used in the  $\alpha_T$  analysis is 0.89, corresponding to an efficiency of  $\sim 67\%$  and a mistag rate of  $\sim 1\%$  for light quarks ( $u, d$  and  $s$  quarks) and gluons and

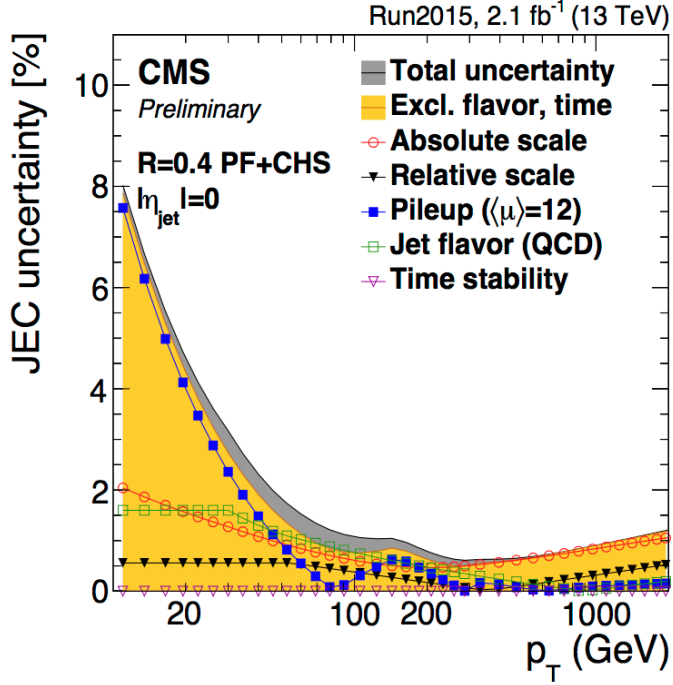


**Figure 4.2:** The overall uncertainty in the corrections applied to MC from Equation 4.7 is shown in the orange solid curve. The pileup uncertainty dominates for  $p_T < 50\text{GeV}$  while for higher values of  $p_T$  the absolute and relative scale dominate [73].

of  $\sim 10\%$  for charm quarks. The difference in efficiency and mistag rates in data and simulation is measured for a range of jet energies to provide scale factors to correct the simulation. In the Run 2 dataset, these scale factors were around 0.94 and 1.1 to 1.3 (depending on  $p_T$ ) for the b tag and mistag SFs respectively [75].

#### 4.3.4 Energy sums

Energy sums are vital for hadronic searches for new physics such as the  $\alpha_T$  search. The typical high mass scale of BSM models causes large quantities of energy to be transferred to particles in the final state. This energy is shared between both visible and invisible particles, leading to significant total and missing energy which can be measured by CMS. The CMS detector is ideally suited to measuring these signatures due to its hermetic design allowing optimal acceptance for all observable particles in the final state.

To measure the energy scale of the parent process in the event two variables are commonly used. These are the total transverse energy,  $E_T$ , which is computed as the scalar sum of the transverse energies of all reconstructed PF candidates in the event and

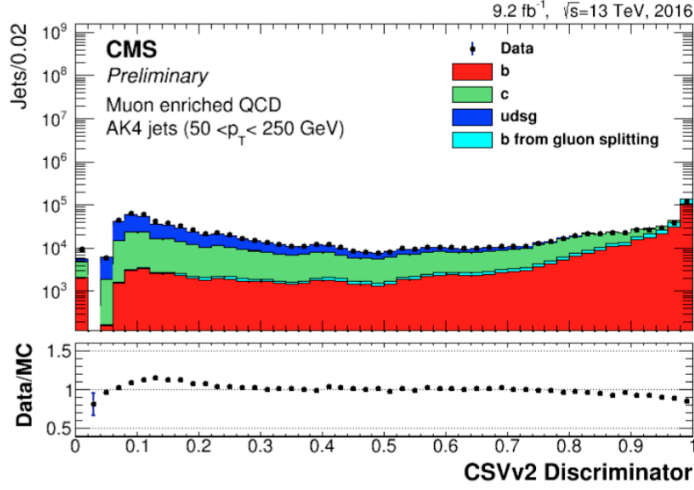


**Figure 4.3:** Distribution of the CSVv2 discriminator for jets defined using the anti- $k_t$  algorithm in a muon enriched jet sample. The markers correspond to the data. The stacked, coloured histograms indicate the contributions of the different jet flavours in the simulation [75]

the total hadronic transverse energy,  $H_T$ , which is computed as the scalar sum of the transverse energies of all calibrated reconstructed jets:

$$E_T = \sum |\vec{p}_T^{\text{PF}}| \quad H_T = \sum |\vec{p}_T^j|. \quad (4.8)$$

The momentum of particles which do not interact with the CMS detector is reconstructed indirectly using the observed particles in the final state by exploiting momentum conservation in the transverse plane. Two variables are used in the  $\alpha_T$  analysis: the missing transverse momentum,  $\vec{E}_T^{\text{PF}}$ , which is defined as the negative vector sum of the transverse momenta of all PF candidates and has magnitude  $E_T$ , as well as the hadronic missing transverse momentum,  $\vec{H}_T$ , which is defined as the negative vector sum of the transverse momenta of all calibrated reconstructed jets and has magnitude  $H_T$ :

$$\vec{E}_T^{\text{PF}} = -\sum \vec{p}_T^{\text{PF}} \quad \vec{H}_T = -\sum \vec{p}_T^j. \quad (4.9)$$

In addition,  $\vec{E}_T^{\text{calo}}$ , defined as the negative transverse vector sum of the calorimeter deposits, is used for the HLT as the PF candidates cannot be reconstructed within latency constraints. The  $\vec{E}_T^{\text{PF}}$  is used offline as performance is substantially improved by including tracker information [67].

As a measure of the momentum imbalance,  $\vec{E}_T^{\text{PF}}$  can be biased by effects including minimum energy thresholds in the calorimeters, tracker inefficiencies and non-linearities in calorimeter response. This bias is reduced by correcting the  $p_T$  of CHS-corrected PF jets using the JECs and propagating the correction to the  $\vec{E}_T^{\text{PF}}$  as

$$\text{corrected } \vec{E}_T^{\text{PF}} = \vec{E}_T^{\text{PF}} - \sum_j (\vec{p}_T^{\text{corr},j} - \vec{p}_T^j). \quad (4.10)$$

This ‘type-1’ correction [76] uses all corrected jets with  $p_T > 15 \text{ GeV}$  with less than 0.9 of their energy deposited in the ECAL. The 4-momenta of any muons found in jets are subtracted when performing the correction and added back to the corrected object. Figure 4.4 shows excellent agreement between simulation and data in reconstructing the  $\vec{E}_T$  with 13 TeV Run 2 data.

## 4.4 Physics objects for the $\alpha_T$ analysis

The  $\alpha_T$  analysis makes use of the reconstruction algorithms described above to identify and reconstruct physics objects. The analysis uses a hadronic signal region with jets and large  $\vec{E}_T$ , as well as several signal depleted regions used to predict the backgrounds in the signal region, the hadronic,  $\gamma + \text{jets}$ ,  $\mu + \text{jets}$  and  $\mu\mu + \text{jets}$  control regions defined in Section 6.4.2. This section describes the definition of the physics objects used for the  $\alpha_T$  analysis.

### 4.4.1 Jets

The jets are reconstructed using PF objects, as described in Section 4.3, and are corrected for pileup contributions using CHS and jet area corrections. Additional cleaning cuts are then applied on the jet constituents as summarised in Table 4.1. These requirements are necessary to reject fake jets and jets reconstructed from pileup. The charged hadron

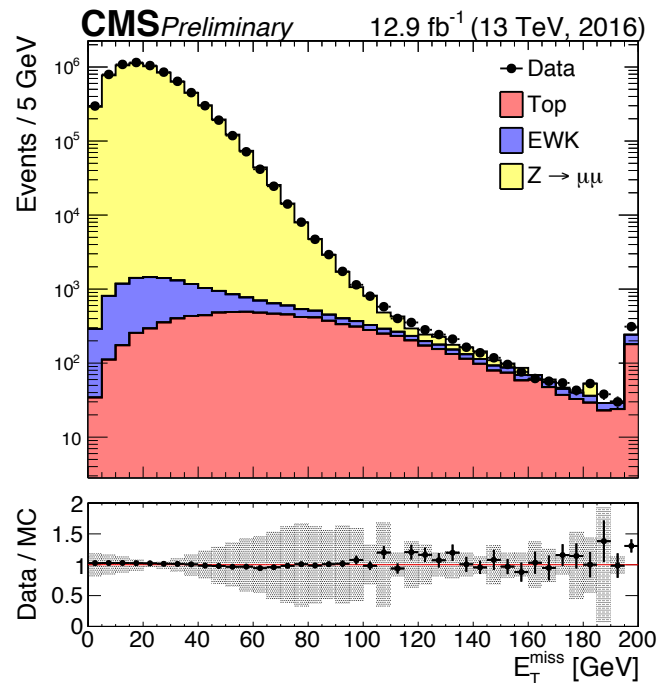


**Figure 4.4:** Distribution of  $E_T^{\text{miss}}$  in  $Z \rightarrow \mu\mu$  candidate events. The markers show the data while the filled coloured histograms show the breakdown in difference processes for the simulation. The lower panel shows the data/MC ratio including both statistical and systematic uncertainties [76].

fraction cut of  $> 0.1$  additionally rejects jets reconstructed from beam halo interactions (see Section 6.1.1).

A threshold of jet  $p_T > 40\text{ GeV}$  is required for jets used in the analysis which further rejects fake jets. Jets in the signal region must satisfy the pseudorapidity requirement  $|\eta| < 2.4$ . The presence of any forward jets with  $|\eta| > 2.4$  is used to improve the  $H_T$  resolution and reject the QCD multijet background (as described in Section 6.2.4). Additionally, the leading jet in the event must satisfy  $p_T > 100\text{ GeV}$ .

**Table 4.1:** Jet identification requirements.

Variable	Cut	Notes
$-3.0 < \eta_{\text{jet}} < 3.0$		
Neutral Hadron Fraction	$< 0.99$	-
Neutral EM Fraction	$< 0.99$	-
Number of constituents	$> 1$	-
Charged Hadron Fraction	$> 0$	only for $ \eta_{\text{jet}}  < 2.4$
Charged Hadron Fraction	$> 0.1$	for highest $p_T$ jet (otherwise veto event)
Charged Multiplicity	$> 0$	only for $ \eta_{\text{jet}}  < 2.4$
Charged EM Fraction	$< 0.99$	only for $ \eta_{\text{jet}}  < 2.4$
$ \eta_{\text{jet}}  > 3.0$		
Neutral EM Fraction	$< 0.90$	-
Number of Neutral Particles	$> 10$	-

## B tagged jets

Jets originating from b quarks are identified using the CSVv2 algorithm defined in Section 4.3.3.

### 4.4.2 Photons

Photons must be identified to define the  $\gamma + \text{jets}$  control region and veto events in the signal and muon control regions. Their reconstruction is described in Sections 4.2.1 and 4.2.3. The photon isolation is ensured using PF relative isolation with a cone size of  $\Delta R = 0.3$ .

Pileup contributions are mitigated using EA correction. Additional selections are summarised in Table 4.2; an efficiency for photon identification of  $\sim 71\%$  is achieved. The number of fake and non-prompt photons passing selection is measured as 2 – 10% depending on  $H_T$ .

The kinematic selection for photons used to veto events in the signal region is  $p_T > 25 \text{ GeV}$  and  $|\eta| < 2.5$ . The photons used to define the control region must satisfy the tighter requirements  $p_T > 25 \text{ GeV}$  and  $|\eta| < 1.4$  to ensure efficient trigger selection and to be sure that the photon is contained within the barrel where it can be better reconstructed.

**Table 4.2:** Photon identification requirements.

Categories		Barrel	
Working point	Tight		
		Loose	
Conversion safe electron veto	Yes		Yes
Single Tower H/E	0.05		0.05
$\sigma_{i\eta i\eta}$	0.0100		0.0102
PF charged hadron isolation	0.76		3.32
PF neutral hadron isolation	$0.97 + 0.014 \times p_{T,\gamma} + 0.000019 \times p_{T,\gamma}^2$	$1.92 + 0.014 \times p_{T,\gamma} + 0.000019 \times p_{T,\gamma}^2$	
PF photon isolation	$0.08 + 0.0053 \times p_{T,\gamma}$	$0.81 + 0.0053 \times p_{T,\gamma}$	

Categories		Endcap	
Working point	Tight		
		Loose	
Conversion safe electron veto	Yes		Yes
Single Tower H/E	0.05		0.05
$\sigma_{i\eta i\eta}$	0.0268		0.0274
PF charged hadron isolation	0.56		1.97
PF neutral hadron isolation	$2.09 + 0.014 \times p_{T,\gamma} + 0.000025 \times p_{T,\gamma}^2$	$11.86 + 0.014 \times p_{T,\gamma} + 0.000025 \times p_{T,\gamma}^2$	
PF photon isolation	$0.16 + 0.0034 \times p_{T,\gamma}$	$0.83 + 0.0034 \times p_{T,\gamma}$	

#### 4.4.3 Electrons

Electrons are identified to veto events in the signal and control regions. The full reconstruction is described in Sections 4.2.1 and 4.2.3. The isolation uses PF mini-isolation with a variable cone size of maximum radius  $\Delta R = 0.2$ . The requirements are summarised in Table 4.3. An overall efficiency for electron selection of  $\sim 90\%$  is achieved.

The kinematic requirements for electrons used to vetoing are  $p_T > 10 \text{ GeV}$  and  $|\eta| < 2.5$ .

**Table 4.3:** Electron identification requirements.

Categories	Barrel	EndCap
$\Delta\eta_{In}$	0.0105	0.00814
$\Delta\phi_{In}$	0.115	0.182
$\sigma_{i\eta i\eta}$	0.0103	0.0301
H/E	0.104	0.0897
d0 (vtx)	0.0261	0.118
dZ (vtx)	0.041	0.822
$ (1/E_{\text{ECAL}} - 1/p_{\text{trk}}) $	0.102	0.126
Missing hits (inner tracker)	2	1
Conversion veto	yes	yes

#### 4.4.4 Muons

Muons are selected to define the single mu,  $\mu + \text{jets}$ , and double mu,  $\mu\mu + \text{jets}$  control regions as well as to veto events in the signal regions. The reconstruction is described in Section 4.2.2. The isolation is defined using a PF relative isolation requirement of  $I_{\text{PF}}^{\text{rel}} < 0.15$  with a cone size of  $\Delta R = 0.4$  for muons in the control regions and by using a PF mini-isolation requirement of  $I_{\text{PF}}^{\text{mini}} < 0.2$  with a maximum cone size of  $\Delta R = 0.4$  to veto events in the signal region. The muons are pileup-corrected using an EA correction. An efficiency for muon selection of  $\sim 98\%$  is achieved.

The kinematic requirements for muons used for veto are  $p_{\text{T}} > 10 \text{ GeV}$  and  $|\eta| < 2.4$ , while muons selected in the control regions must satisfy  $p_{\text{T}} > 30 \text{ GeV}$  and  $|\eta| < 2.1$ . This ensures efficiency for passing trigger requirements and that the muon is well reconstructed.

#### 4.4.5 Isolated tracks

Isolated tracks are used to identify single prong decays of the  $\tau$  lepton and misreconstructed leptons. They are selected from the charged PF candidates satisfying  $p_{\text{T}} > 10 \text{ GeV}$ ,  $\Delta z(\text{track}, \text{PV})$  and  $I_{\text{PF}}^{\text{rel}} < 0.1$  with a cone of  $\Delta R = 0.3$ .

#### 4.4.6 Energy sums

The  $\mathcal{E}_{\text{T}}$  is computed from the magnitude of the vector sum of the transverse momentum of all PF candidates in the event. This is type-1-corrected, as described in Section 4.3.4,

using PF jets with  $p_T > 15 \text{ GeV}$ . In the control regions the object(s) used to define the control region are not included in the  $\cancel{E}_T$  calculation. The  $\cancel{H}_T$  and  $H_T$  are defined using the vector and scalar sum, respectively, of all PF jets satisfying  $p_T > 40 \text{ GeV}$  and  $|\eta| < 2.4$ .

#### 4.4.7 Summary

A summary of the physics objects used for the  $\alpha_T$  search and their kinematic requirements is presented in Table 4.4.

**Table 4.4:** Kinematic selections for physics objects.

Object		Kinematic selection
Jet	Central jets	$p_T > 40 \text{ GeV},  \eta  < 2.4$
	Leading central jets	$p_T > 100 \text{ GeV},  \eta  < 2.4$
	Forward jet (veto)	$p_T > 40 \text{ GeV},  \eta  > 2.4$
Photon	$\gamma + \text{jets}$ control region (relative isolation)	$p_T > 200 \text{ GeV},  \eta  < 1.45$
	Veto (relative isolation)	$p_T > 25 \text{ GeV},  \eta  < 2.5$
Muon	$\mu + \text{jets}$ and $\mu\mu + \text{jets}$ control regions (mini isolation)	$p_T > 30 \text{ GeV},  \eta  < 2.1$
	Veto (relative isolation)	$p_T > 10 \text{ GeV},  \eta  < 2.5$
Electron	Veto (mini isolation)	$p_T > 10 \text{ GeV},  \eta  < 2.5$
Isolated track	Veto	$p_T > 10 \text{ GeV},  \eta  < 2.5$



# Chapter 5

## The Level-1 trigger upgrade

During Run 2, the LHC has provided collisions at an energy of 13 TeV and at a peak luminosity of  $14 \times 10^{33} \text{ cm}^{-2} \text{s}^{-1}$ , marking a significant increase in energy and luminosity over those provided in Run 1 (8 TeV and  $7 \times 10^{33} \text{ cm}^{-2} \text{s}^{-1}$  respectively). With a spacing between bunches of 25ns, an average of 25 simultaneous interactions are produced per bunch crossing. This high luminosity and pileup provides a challenging environment for the L1 trigger system, which must continue to provide an input rate to the HLT of 100 kHz, in conditions that exceed design specifications. Simply increasing thresholds on the L1 trigger seeds causes unacceptable inefficiencies for electroweak physics and TeV scale searches and, therefore, the L1 trigger system, and associated algorithms, must be upgraded.

In this section, the upgrades to the L1 calorimetric trigger system and the associated L1 jet algorithm are discussed. The muon trigger system and upgrades to the algorithms for identification of other physics objects for the L1 trigger are detailed in [77, 78, 79].

### 5.1 Legacy system and upgrade

The global calorimeter trigger (GCT) was used during Run 1 to find jets, electrons and photons and to compute global energy sums [80]. The trigger system takes input from trigger towers (TTs) corresponding to  $5 \times 5$  ECAL crystals and an identical area in the HCAL. These are grouped into  $4 \times 4$  ‘calorimeter regions’ that form the input for physics object and reconstruction algorithms for the GCT. Trigger primitive generators (TPGs) provide the interface with the detector to compute trigger inputs. Due to hardware limitations the detector is split into 16 sections, each processed by a regional calorimetric

trigger (RCT) to form candidates and sum energies. The RCTs must share information to account for features that occur at boundaries between the 16 sections. The information from the RCTs is combined in the GCT which computes global quantities and sorts the jets before passing these quantities to the global trigger (GT). The GT also receives information from the global muon trigger (GMT) and makes the final trigger decision.

The upgrade of the GCT was carried out in two stages. The first stage, upgrade calorimetric trigger (UCT), was used for data taking during 2015 and used updated firmware and algorithms to allow improved jet and object identification, including pileup subtraction [81]. In the second stage the architecture was entirely replaced by the time multiplexed trigger (TMT) to allow ‘time multiplexing’, whereby each event is processed entirely within one card using the full trigger tower granularity [82].

## 5.2 The time multiplexed trigger architecture

The TMT uses two processing layers. The first layer performs preprocessing and data formatting using 18 CTP7 cards [83]. Each card requires only a regional view of the detector and performs local operations such as summing ECAL and HCAL transverse energies. The data for each event is combined and transmitted to a single node in the second processing layer, an Imperial Master Processor Virtex-7 (MP7) card [83]. The MP7 is a high-performance  $0.92\text{Tb/s} + 0.92\text{Tb/s}$  (input + output rate) all-optical processor with sufficient data rate for the entire calorimeter to be processed in a single card. The data from the 9 nodes on the second layer is passed to a demultiplexer board (also an MP7) before being sent to the GT. The GT makes the final trigger decision using both the calorimeter and muon trigger systems.

The difference between the GCT/UCT and TMT architectures is shown schematically in Figure 5.1. In the TMT architecture, data is buffered and retransmitted to the first node (on the second layer) over 9 bunch crossings to allow the entire event to be processed on one card. This removes the need for a large number of links between cards and allows the full TT granularity to be used. The increase in granularity compared to the GCT is illustrated in Figure 5.2.

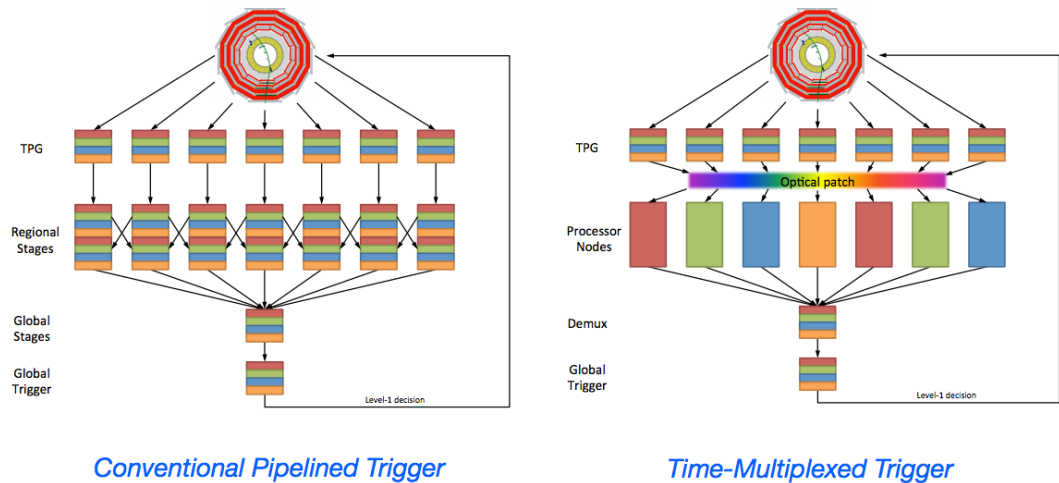


**Figure 5.1:** Comparison of the GCT (left) and TMT architectures (right) showing the flow of information to the final global decision. The colours indicate the data from each bunch crossing [82]

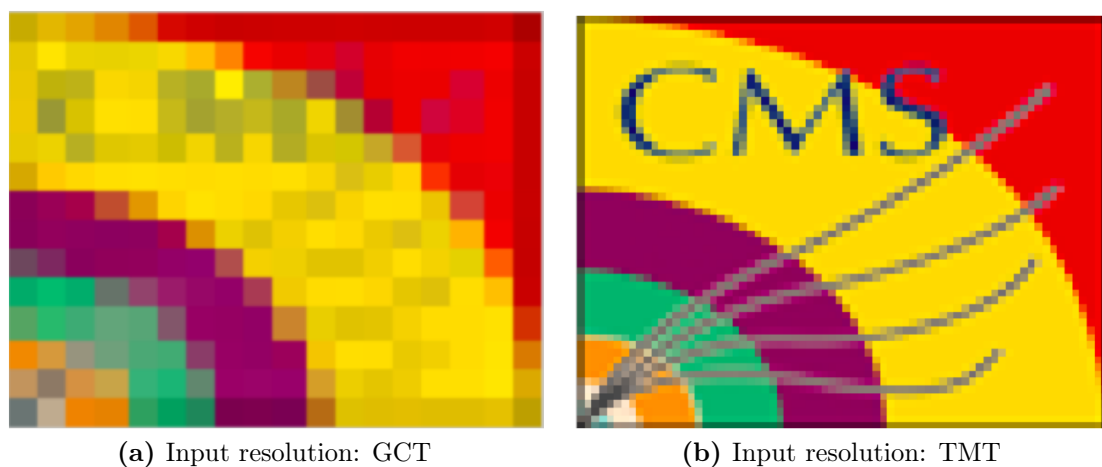


**Figure 5.2:** A representation of the CMS collaboration logo digitised with the input resolution of the L1 calorimeter trigger up to  $|\eta| < 3$  using (a) the legacy system ( $18 \times 14$  pixels) and (b) the TMT ( $72 \times 56$  pixels).

## 5.3 L1 jet algorithm

The increase in pileup and luminosity in Run 2 makes triggering with jets significantly more challenging than during Run 1. To maintain sensitivity to new physics the upgrade jet identification and reconstruction algorithm must provide high efficiencies and low rates for L1 trigger seeds. This performance must be maintained for high pileup scenarios.

The TMT architecture provides several advantages over the GCT system which can be exploited in designing the jet algorithm. These include significantly increased processing power and granularity (enhanced by factor 16). More flexible algorithms, which make use of smaller features than previously accessible, can be defined. This is exploited in the use of an improved jet clustering algorithm, described in Section 5.3, as well as online pileup subtraction, described in Section 5.4, for jet identification and reconstruction with the TMT.

### 5.3.1 GCT jet clustering

The GCT algorithm uses a  $3 \times 3$  calorimeter region sliding jet window with a central seed to reconstruction jets in the range  $|\eta| < 5$ . The algorithm scans the calorimeter in increments of calorimeter regions and clusters a jet if the energy in the central seed region is greater than both 5 GeV and each of the eight bordering regions. The threshold of 5 GeV was added during the 2012 8 TeV run, when the number of pileup interactions increased, to remove soft pileup jets. The  $12 \times 12$  TT jet size ( $\Delta\eta \times \Delta\phi = 1.04 \times 1.04$ ) corresponds approximately to  $R = 0.5$  for the anti- $k_T$  jet algorithm used in offline reconstruction.

### 5.3.2 TMT jet clustering

The jet algorithm used for the TMT similarly uses a sliding window algorithm. This is composed of  $9 \times 9$  TTs ( $\Delta\eta \times \Delta\phi = 0.78 \times 0.78$ ), corresponding to the  $R = 0.4$  used in Run 2. The use of an odd number of trigger towers ensures that a central seed tower can be defined.

In order to ensure that jets do not overlap, which would cause energy deposits to be double counted, the seed tower is required to meet the conditions shown in Figure 5.3. The veto conditions are asymmetric along the diagonal to prevent TTs with the same

>	>	>	>	>	>	>	>	>
$\geq$	>	>	>	>	>	>	>	>
$\geq$	$\geq$	>	>	>	>	>	>	>
$\geq$	$\geq$	$\geq$	>	>	>	>	>	>
$\geq$	$\geq$	$\geq$	$\geq$		>	>	>	>
$\geq$	$\geq$	$\geq$	$\geq$	$\geq$	$\geq$	>	>	>
$\geq$	>	>						
$\geq$	>							
$\geq$								

**Figure 5.3:** The  $9 \times 9$  veto conditions used to define jets. The inequalities ensure jet energies are not double counted

energy vetoing one another. An inefficiency may be expected if a jet vetoes another which itself vetoes a third. However, this effect was found to introduce a negligible ( $\sim 0.1\%$ ) inefficiency. A threshold on the central seed tower may additionally be required to reconstruct a jet, as discussed in Section 5.4.3.

If a seed passes the veto requirements, a jet is defined with a position given by the seed tower and an energy given by the total energy of the towers making up the jet. The seed position is used as jets tend to be boosted objects with an energy deposited in a small central area. Note that the L1 jets are massless such that  $p_T = E_T$ .

### Comparison with offline jet reconstruction

An evaluation of the performance of the TMT jet algorithm can be made by comparing the results of jet finding with the offline reconstruction algorithm used by most CMS analyses during Run 2, anti- $k_T$  with a distance parameter of 0.4, described in Section 4.3.

The trigger tower deposits were generated using a simulated sample of top pair-production ( $t\bar{t} + \text{jets}$ ) due to the plentiful sample of jets produced in this process. In

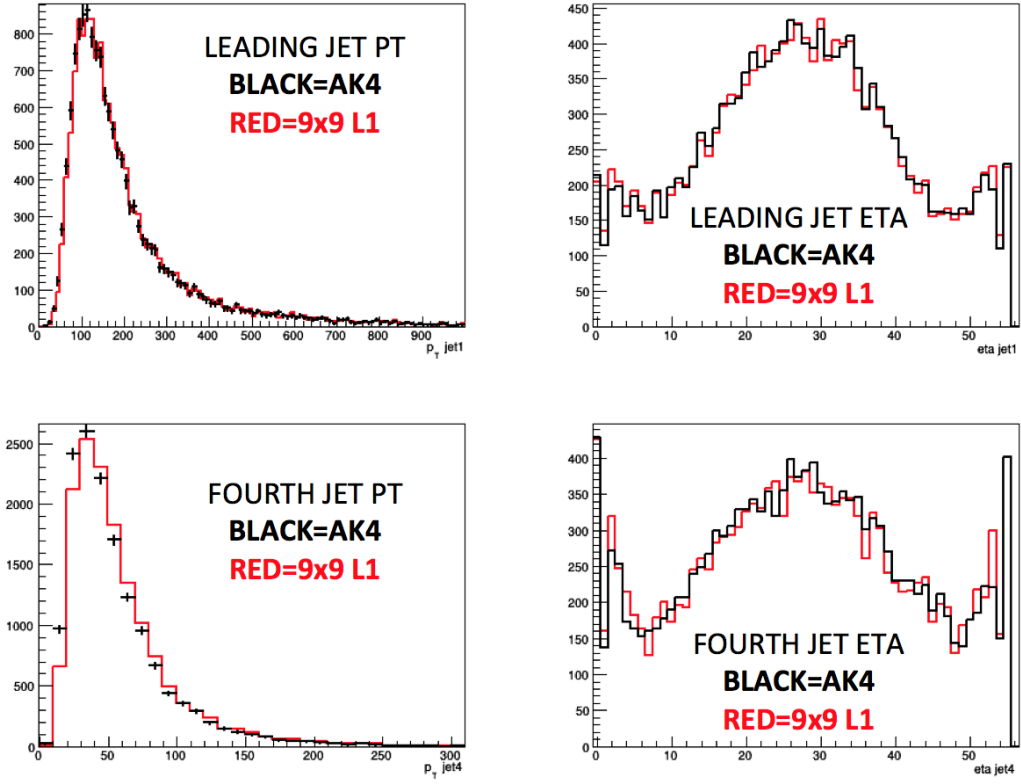


**Figure 5.4:** Comparison of the L1 jet finding algorithm with the anti- $k_T$  algorithm using TT inputs. Distributions of  $p_T$  and  $\eta$  are shown for the leading and fourth jet.

this section all simulated samples used have conditions of  $\sqrt{s} = 13$  TeV, bunch spacing = 50 ns and Gaussian distributed pileup around 40 simultaneous interactions. The anti- $k_T$  algorithm is run over the same inputs as used for the L1 algorithm with the FASTJET package [68].

A comparison between the predictions of both algorithms for several important jet variables is shown in Figure 5.4 for the leading and fourth jet. In general, excellent agreement is observed. Small differences can be seen at high  $|\eta|$  and low  $p_T$ . This is due to the ability of the anti- $k_T$  algorithm to reconstruct smaller jets with smaller radii while the L1 jet algorithm size is fixed.

### 5.3.3 Energy sums

In addition to jet reconstruction, the TMT must also build energy sums. These can be defined using either jets or individual calorimeter deposits, analogously to the offline quantities. The baseline quantities that are constructed are

- L1 total  $E_T$  : the scalar sum the  $E_T$  of all calorimeter TTs
- L1  $\cancel{E}_T$  : the inverse vector sum of the  $E_T$  of all calorimeter TTs
- L1  $H_T$  : the scalar sum of all L1 jet  $p_T$
- L1  $\cancel{H}_T$  : the inverse vector sum of all L1 jet  $p_T$ .

The quantities made using L1 jets require a minimum  $p_T$  of 20 GeV. As will be discussed in Section 5.5, this requirement provides additional robustness against soft jets reconstructed from detector noise or pileup. Additional quantities based on jets and/or energy sums may also be used to define trigger seeds. A study of the performance of one such variable is detailed in Section 5.6.

## 5.4 Pileup subtraction

Simultaneous soft interactions cause additional energy to be deposited throughout the detector. This will be approximately isotropically distributed ( $\sim 1$  GeV per unit area); however, variations in detector response as well as the profile of pileup events can cause  $\eta$  and, to a lesser extent,  $\phi$  dependence. In addition, event-by-event fluctuations in the distribution and magnitude of the pileup deposits can greatly affect calorimeter objects. For jets, pileup can both increase the energy of jets associated with the hard scatter and cause ‘pileup jets’ to be clustered entirely from pileup energy deposits.

Pileup subtraction at L1 aims to remove pileup contributions such that the trigger decision is unbiased by the presence of simultaneous interactions. Changes to detector response and beam conditions during running as well as the random nature of pileup necessitate an event-by-event estimation and mitigation of the pileup contribution. For the TMT, this must be done using only the calorimeter because tracker information is unavailable.

Several methods of pileup subtraction that meet the stringent latency requirement are discussed in this section. These rely on both global and local estimations of pileup in each event to perform pileup correction and reject pileup jets. Local methods are

more susceptible to statistical fluctuations; however, unlike global methods, they allow anisotropy in the pileup distribution to be considered.

### 5.4.1 Global $\rho$ subtraction

Global  $\rho$  subtraction uses the jets themselves to estimate the pileup energy density ( $\rho_{\text{pileup}}$ ) using the median energy density of all jets in the event, defined as  $\rho_{\text{global}}$  [69]. The main assumptions with this method are that the pileup distribution is independent of  $\eta$  and  $\phi$ , and that the number of pileup jets is much larger than the number from the hard scatter. Using  $\rho_{\text{global}}$ , a correction to each jet can be made:

$$p_{Tj}^{\text{subtracted}} = p_{Tj}^{\text{raw}} - \rho_{\text{global}} \cdot A_j, \quad (5.1)$$

where  $A_j$  is the area of the jet,  $\Delta\phi\Delta\eta(\eta)$  (the  $\eta$  dependence in the area is due to variation in the jet tower size). If  $\rho \cdot A_j > p_{Tj}^{\text{raw}}$  the jet is discarded. Figure 5.5 shows a strong linear dependence between  $\rho_{\text{global}}$  and the number of interactions for minimum bias events. The non-zero intercept is caused by contamination of jets from the hard scatter.

To account for  $\eta$  dependence in the pileup, the  $\rho_{\text{global}}$  subtraction may be amended by dividing the calorimeter into strips of phi and calculating the median  $\rho$  for jets in each strip. However, this significantly adds to the latency in the pileup subtraction and may be less robust as fewer jets can be sampled in each  $\eta$  slice and is therefore not considered in this section.

### 5.4.2 Doughnut subtraction

Doughnut subtraction makes use of the area around the jet to sample the local pileup energy density in order to correct (or reject) each jet and has been previously proposed for use during heavy ion collisions [85]. The energy contribution from the jet itself is negligible outside the  $9 \times 9$  ring, as shown in Figure 5.6. For doughnut subtraction the transverse energy density is sampled by taking four strips around the jet, as shown in Figure 5.7a. The strips are ordered according to energy density, and the median two strips taken. The pileup energy density is then estimated from the energy density of the

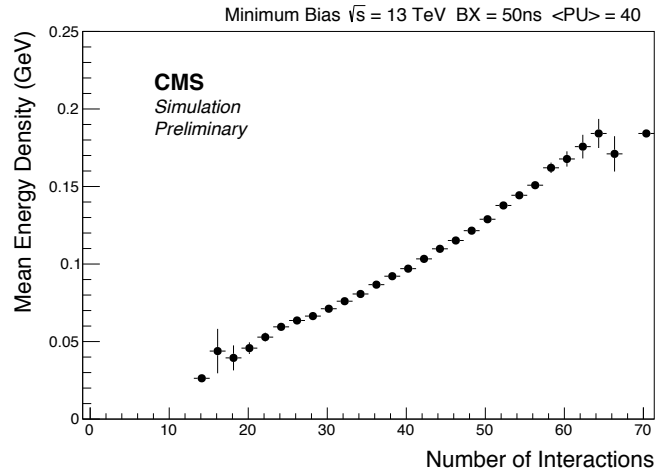


**Figure 5.5:** Dependence of  $\rho_{\text{global}}$  on the number of interactions

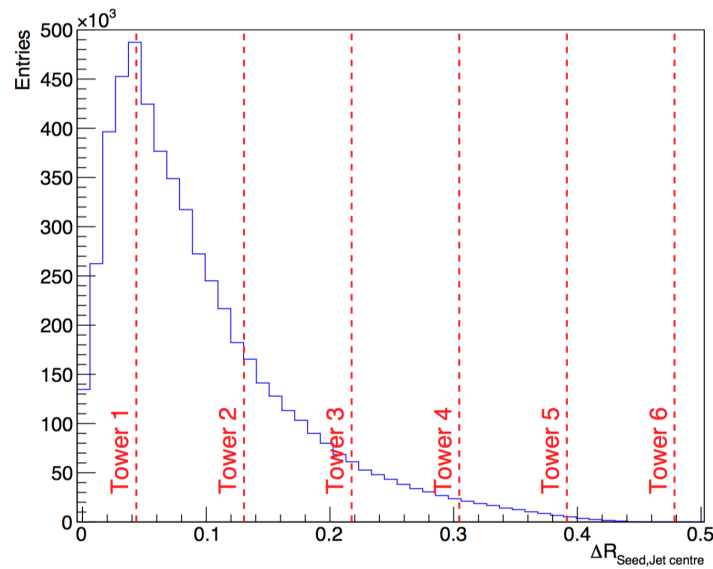


**Figure 5.6:**  $\Delta R$  distribution between the seed and constituent TTs using data from Run 1 [84].

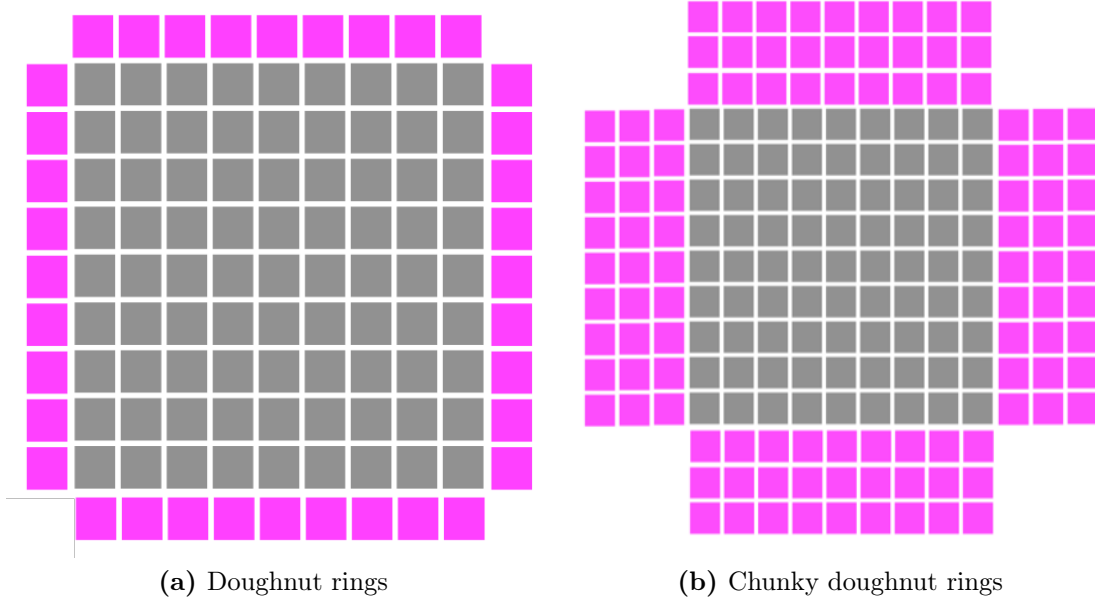


**Figure 5.7:** The rings used to sample the local pileup energy density for the doughnut (a) and chunky doughnut (b) pileup subtraction. The median two strips (in energy density) are used in each case.

median two strips. This  $\rho_{\text{doughnut}}$  is used to correct the jet analogously to Equation 5.1. Typically the strip with the largest energy density is susceptible to contribution from nearby jets. Using the median strips to estimate  $\rho_{\text{pileup}}$  allows such contamination to be mitigated.

Unlike global subtraction, doughnut subtraction allows local variations in  $\rho_{\text{pileup}}$  to be included; however, it is significantly more susceptible to statistical fluctuations because of the relatively small area sampled. An extension, ‘chunky’ doughnut, shown in Figure 5.7b, uses enlarged strips to sample three times the area in measuring  $\rho_{\text{pileup}}$ . The dependence of the number of interactions with the energy density for the chunky doughnut pileup estimation ( $\rho_{\text{chunky}}$ ) is shown in Figure 5.8.

### 5.4.3 Seed threshold and zero suppression

The requirement of a threshold on the seed tower when identifying a jet provides a powerful rejection of pileup jets. This takes advantage of the diffuser energy deposition for pileup jets compared to jets originating from the hard scatter. A seed threshold does not allow pileup contamination in real jets to be corrected but can be used in

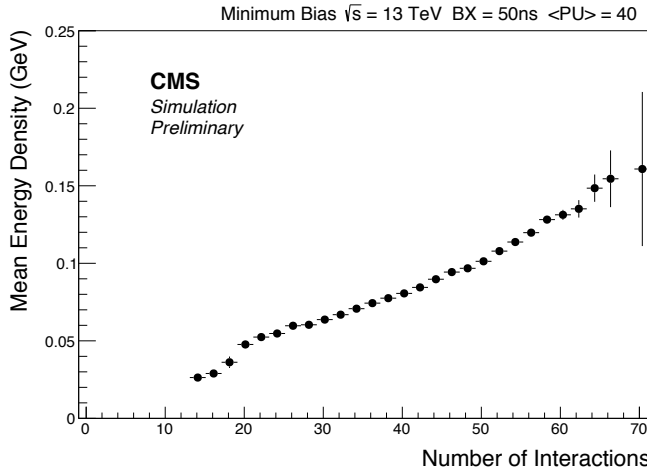


**Figure 5.8:** Dependence of  $\rho_{\text{chunky}}$  on the number of interactions

conjunction with other pileup subtraction techniques such as doughnut subtraction. Global  $\rho$  subtraction is incompatible with a seed threshold as this technique relies on reconstructing substantially more pileup jets than those from the hard scatter. This problem may be addressed by using a separate jet collection with no seed threshold for calculating  $\rho_{\text{global}}$ ; however, latency constraints do not permit this for the L1 trigger.

Zero suppression is a rudimentary form of pileup correction whereby only towers with an energy deposition above a given threshold are included in the reconstruction of each jet. This cannot be easily adapted for different pileup regimes but provides a simple baseline for assessing more complex algorithms. Zero suppression may also be used in conjunction with other pileup correction techniques.

The thresholds used for the seed and zero suppression may be  $\eta$  (or even  $\phi$ ) dependent; however, such variable thresholds are not considered in the studies presented below. The smallest energy quanta available at L1 is 0.5 GeV and defines a ‘L1 unit’. The thresholds considered in this section are 5 L1 units for the central seed (seed 5) and 1 or 2 L1 units for the zero suppression (labelled as TSup1 or TSup2).

#### 5.4.4 Calibration

The energy of the L1 jets ( $p_{\text{T}}^{\text{L1}}$ ) is calibrated against generator level quantities using a simulated QCD dijet sample. The calibration is carried out separately in the eight

$\Delta\eta = 0.75$  ranges from  $\eta = -3.0$  to 3.0 to account for changes in detector response. In each region the procedure is as follows:

- Cluster generator particles in the QCD sample (except muons and neutrinos) using the anti- $k_T$  algorithm with  $R = 0.4$  into generator jets.
- Match L1 jets to generator jets by finding the closest in  $\Delta R$  between the central tower of the L1 jet and the generator jet. L1 jets with  $\Delta R > 0.3$  from any generator jet are ignored.
- Define the ‘response’ for each L1 jet as the ratio of the (pileup-corrected)  $p_T^{L1}$  to the matched generator jet  $p_T$  ( $p_T^{\text{Gen}}$ ).
- For each bin in  $p_T^{\text{Gen}}$ , fit the response with a Gaussian to obtain the mean response for that  $p_T^{\text{Gen}}$ . The average  $p_T^{L1}$  in the bin is calculated to obtain the distribution of the mean response against  $p_T^{L1}$ .
- Perform a  $\chi^2$  fit of the distribution of mean response against  $p_T^{L1}$  using the calibration function [86] defined in Equation 5.2.
- Use the result of the fit to define correction factors for each  $p_T^{L1}$  in each  $\eta$  bin.

$$\left\langle p_T^{L1} / p_T^{\text{Gen}} \right\rangle^{-1} = p_T^{L1} \cdot \left( p_0 + \frac{p_1}{(\log p_T^{L1})^2 + p_2} + p_3 \exp(-p_4(\log p_T^{L1} - p_5)^2) \right) \quad (5.2)$$

The calibration must be done separately for each choice of pileup subtraction algorithm, seed threshold and zero suppression. Figure 5.9 shows an example response for seed 5, chunky-doughnut-corrected jets is shown as a function of  $p_T^{L1}$  for the  $0 < \eta < 0.75$  range. The fitted calibration function defines the correction factors and is shown to agree well with the data.

In Figure 5.10 the response for the same QCD dijet sample is shown as a function of the  $p_T^{L1}$ . The calibration is effective for  $p_T^{L1} > \sim 20 \text{ GeV}$  where the response is flat at unity. Below this  $p_T$ , the matching procedure degrades (the majority of matched jets come from pileup or detector noise) such that the average response is an unreliable estimate of the jet algorithm response to real jets.

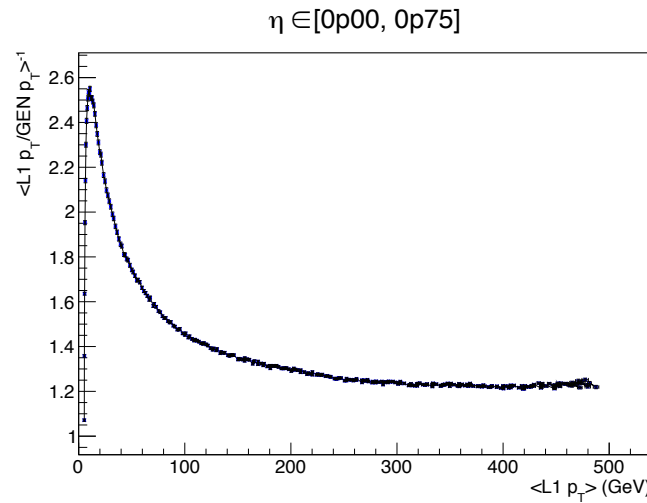


**Figure 5.9:** Fitted response for a QCD dijet sample in the range  $0 < \eta < 0.75$

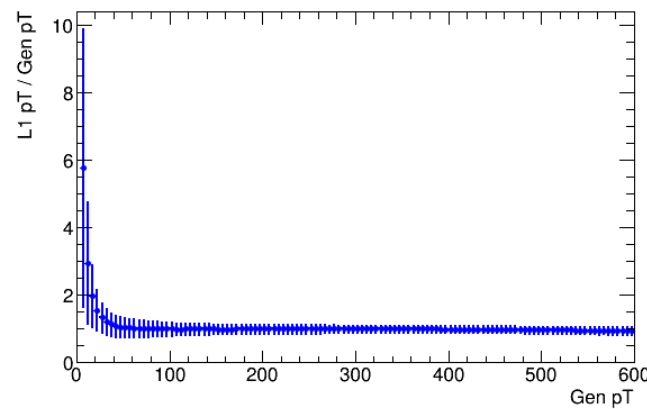


**Figure 5.10:** Calibrated response in the QCD dijet sample used to derive the calibration factors. The calibration is seen to be effective for the range  $p_T^{\text{L1}} > \sim 20 \text{ GeV}$ .

## 5.5 Jet performance

The performance of the jet algorithm and the various pileup suppression techniques is tested using Monte Carlo simulation. In each case, the corrected  $p_T^{L1}$  is calibrated following the procedure in Section 5.4.4. Comparisons are made with algorithms used for both the legacy GCT and UCT systems to benchmark the performance. Efficiencies are measured using a simulated  $t\bar{t}$  sample while background rates are measured using a simulated minimum bias sample.

### 5.5.1 Matching efficiency

The efficiency with which the L1 jets may be matched to generator jets provides a measure of the ability of the L1 jet algorithm to reconstruct real jets from the hard scatter. The matching procedure is the same as that used for the calibration. The matching efficiency for all generator jets and the fourth leading jet is shown in Figure 5.11 as a function of  $p_T^{\text{Gen}}$  for several benchmark pileup suppression algorithms. The efficiency plateaus at unity around  $p_T^{\text{Gen}} = 50 \text{ GeV}$ . The pileup subtraction and seed threshold is shown to reduce the matching efficiency at low  $p_T$ ; however, for this low  $p_T$  region the L1 jets matched to generator jets are typically reconstructed from pileup calorimeter deposits and their energy does not therefore reflect that of the matched generator jet. A substantial improvement in efficiency over the GCT is observed in matching the fourth leading jet.

### 5.5.2 Resolution

The resolution, defined as  $(p_T^{L1} - p_T^{\text{Gen}})/p_T^{\text{Gen}}$ , measures the level of agreement between the energies of the L1 and matched generator jets. The matching procedure is the same as that described in Section 5.4.4. The resolution provides an important measure of the ability of the algorithm to reject jets from pileup energy deposits as well as to remove the contribution of pileup from real jets from the hard scatter. In Figure 5.13a, the resolution as a function of the number of simultaneous interactions is shown for a simulated  $t\bar{t}$  sample. The resolution is flat near unity when pileup subtraction is applied, but exhibits a strong dependence on pileup if uncorrected. To illustrate the pileup contamination for different  $p_T^{\text{Gen}}$  jets, a linear fit to the resolution as a function of pileup is made in  $p_T^{\text{Gen}}$  bins; the resultant gradients are shown in Figure 5.13b. Pileup subtraction is shown

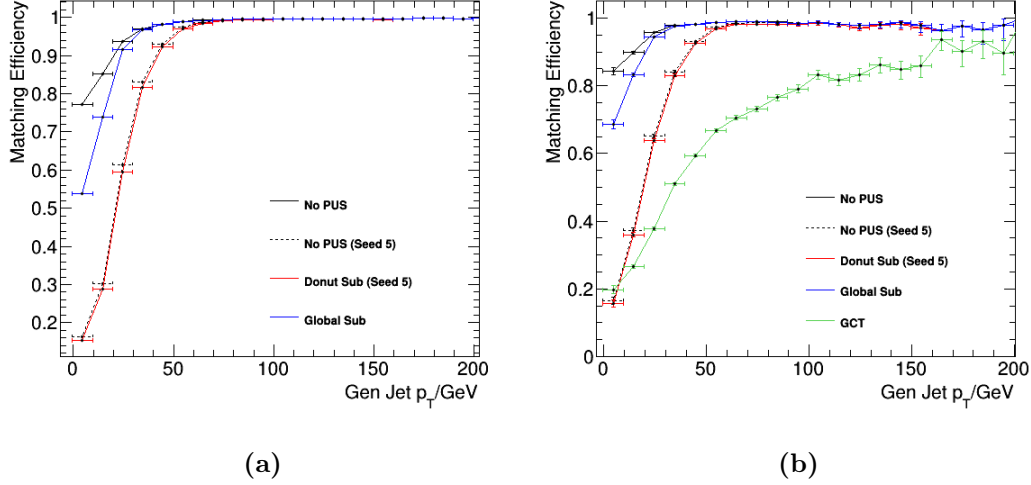


**Figure 5.11:** Matching efficiencies for jets showing effect of seed and pileup subtraction at low energies for all jets (a) and for the fourth jet (b). In (b) a comparison with the GCT is shown.

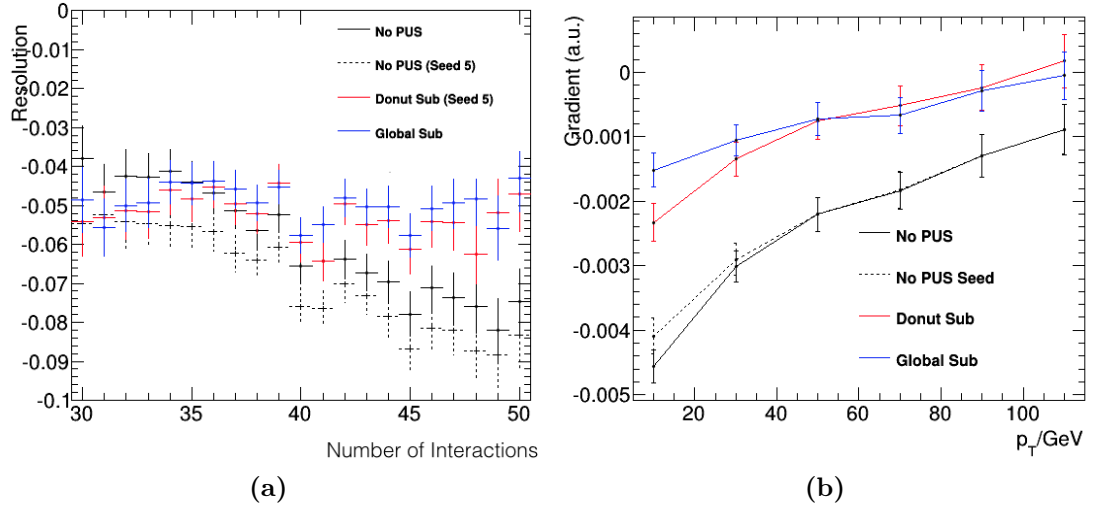


**Figure 5.12:** (a) Resolution as a function of the number of interactions. (b) Gradients of linear fits to resolution as a function of number of interactions in bins of  $p_T^{\text{gen}}$ .

to significantly reduce the pileup dependence of the resolution across  $p_T^{\text{Gen}}$ . If no pileup subtraction is applied, the magnitude of the gradient is particularly enhanced for low  $p_T^{\text{Gen}}$  where pileup contamination dominates.

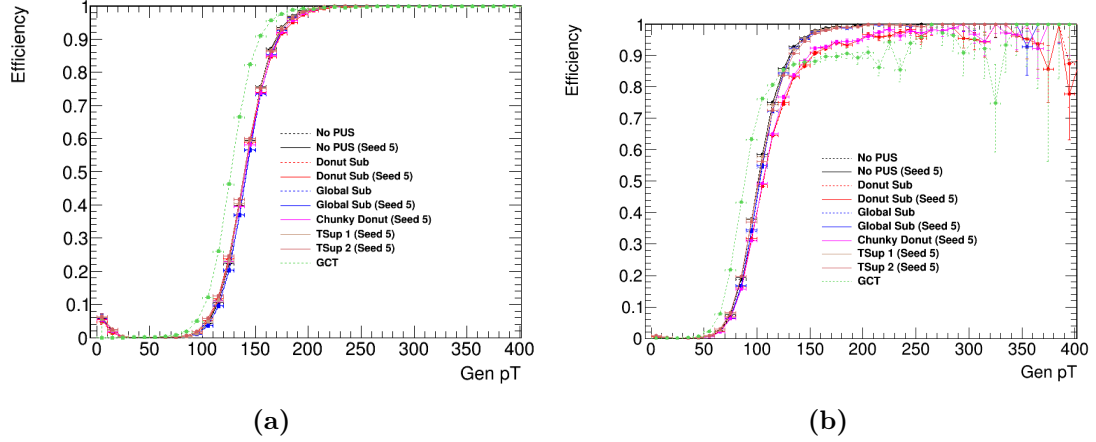


**Figure 5.13:** Efficiency as a function of  $p_T^{\text{Gen}}$  for (a) a L1 threshold of 150 GeV on the leading jet and (b) a L1 threshold of 100 GeV on the fourth leading jet.

### 5.5.3 Rates and efficiencies

The ‘turn-on’ of the efficiency for generator quantities for a L1 selection of 150 GeV on the leading jet and 100 GeV on the fourth leading jet are shown in Figure 5.13. The upgrade trigger exhibits a sharper turn-on than the GCT quantities and plateaus at higher values than the legacy system.

The efficiencies shown in Figure 5.13, however, do not fully describe the performance of the trigger as the total rate of selected events places stringent restrictions on the possible L1 thresholds. Figure 5.14 shows the rate of minimum bias events passing selection (per second) against the efficiencies for selecting a leading jet, second leading jet and fourth leading jet with  $p_T^{\text{Gen}}$  thresholds of 150 GeV, 110 GeV and 50 GeV respectively. As the jet multiplicity increases and threshold decreases, the performance of the upgrade L1 jets compared to the legacy system is substantially improved. For the upgrade L1 jets, the global  $\rho$  subtraction exhibits the best performance; however, the differences between the pileup subtraction algorithms are small.

During Run 2 the pileup is not constant but varies with changes in instantaneous luminosity. Stability in the rate for different pileup scenarios is import to ensure that L1 trigger thresholds do not need to be increased during running. Figure 5.15 shows the rate against the number of simultaneous interactions for a lead jet threshold of 30 GeV. The dependence on pileup is seen to be significantly mitigated by chunky doughnut pileup subtraction compared to no pileup subtraction and global  $\rho$  subtraction.

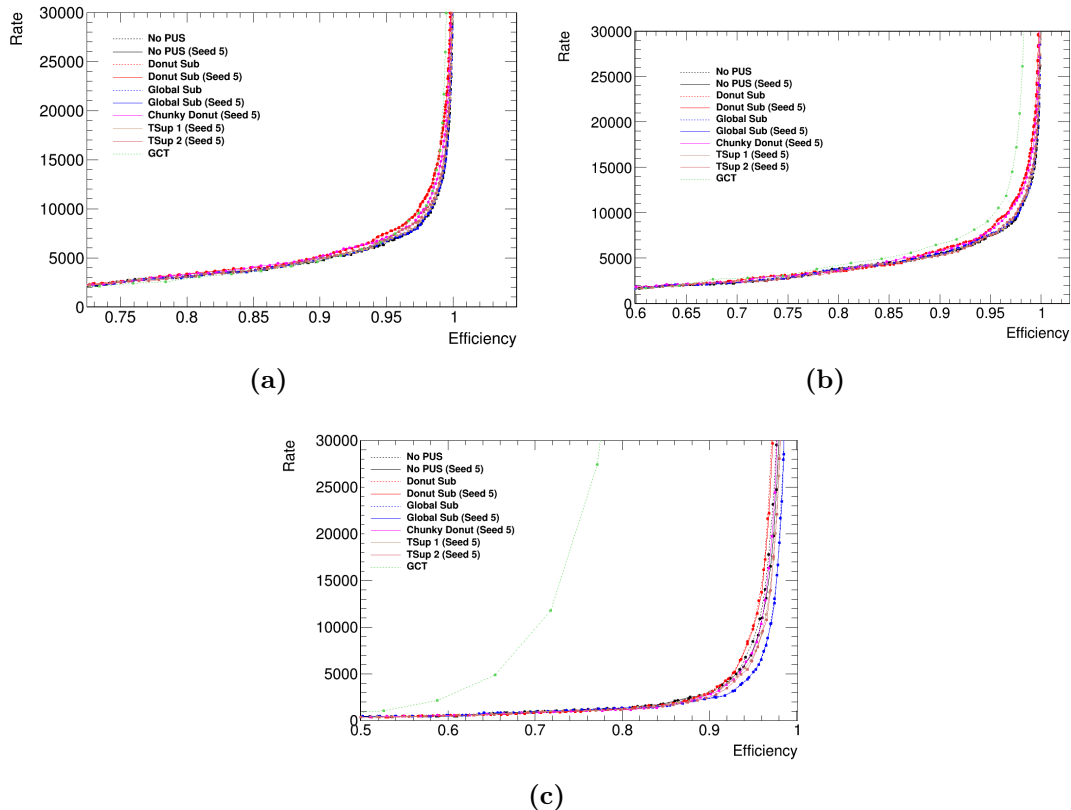


**Figure 5.14:** Rate (Hz) against efficiency for (a) L1 leading jet with a threshold of 150 GeV, (b) L1 second leading jet with a threshold of 110 GeV and (c) L1 fourth leading jet with a threshold of 50 GeV.

To benchmark the energy sums performance, the rate against efficiency for L1  $H_T$  and L1  $\cancel{H}_T$  is shown in Figure 5.16. All jets above 20 GeV are used to calculate L1  $H_T$ , making this quantity particularly susceptible to pileup. The chunky doughnut pileup subtraction with a seed of 5 is shown to significantly improve performance compared to the other pileup subtraction methods and the legacy system (except global  $\rho$  with a seed of 5, not viable in the L1 trigger). The performance of the UCT is not directly comparable as L1  $H_T$  and  $\cancel{H}_T$  are calculated using calorimeter regions above a threshold rather than jets. Similarly, the performance for L1  $\cancel{H}_T$  is optimal for chunky doughnut subtraction with a seed of 5 and global  $\rho$  subtraction. Figure 5.16b also shows L1  $\cancel{E}_T$ , which exhibits the best performance. This is expected as pileup contributions are deposited in  $\phi$  approximately uniformly throughout the detector and their contribution will therefore cancel in the vector sum of the towers.

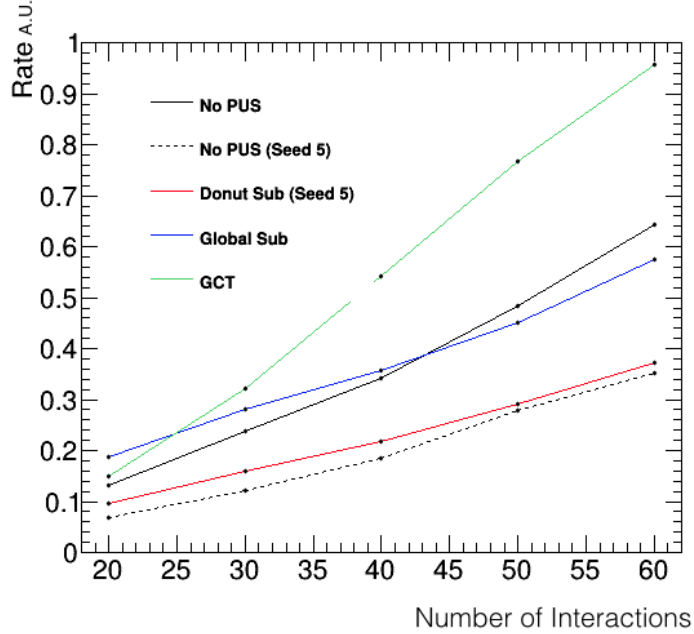


**Figure 5.15:** The dependence of the rate for a threshold of  $p_T^{L1} = 30 \text{ GeV}$  on the number of simultaneous interactions

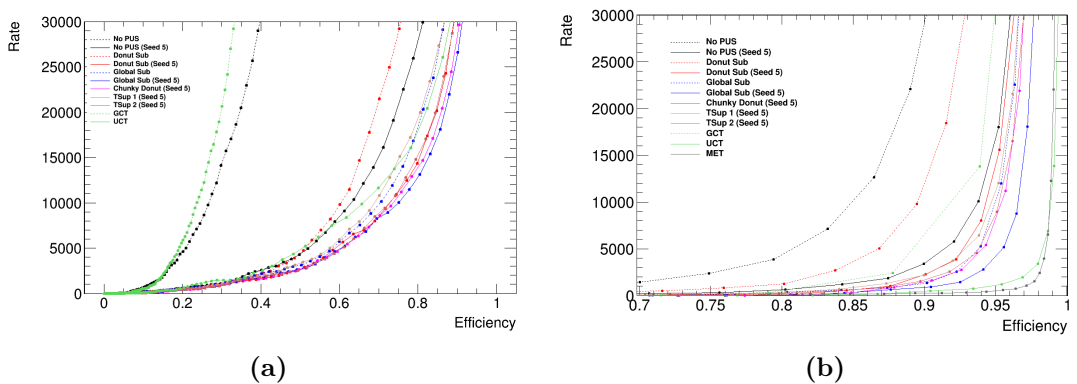


**Figure 5.16:** Rate (Hz) against efficiency for (a) L1  $H_T$  and (b) L1  $\mathcal{H}_T$ , both with a threshold of 200 GeV.

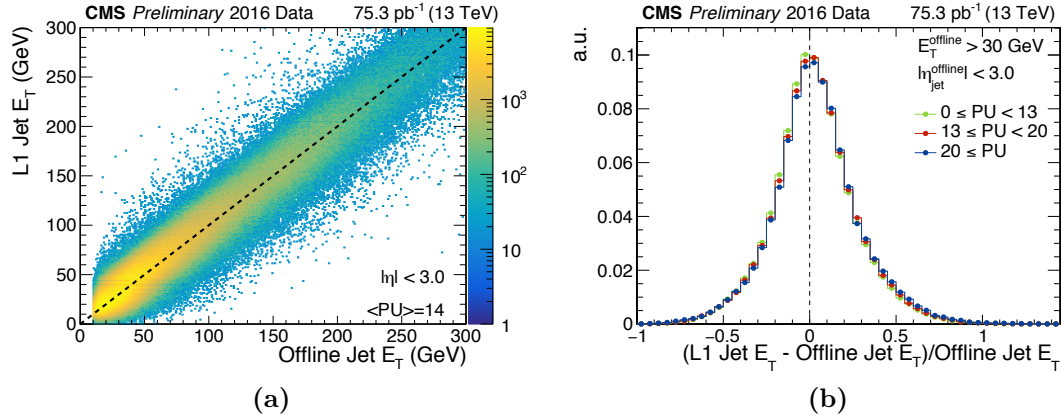


**Figure 5.17:** (a) The L1 jet energy compared to offline in early 2016 data for a wide range of jet energies. (b) Resolution for the L1 jet energy compared to offline in early 2016 data for several different pileup scenarios [87].

### 5.5.4 Summary

The performance plots described in this section have highlighted the importance of effective pileup subtraction for the L1 trigger. Significantly improved performance is observed over the legacy and UCT systems, highlighting the advantages of additional granularity and algorithmic complexity afforded by the upgraded architecture. The best performance is seen with the chunky doughnut (with a seed threshold) and global  $\rho$  pileup subtraction. Due to latency constraints and the desire to account for local effects when triggering, a local pileup subtraction algorithm is preferred. Therefore, the chunky doughnut subtraction has been used for data taking in 2016.

Figure 5.17 shows two example performance plots made using early 2016 data. The upgrade jet energy is seen to agree well with offline over a wide range of energies and shows little pileup dependence.

## 5.6 Cross-trigger study

The simple single object triggers considered in the previous section are useful for selecting high  $p_T$  signatures and for low luminosities. In order to provide efficiency for the full range of the CMS physics program at higher luminosities, sophisticated combinations of

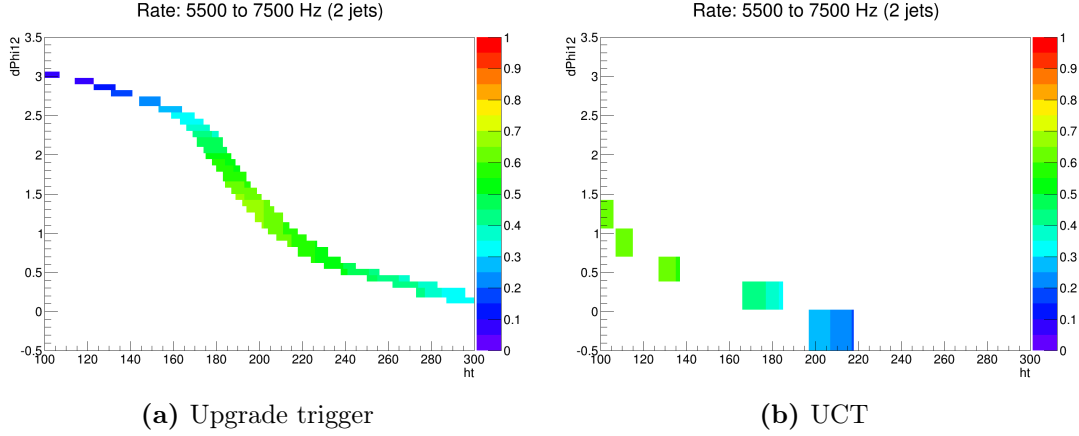


**Figure 5.18:** Efficiency of the dijet selection for hadronic offline requirement  $200 < H_T < 300 \text{ GeV}$  and  $\alpha_T > 0.65$  in a band of rate of 5.5 to 7.5 kHz

the single object triggers, ‘cross-triggers’, are required. In this section, the  $\alpha_T$  analysis is used to highlight the utility of such a cross-trigger at L1.

The  $\alpha_T$  analysis is detailed in Chapter 6. In order to maximise acceptance to supersymmetric models at lower energy scales, a low  $H_T$  threshold is required. However, without an additional requirement, the rate would be unacceptably high. A cross-trigger using a selection on both the difference in  $\phi$  between the two leading jets ( $\Delta\phi_{1,2}$ ) and  $H_T$  can control this rate while maintaining efficiency. The  $\Delta\phi_{1,2}$  requirement takes advantage of the high relative  $H_T$  to  $H_T$  for the signal models.

An acceptable rate for such a cross-trigger, given the overall budget of 100kHz, is around 5.5 to 7.5 kHz. This range defines a band in the plane of  $\Delta\phi_{1,2}$  and  $H_T$  in which the efficiency can be inspected. To avoid signal model dependence, the efficiency is measured using a  $t\bar{t}$  sample for the multijet case ( $n_{\text{jet}} \geq 4$ ) and a sample of Z boson production in association with jets, where the Z decays to neutrinos, for the dijet case ( $n_{\text{jet}} = 2$ ). An offline hadronic selection of  $200 < H_T < 300 \text{ GeV}$  and  $\alpha_T > 0.65$  is made in defining the efficiency. This approximates to the selection of the lowest  $H_T$  regions used in the  $\alpha_T$  search, for which achieving high efficiencies is most challenging. The results are shown for both the TMT and UCT trigger in Figures 5.18 and 5.19 for the dijet and multijet trigger respectively. For the TMT, chunky-doughnut-corrected, calibrated jets are used.

In both cases the greatly superior resolution afforded by the TMT allows a significantly more granular operating range than the UCT. Higher efficiencies, especially for the multijet

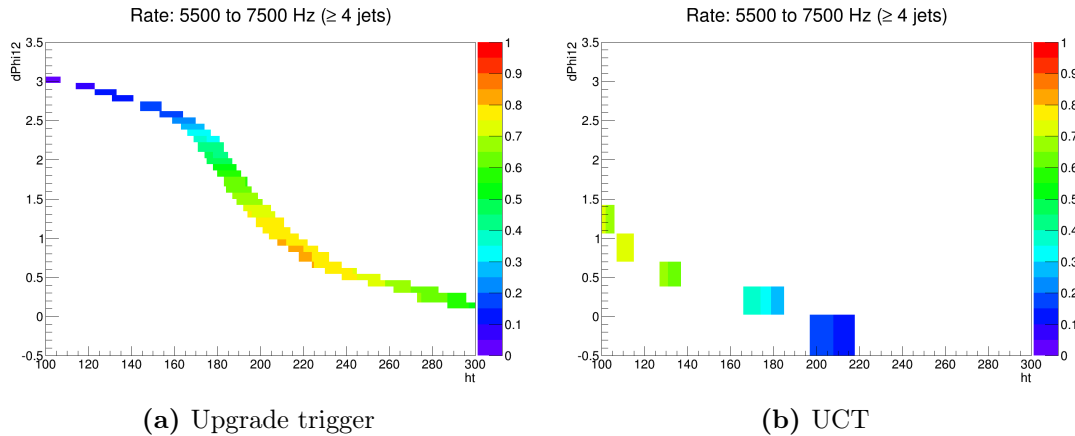


**Figure 5.19:** Efficiency of the multijet selection for hadronic offline requirement  $200 < H_T < 300$  and  $\alpha_T > 0.65$  in a band of rate of 5.5 to 7.5 kHz

topology, are achievable with the upgraded system. The maximal efficiency gain in using  $\Delta\phi_{1,2}$  to that using a  $H_T$  trigger alone may also be considered for the TMT. For the dijet case there is a significant efficiency gain from  $\sim 30\%$  to  $\sim 70\%$ , while for the multijet the gain is  $\sim 50\%$  to  $\sim 80\%$  when  $\Delta\phi_{1,2}$  is used in conjunction with  $H_T$ . This highlights the importance of cross triggers in controlling rates while keeping low offline thresholds.



# Chapter 6

## The $\alpha_T$ search

The  $\alpha_T$  analysis is a hadronic search for BSM physics targeting the pair-production of coloured SUSY particles that decay to the weakly interacting LSP.

Exploiting a hadronic final state requires effective background suppression and residual background prediction. During Run 1, the  $\alpha_T$  analysis strategy has been used for several searches for supersymmetry at both  $\sqrt{s} = 7\text{ TeV}$  and  $\sqrt{s} = 8\text{ TeV}$ , as well as a range of luminosities [88, 89, 90, 91]. For Run 2, the selections and categorisation have been updated to improve the sensitivity and acceptance of the search; they are detailed in this section.

The  $\alpha_T$  analysis ‘signal region’ is defined by selecting a final state including jets and significant  $\cancel{E}_T$  with no reconstructed leptons or photons. These selections provide sensitivity to hadronic SUSY models with significant  $\cancel{E}_T$  in the final state.

Background control is crucial in a search for BSM physics. To mitigate the otherwise dominant QCD multijet background, detailed in Section 6.1.1, dedicated dimensionless variables, defined in Section 6.2, are used to strongly suppress this process. In defining the signal region, additional hadronic, kinematic and cleaning selections are used for further QCD and electroweak background suppression; these are described in Section 6.4.1.

The determination of residual QCD multijet backgrounds as well as backgrounds with genuine  $\cancel{E}_T$  (described in Section 6.1.2) relies on data-driven techniques described in Chapter 7. These data-driven predictions use signal depleted ‘control regions’ enriched in a particular background process (or related process). All events used in the  $\alpha_T$  analysis pass a common preselection described in Section 6.3. Further selections in these control regions closely follow those in the signal region; they are detailed in Section 6.4.2.

As discussed in Chapter 5, an effective trigger strategy is critical to ensure acceptance for signals such as compressed SUSY models which can have relatively low  $H_T$  but significant  $\mathcal{H}_T$ . The trigger strategy for the signal and control regions is discussed in Section 6.6.

To inclusively optimise sensitivity, the events that pass the signal region requirements must be categorised to allow significant signal contributions for a wide range of models. Several variables are used, as detailed in Section 6.5, to categorise the signal region.

## 6.1 Backgrounds for hadronic searches

### 6.1.1 The QCD multijet background

The QCD multijet background from inelastic scattering is dominant in hadronic searches at the LHC. The final state is typically a balanced dijet event with no weakly interacting particles in the final state. Higher jet multiplicity events are rarer but also possible.

While the events contain no ‘true’  $\cancel{E}_T$  from weakly interacting particles (except for ‘heavy flavour’ QCD, see below), fluctuations in detector response and reconstruction can cause a small fraction of the QCD events to gain significant ‘fake’  $\cancel{E}_T$ . These form a dominant background as the total QCD cross section is up to  $\sim 7$  orders of magnitude larger than that of the SM backgrounds containing true  $\cancel{E}_T$  (see Section 6.1.2) [92]. The main detector and reconstruction mechanisms that introduce fake  $\cancel{E}_T$  are summarised below:

- Detector inefficiencies due to regions with reduced or no response (‘dead cells’) can cause a significant proportion of the energy of any incident physics object to be lost. If the true event is balanced, losses which are caused by detector inefficiency will contain a  $\cancel{E}_T$  vector which points approximately in the  $\phi$  direction of the problematic region.
- Misreconstruction due to effects such as tracking errors, incorrect object identification and under/overcorrection of jets when calibrating. This may apply to one or more objects in the event. If the underlying event is balanced, the  $\cancel{E}_T$  vector will typically point in the direction of the misreconstructed object in cases of underestimation or in the opposite direction in cases of overestimation.

- Additional energy can be added to the event due to effects such as ‘hot cells’ that consistently record energy depositions without incident particles in the ECAL or HCAL, spontaneous discharges and direct particle interactions with detector electronics or photomultipliers.
- The ‘beam halo’ of charged particles around the LHC beam, caused mainly by proton scattering off the LHC collimators, may interact with muon chambers, causing fake muons to be reconstructed, or may deposit energy in the calorimeters as they traverse the detector [93]. The beam halo has the largest effect for  $\phi = 0$  and  $\phi = \pi$  as the constituent particles tend to lie within the plane of the LHC ring.
- Imbalance may be introduced by acceptance effects. If physics objects are excluded from the calculation of energy sums due to thresholds in quantities such as  $p_T$  or  $\eta$ ,  $\cancel{E}_T$  will be introduced. These thresholds are typically required because of imperfect detector coverage or to remove objects reconstructed from effects such as detector noise or pileup.

In addition to QCD multijet events with fake  $\cancel{E}_T$  discussed above, QCD scattering processes may produce events containing true  $\cancel{E}_T$ . This is due to the rare production of heavy-flavour quarks which decay via leptons and neutrinos. These events pass hadronic selection as the leptons from heavy-flavour decay are usually confined within the jet cone and fail isolation requirements. In such cases the  $\cancel{E}_T$  vector is typically closely aligned with the  $\phi$  direction of the jet.

### 6.1.2 Electroweak backgrounds

There are several SM processes which include  $\cancel{E}_T$  from neutrinos in the final state and can form backgrounds for hadronic searches (labelled as electroweak backgrounds). The dominant electroweak backgrounds are  $W + \text{jets}$ ,  $t\bar{t} + \text{jets}$  and  $Z + \text{jets}$ . The  $\alpha_T$  signal region, defined fully in Section 6.4.1, selects purely hadronic events containing reconstructed jets and  $\cancel{E}_T$ . An overview of the electroweak background processes and the mechanisms by which they may enter into the signal region is given below.

#### $Z + \text{jets}$ background

The largest background process in the signal region comes from  $Z$  boson production in association with jets ( $Z + \text{jets}$ ) followed by decay to neutrinos,  $Z \rightarrow \nu\bar{\nu}$ . This process is an ‘irreducible’ background as the neutrinos produce significant  $\cancel{E}_T$  in the final state

with no associated leptons. Across the signal region,  $Z \rightarrow \nu\bar{\nu}$  contributes  $\sim 50\%$  of the overall background. The decay of the  $Z$  boson to leptons,  $Z \rightarrow \ell\ell$  may also introduce  $\cancel{E}_T$  if one or both of the leptons is not reconstructed (lost). Due to the low probability of losing both leptons in the event, this is a subdominant background, comprising  $\sim 0.5\%$  of the signal region.

### **W + jets background**

The production of a W boson in association with jets (W + jets) where the W boson decays leptonically ( $W \rightarrow l\nu$ ) comprises  $\sim 40\%$  of the overall background in the signal region. Such events pass hadronic selection if the lepton is not reconstructed. This lost lepton background may be introduced if the lepton falls out of acceptance, fails isolation requirements or is otherwise misreconstructed. Both the lost lepton and the neutrino in the event may contribute to the  $\cancel{E}_T$ . The branching fraction for a W boson decaying to a hadronically decaying  $\tau$  is  $\sim 6\%$ . In such events the associated  $\tau$  neutrino may introduce significant  $\cancel{E}_T$ . If the hadronic decay products are reconstructed as a jet, these events may pass the signal region selection. To reduce this background, a single isolated track veto is used to reject single-prong decays of the  $\tau$  ( $\tau^\pm \rightarrow \pi^\pm + n\pi^0\nu$ ) which comprise  $\sim 70\%$  of the hadronic  $\tau$  decays.

### **t $\bar{t}$ + jets and single top background**

The t $\bar{t}$  + jets and single top background comprise around 5% and 0.5% of the overall background respectively. On production, the top quark will predominantly decay via the weak force as  $t \rightarrow W + b$ . The W boson may then decay hadronically, producing a final state with multiple jets, or leptonically, producing a final state including a lepton and a neutrino.

The final state in an event with t $\bar{t}$  + jets production will include two bottom quarks as well as multiple jets and/or significant  $\cancel{E}_T$ , depending on the decay. If both W bosons decay hadronically ( $\sim 45.7\%$  of t $\bar{t}$  decays), up to six jets may be produced from the hadronisation of the quarks. In this case the  $\cancel{E}_T$  may be introduced via jet mismeasurement or from bottom quark decay via neutrinos. If one of the W bosons decays leptonically ( $\sim 45.8\%$  of t $\bar{t}$  decays), up to four jets may be expected as well as  $\cancel{E}_T$  from the neutrino. Such events may enter hadronic selection if the lepton is lost. Finally, if both W bosons decay leptonically ( $\sim 10.5\%$  of t $\bar{t}$  decays), the final state contains two

leptons and significant  $\cancel{E}_T$ . This mode is subdominant due to the low probability of losing both leptons and the lack of jets in the final state. For all decay modes, the number of jets reconstructed in the event may be increased by processes such as ISR/FSR and pileup.

The  $\alpha_T$  analysis categorises events using the number of reconstructed jets identified as originating from bottom quarks. The  $t\bar{t}$  background is particularly enriched for  $n_b \geq 2$ , comprising  $\sim 60\%$  of the background for such events.

Single top production occurs mainly via t-channel in association with a quark, production in association with a W boson (tW), or s-channel in association with a bottom quark, with approximate proportions 72.5, 24 and 3.5% respectively. As for  $t\bar{t} + \text{jets}$ , the single top background is enhanced for categorisations with at least two reconstructed bottom quarks, rising to  $\sim 5\%$  of the total for such events.

### Residual electroweak backgrounds

In addition to the backgrounds discussed above, there are several processes which make minor contributions to the signal region (which can be enhanced for particular categorisations). Such residual backgrounds include  $t\bar{t}$  production in association with a vector boson,  $t\bar{t}V$  ( $\sim 0.1\%$  of the total background and  $\sim 4\%$  of the total background for an  $n_b \geq 2$  selection); pair production of vector bosons, ZZ, WZ and WW ( $\sim 1.4\%$  of the total background); production of a (lost) photon in association with jets ( $\sim 0.7\%$  of the overall background) and leptonic decays of the Z with two lost leptons ( $\sim 0.5\%$  of the overall background).

## 6.2 Suppression of the QCD multijet background

Predicting the QCD backgrounds presents significant challenges, discussed in Section 7.3.2, which can introduce large uncertainty in the background estimation. A distinguishing feature of the  $\alpha_T$  analysis is the aim to mitigate this uncertainty by reducing the QCD multijet background to under 10% of the total in each category of the analysis. This is achieved using selections on the dedicated variables  $\alpha_T$ ,  $\Delta\phi_{\min}^*$ ,  $H_T/\cancel{E}_T$  and the forward jet veto. This section describes how these variables reject QCD events by exploiting the topologies and features of such events. Further event filters that specifically target

events containing  $\cancel{E}_T$  introduced by known detector problems and beam halo effects are discussed in Section 6.3.2.

### 6.2.1 $\alpha_T$

The  $\alpha_T$  variable is designed to reject balanced events which gain significant  $\cancel{E}_T$  through jet mismeasurement. The  $\alpha$  variable was initially proposed in [94] and converted into the transverse variable,  $\alpha_T$ , to allow use with hadronic collisions. The absolute value of the  $\cancel{E}_T$  is sensitive to the detector and reconstruction effects discussed in Section 6.1.1. The  $\alpha_T$  variable is designed to be dimensionless such that the topology of the event is used to reject QCD processes, regardless of the total value of the  $\cancel{E}_T$ .

For a dijet event,  $\alpha_T$  is defined as

$$\alpha_T = \frac{E_T^{j_2}}{M_T}, \quad (6.1)$$

where  $E_T^{j_2}$  is the transverse energy of the less energetic jet and  $M_T$  is the transverse mass of the dijet system,

$$M_T = \sqrt{\left(\sum_{i=1}^2 E_T^{j_i}\right)^2 - \left(\sum_{i=1}^2 p_x^{j_i}\right)^2 - \left(\sum_{i=1}^2 p_y^{j_i}\right)^2}. \quad (6.2)$$

where  $E_T^{j_i}$  is the transverse energy of jet  $j_i$  ( $E_T^{j_i} = E^{j_i} \sin \theta^{j_i}$ ), and  $p_x^{j_i}$  and  $p_y^{j_i}$  are the  $x$  and  $y$  components of the transverse momentum of the jet.

For events with three or more jets, a pseudo-dijet system is defined where all possible vectorial sums of the jets into two pseudo-jets are considered. The combination into pseudo-jets with the smallest difference in transverse energy,  $\Delta E_T$ , is chosen as the most balanced configuration and used to define  $\alpha_T$ . The  $M_T$  for the event is insensitive to the clustering and is given by

$$M_T = \sqrt{\left( \sum_{i=1}^2 E_T^{j_i} \right) - H_T^2}. \quad (6.3)$$

where the sum is over all jets in the event. The sub-leading pseudo-jet energy,  $E_T^{j'_2}$ , is given by

$$E_T^{j'_2} = \frac{\sum_i E_T^{j_i} - \Delta E_T}{2}. \quad (6.4)$$

The definition of  $\alpha_T$  for any number of jets is therefore

$$\alpha_T = \frac{\sum_i E_T^{j_i} - \Delta E_T}{2\sqrt{\left(\sum_i E_T^{j_i}\right)^2 - H_T^2}}. \quad (6.5)$$

Most jets in the event contain significant boost such that  $E_T \sim p_T$ . The  $\alpha_T$  definition can be approximated in this case by

$$\alpha_T \approx \frac{H_T - \Delta H_T}{2\sqrt{H_T^2 - H_T^2}}. \quad (6.6)$$

where  $\Delta H_T$  is the difference in  $p_T$  of the pseudo-jets.

To illustrate the mechanism by which the  $\alpha_T$  variable rejects  $Z_T$  from mismeasured or lost jets, consider a dijet event as shown in Figure 6.1. Three possible event topologies are shown: a perfectly balanced event (left), a perfectly balanced event with a mismeasured jet (middle) and an event containing true  $Z_T$  (right). In a balanced dijet event without mismeasurement,  $\Delta E_T = H_T = 0$  and the value of  $\alpha_T$  will be 0.5. If one of the jets is undermeasured or overmeasured for an otherwise balanced dijet event,  $\Delta H_T = H_T$  and Equation 6.6 can be written as

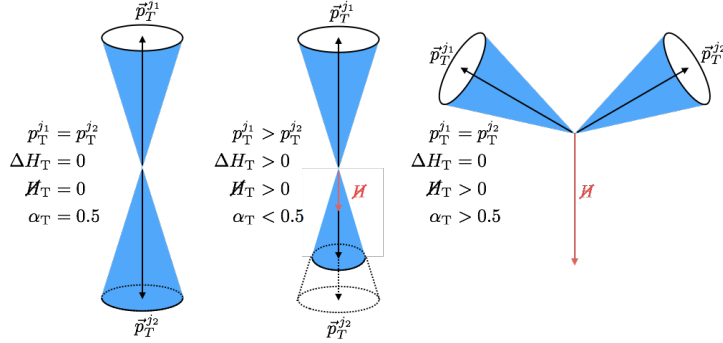


**Figure 6.1:** The  $\alpha_T$  variable inputs and values for three types of event: balanced and well measured jets (left), balanced jets with a mismeasured jet (middle) and well measured jets recoiling against true  $\cancel{E}_T$  (right). The solid cones signify the reconstructed jet momentum while the dashed cones represent the true momentum. The calculation of  $\alpha_T$  is described in the text.

$$\alpha_T \approx \sqrt{\left( \frac{H_T^2 - \cancel{H}_T^2}{2H_T^2 + \cancel{H}_T^2} \right)} < 0.5. \quad (6.7)$$

Conversely, if an event contains true  $\cancel{E}_T$  and the jets are recoiling against significant  $\cancel{E}_T$  (which is not aligned with one of the jets in the event), as shown on the right of Figure 6.1,  $\alpha_T > 0.5$ .

In the general case of two or more jets, for events containing  $\cancel{E}_T$  from mismeasurement or neutrinos produced in heavy-flavour decays, the values of  $\Delta E_T$  and  $H_T$  are highly correlated, leading to values of  $\alpha_T \leq 0.5$ . This correlation is much weaker in the case of pair-produced, R-parity conserving SUSY events, where each decay chain ends in the undetected LSP, and for the electroweak backgrounds, allowing  $\alpha_T > 0.5$ .

The  $\alpha_T$  distribution is shown in Figure 6.2. The region of  $\alpha_T < 0.5$  is dominated by QCD multijet events. This contribution sharply drops as  $\alpha_T$  increases above 0.5. Multijet events with very rare large stochastic fluctuations in the measured jet energies can lead to values of  $\alpha_T$  above 0.5. QCD multijet events may also have  $\alpha_T$  values larger than 0.5 if the  $p_T$  of one or more jets is sufficiently different from  $E_T$ , breaking the assumption required for the approximate equality in Equation 6.7. However, this is found to have  $< 1\%$  effect on the number of QCD multijet events passing  $\alpha_T > 0.5$ . The  $\alpha_T$  distribution becomes more sharply peaked with increasing  $H_T$  in the event as mismeasurements are larger for lower jet  $p_T$ . Significantly larger values of  $\alpha_T$  for QCD

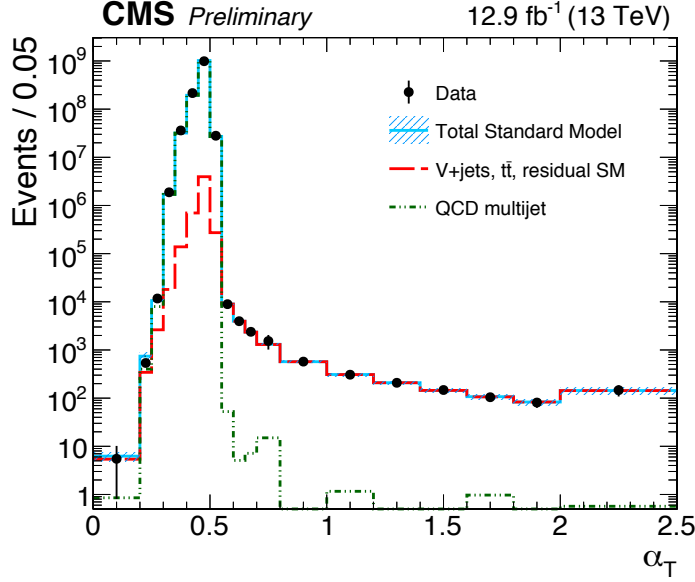


**Figure 6.2:** The  $\alpha_T$  distribution observed in data compared to simulation. The statistical uncertainties for the QCD multijet and electroweak backgrounds are represented by the hatched areas. The final bin of each distribution contains the overflow events. The events below  $\alpha_T = 0.55$  use unbiased triggers with a loose preselection while events above  $\alpha_T = 0.55$  use the signal region triggers and selection.

multiparticle events can also be caused by hot cells or acceptance effects. These are mitigated by the other discriminating variables discussed below and dedicated event filters.

Unlike the QCD processes, the electroweak backgrounds have a long tail in values of  $\alpha_T$  greater than 0.5. The  $\alpha_T$  variable allows a powerful discrimination between the otherwise dominant QCD background and processes with  $\cancel{E}_T$  well separated from the jets.

### 6.2.2 $\Delta\phi_{\min}^*$

The  $\Delta\phi_{\min}^*$  variable is an additional topological variable designed to mitigate contamination from mismeasured events (from reconstruction and instrumental issues) and semileptonic heavy-flavour decays. The variable is defined as follows:

- Each jet in the event is considered in turn as the probe jet,  $j_i$ .
- The  $\vec{H}_T$  is recalculated with the probe jet removed,  $\vec{H}_T^{j_i}$ .
- The azimuthal separation of the probe jet and  $\vec{H}_T^{j_i}$  is calculated,  $\Delta\phi_i$ .

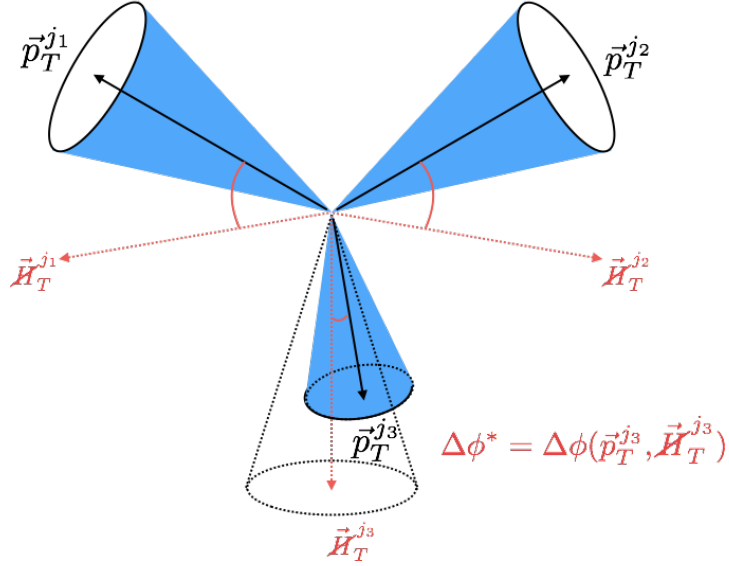


**Figure 6.3:** The  $\Delta\phi_{\min}^*$  variable inputs and values for a mismeasured balanced three jet event. The third jet minimises the  $\Delta\phi_i$  and is used to calculate  $\Delta\phi_{\min}^*$  as described in the text.

- The  $\Delta\phi_{\min}^*$  is calculated as the minimal  $\Delta\phi_i$  over all jets in the event,

$$\Delta\phi_{\min}^* = \min_{\forall i \in [1, n_{\text{jet}}]} \Delta\phi_i. \quad (6.8)$$

If the  $\Delta\phi_{\min}^*$  value is close to the jet cone size, the jet which minimizes  $\Delta\phi_i$  ( $j_{\Delta\phi_{\min}^*}$ ) is likely to be mismeasured or to contain  $E_T$  from a leptonic decay of a heavy-flavour quark. The  $\Delta\phi_{\min}^*$  variable is insensitive to the  $p_T$  of  $j_{\Delta\phi_{\min}^*}$  and rejects events containing a jet whose  $p_T$  is either overmeasured or undermeasured. The jets in the electroweak background processes and signal models typically recoil against the  $E_T$ , implying larger values of  $\Delta\phi_{\min}^*$ . The calculation of  $\Delta\phi_{\min}^*$  for a mismeasured balanced event containing three jets is shown in Figure 6.3. In the  $\alpha_T$  analysis, a threshold of 0.5 is used to reject QCD multijet events.

The  $\Delta\phi_{\min}^*$  variable cannot be defined in the monojet category. For events in this category containing additional jets with  $p_T > 25 \text{ GeV}$ , the  $\Delta\phi_{\min}^*$  variable is defined including these jets. For events with no addition jets with  $p_T > 25 \text{ GeV}$ , no threshold on  $\Delta\phi_{\min}^*$  is used.

The distribution of  $\Delta\phi_{\min}^*$  in data and simulation for  $H_T > 800 \text{ GeV}$  is shown in Figure 6.4. The QCD multijet background is seen to decrease by around five orders of

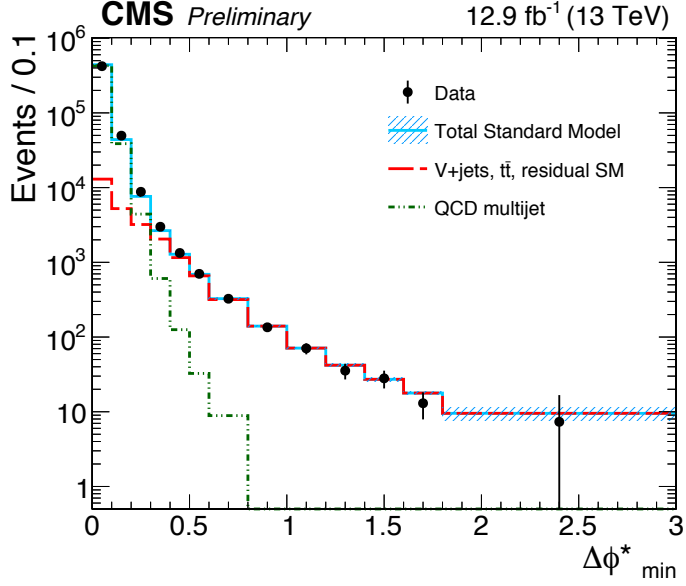


**Figure 6.4:** The  $\Delta\phi_{\text{min}}^*$  distribution observed in data compared to simulation for a selection  $H_T > 800 \text{ GeV}$ . The statistical uncertainties for the multijet and SM expectations are represented by the hatched areas.

magnitude as  $\Delta\phi_{\text{min}}^*$  increases to 0.5. In Figure 6.4 the electroweak backgrounds are shown to have long tails up to  $\Delta\phi_{\text{min}}^* = \pi$ .

### 6.2.3 $\mathcal{H}_T/\mathcal{E}_T$

The  $\mathcal{H}_T/\mathcal{E}_T$  cleaning cut is designed to reduce the contamination from balanced events which contain significant  $\mathcal{H}_T$  due to acceptance effects from kinematic and pseudorapidity thresholds, severe jet mismeasurement and particles not clustered into jets. The PF  $\mathcal{E}_T$  is more robust against acceptance effects as all PF candidates are included in its computation. The contamination due to such effects may therefore be mitigated using a maximal threshold on the ratio of the  $\mathcal{H}_T$  to the  $\mathcal{E}_T$ .

### 6.2.4 Forward jet veto

The  $\mathcal{H}_T$  variable is made using jets with  $|\eta| < 2.4$ . Jets in the forward pseudorapidity region may introduce  $\mathcal{H}_T$ . A veto on any jet in the forward region with  $p_T > 40 \text{ GeV}$  is used to reject such events.

## 6.3 Preselection

The objects described in Section 4.4 are used to define a common kinematic preselection for the signal and control regions used in the  $\alpha_T$  analysis. The kinematic selections as well as event filters and vetoes targeting known instrumental, reconstruction and beam effects are described in this section.

### 6.3.1 Kinematic selections

The minimal requirements on the energy sums for both the signal and control regions are  $H_T > 200 \text{ GeV}$  and  $\cancel{H}_T > 130 \text{ GeV}$ . In addition, at least one jet satisfying the requirements detailed in Table 4.4 is required. These selections are designed by considering trigger efficiency constraints while maximising acceptance for signal models with small mass splittings.

### 6.3.2 Event filters

Event filters reject events contaminated by detector or reconstruction effects which can cause significant  $\cancel{E}_T$ . Such effects may not be known when the background simulations are produced or can be difficult to simulate. Therefore, dedicated filters are used to remove such events from the dataset. These ‘ $\cancel{E}_T$  filters’ are:

- The HBHE noise and isolation filters that rejects energy spikes in The HCAL caused by noise from sources including direct particle interactions with HCAL instrumentation.
- The EE bad supercluster filter that removes events containing TeV scale energy spikes from anomalous pulses in the EE.
- The CSC beam halo filter that uses the CSC to measure halo muons and reject events containing significant contamination from the beam halo.
- The ECAL trigger primitive filter that rejects events where significant energy is deposited in dead cell regions.
- The PV filter that requires at least one well reconstructed vertex, which ensures collisions have occurred (rather than an event triggered and reconstructed from detector noise).

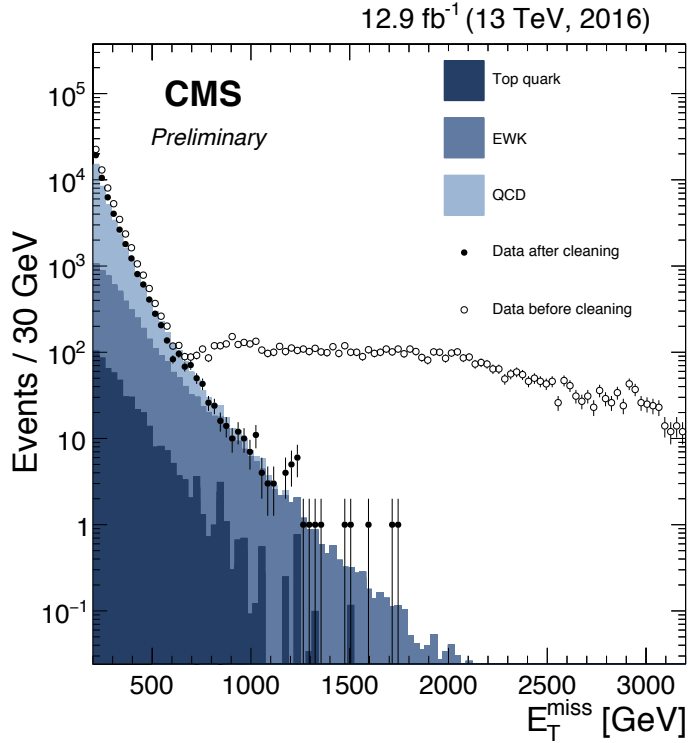


**Figure 6.5:** The  $E_T$  filters remove the long tail in the reconstructed  $E_T$  caused by detector, reconstruction and beam effects in the data [76].

- The bad muon and bad charged hadron filters that reject events containing poorly reconstructed muons reconstructed as a muon or PF charged hadron respectively.

The performance of the  $E_T$  filters for the reconstructed  $E_T$  in the data is shown in Figure 6.5. The long tail caused by the effects in data discussed above is mitigated by the filters. In addition to the  $E_T$  filters, additional vetoes are used by the  $\alpha_T$  analysis to reject events affected by misreconstruction and residual beam halo, as follows:

- A leading jet charged hadron energy fraction (CHF) veto that rejects events contaminated by beam halo energy deposits which pass the CSC beam halo filter. The lead jet in the event is required to satisfy  $\text{CHF} > 0.1$ .
- The odd jet veto that rejects any event containing a jet which fails the requirements in Table 4.1. Such events are often caused by noise or misreconstruction.
- The forward jet veto, described in Section 6.2.4, rejects events containing jets which fall out of acceptance but are reconstructed in the forward region.
- The  $H_T/E_T < 1.25$  requirement, described in Section 6.2.3, rejects events containing  $H_T$  due to energy present in the event that is not clustered into jets.

## 6.4 Analysis selections

The common preselections are applied for all events used by the  $\alpha_T$  analysis. The events passing these selections may then fall into the signal region or the hadronic,  $\gamma + \text{jets}$ ,  $\mu + \text{jets}$  or  $\mu\mu + \text{jets}$  control region. These regions are exclusive so that no event may be double counted; the selections for each are summarised below.

### 6.4.1 Hadronic signal region

Events in the signal region are categorised (see Section 6.5) and used to search for signatures of new physics (see Chapter 8). Selections are designed to suppress the QCD multijet and electroweak backgrounds while maintaining acceptance to hadronic SUSY models containing significant  $\cancel{E}_T$ .

The QCD multijet background is suppressed using thresholds on the  $\alpha_T$ ,  $\Delta\phi_{\min}^*$  and  $H_T/\cancel{E}_T$  variables and event filters. An  $H_T$  dependent threshold is used to account for the broadening  $\alpha_T$  distribution for lower  $H_T$  values. These thresholds are also chosen to be efficient given the trigger requirements (see Section 6.6) and are shown in Table 6.1. The highest threshold of 0.65 is used for  $200 < H_T < 300$  GeV while there is no  $\alpha_T$  requirement for  $H_T > 800$  GeV, for which region a pure  $H_T$  trigger is used. At least two jets are required to define  $\alpha_T$  and therefore no threshold is used in events containing only one jet (monojet).

**Table 6.1:**  $\alpha_T$  thresholds versus lower bound of  $H_T$  bin in units of GeV. For all  $H_T$  bins satisfying  $H_T > 800$  GeV, no  $\alpha_T$  cut is applied. No  $\alpha_T$  requirement is imposed in the monojet bins.

$H_T$	200	250	300	350	400	500	600	$>800$
$\alpha_T$ threshold	0.65	0.60	0.55	0.53	0.52	0.52	0.52	–

A  $\Delta\phi_{\min}^*$  threshold of 0.5 is used for all events passing signal region selection. This value is motivated by the jet cone size of 0.4 and desired level of QCD suppression. For monojet events, the  $\Delta\phi_{\min}^*$  variable is defined using all jets with  $p_T > 25$  GeV. If there are no such jets, no threshold on  $\Delta\phi_{\min}^*$  is used.

The values of the thresholds on  $\alpha_T$ ,  $\Delta\phi_{\min}^*$  and  $H_T/\cancel{E}_T$  provide the desired level of QCD multijet contamination, measured in data, of  $< 10\%$  (see Section 7.3.2). This level

of QCD rejection is unique for the  $\alpha_T$  analysis among hadronic SUSY searches. Given the difficulties in predicting residual QCD backgrounds (see Section 7.3.2), the  $\alpha_T$  strategy can provide a robust confirmation of a potential discovery.

### 6.4.2 Control regions

The control regions are used to predict both the residual QCD multijet and electroweak backgrounds. The predictions are made using the ‘transfer factor’ (TF) method, as described in Section 7.3.1. Each of the control regions is enriched in the background sample(s) predicted by that control region or a related process. The selections used are described in this section and are designed to be as close to the signal region selections as possible while ensuring a large sample of events enriched in the relevant process.

#### Hadronic control regions

The hadronic control regions are used to determine the level of QCD contamination remaining in the signal region (see Section 7.3.2). These are defined by inverting the selection on the discriminating variables described in Section 6.2 to give a data sample dominated by events from QCD processes. Any event containing a reconstructed photon or lepton is vetoed.

#### Photon control region

The  $\gamma + \text{jets}$  control region is used to predict the  $Z \rightarrow \nu\bar{\nu}$  background in the signal region. One photon satisfying the requirements in Table 4.4 is required in the event and events containing leptons are vetoed. The energy sums are then calculated without this photon. To reduce the reliance on simulation, all signal region selections are made except for those on the  $\Delta\phi_{\min}^*$  variable. These requirements are removed to enhance the statistics in the control region sample for predicting the  $Z \rightarrow \nu\bar{\nu}$  background. Due to trigger considerations, the  $\gamma + \text{jets}$  control region is used for  $H_T > 400 \text{ GeV}$  only. To ensure the photon is not affected by hadronic activity, any events with a jet satisfying  $\Delta R(j, \gamma) < 1$  are vetoed. Finally, the  $\cancel{H}_T > 130 \text{ GeV}$  threshold in both signal and control helps ensure the bosons are sufficiently boosted such that the  $Z$  boson mass does not bias the prediction of  $Z \rightarrow \nu\bar{\nu}$  using the  $\gamma + \text{jets}$  control region.

### Muon control regions

The muons used for the muon control regions are defined as detailed in Table 4.4. Energy sums are defined without including the muon and all selections except for those on the  $\Delta\phi_{\min}^*$  and  $\alpha_T$  variables are used. Events are vetoed if  $\Delta R(j, \mu) < 0.5$  for all jets and muons in the event to ensure no hadronic activity affects the muon(s). Events are also rejected if they contain an electron or photon.

The  $\mu + \text{jets}$  control region is used to predict the lost lepton background from a sample rich in  $W + \text{jets}$  and  $t\bar{t}$  processes. A single muon is required and a selection is used on the transverse mass variable,  $M_T(\mu, \cancel{E}_T) \equiv \sqrt{2E_T^\mu \cancel{E}_T(1 - \cos(\Delta\phi_{\mu, \cancel{E}_T}))}$ , of  $M_T(\mu, \cancel{E}_T) < 125 \text{ GeV}$  to enrich the sample with the  $W + \text{jets}$  background and to reduce potential contamination from SUSY signal models.

The  $\mu\mu + \text{jets}$  control region is used along with the  $\gamma + \text{jets}$  control region to predict the  $Z \rightarrow \nu\bar{\nu}$  background using a sample rich in the  $Z(\rightarrow \mu\mu) + \text{jets}$  process. Exactly two oppositely charged muons are required with an invariant mass within 25 GeV of the mass of the  $Z$  boson,  $|M_{\mu_1, \mu_2} - m_Z| < 25 \text{ GeV}$ .

## 6.5 Categorisation

In order to maintain sensitivity to a wide range of signal models, events are categorised using several discriminating variables. This categorisation allows sensitivity to a wide range of hadronic signal models.

The  $\alpha_T$  analysis uses a categorisation in  $n_{\text{jet}}$ ,  $n_b$  and  $H_T$  for both the signal and control regions. Each signal region category is therefore predicted using an identical selection in these variables for the control region. In determining the categorisation, sufficient control region statistics are required to predict each  $n_{\text{jet}}$ ,  $n_b$  and  $H_T$  bin. The signal region is further categorised according to  $\cancel{H}_T$ . The categorisations and motivations are detailed below.

### 6.5.1 Categorisation in $n_{\text{jet}}$

The  $\alpha_T$  analysis categorises events into three topologies, ‘monojet’, ‘asymmetric’ and ‘symmetric’, using selections on the second jet  $p_T$ . For all topologies, the leading jet must satisfy  $p_T^{j_1} > 100 \text{ GeV}$ .

The monojet topology vetoes events containing a second jet with  $p_T^{j_2} > 40 \text{ GeV}$  and is designed to target compressed SUSY models. For such models the LSP carries the majority of the energy from the heavy sparticle decay, meaning any jets produced in the decay are soft (small values of  $p_T$ ). These events may fall into the monojet category if one of the incoming/outgoing partons radiate a jet. The monojet topology rejects backgrounds from  $t\bar{t}$  which tends to have high  $n_{\text{jet}}$  multiplicities.

The asymmetric topology selects events containing a second jet with  $40 \text{ GeV} < p_T^{j_2} < 100 \text{ GeV}$ . This category targets compressed SUSY models whose decay products are soft but can be reconstructed. In the presence of a boosted ISR/FSR such an event may have significant imbalance between the  $p_T$  of the ISR/FSR jet and the soft jets from the sparticle decay.

Finally, the symmetric topology requires  $p_T^{j_2} > 100 \text{ GeV}$  and targets more generic supersymmetric models with large mass splittings for which the decay products carry significant energies.

The jet multiplicity varies widely depending on the signal model and background process. Supersymmetric models of light flavoured squark production and compressed models tend to produce a small number of jets with significant energy. Conversely, uncompressed models of gluino or top squark production have larger jet multiplicities. The backgrounds are also largely  $n_{\text{jet}}$  dependent as  $t\bar{t}$  decays typically produce high multiplicities while decays of vector boson backgrounds produce low multiplicities. The events with a symmetric topology are therefore categorised according to  $n_{\text{jet}} = 2, 3, 4$  and  $n_{\text{jet}} \geq 5$ .

### 6.5.2 Categorisation in $n_b$

A categorisation on  $n_b$  improves sensitivity to models containing direct and indirect decays via heavy-flavour squarks. Such models are favoured as they naturally predict a light Higgs mass (see Chapter 2) and can produce final states including two to four bottom quarks, depending on the decay mode. Events are categorised as  $n_b = 0, 1, 2$  and

$n_b \geq 3$ . The dominant background for events with more than one b jet comes from the  $t\bar{t}$  process. The misidentification of jets from light-flavoured quarks as b jets increases the background rate for a high  $n_b$  selection.

### 6.5.3 Categorisation in $H_T$

The  $H_T$  produced in an event provides a measure of the mass scale of new physics models as the energy provided to the visible decay products is dependent on the mass splitting between the heavy sparticle and LSP. The finest control and signal region binning in  $H_T$  is shown in 6.1. These are merged from above depending on the requirement of at least one control region event observed in data per  $H_T$  region to allow a meaningful prediction.

### 6.5.4 Categorisation in $\mathcal{H}_T$

The categorisation in  $\mathcal{H}_T$  was introduced for the first analysis on Run 2 data. The  $\mathcal{H}_T$  modelling in the signal region is taken from simulation and a data-driven approach is utilised to validate this modelling using the data in the control regions as described in Section 7.5.

The  $\mathcal{H}_T$  variable is dependent on the energy carried by the invisible decay product of any BSM physics model (such as the LSP in SUSY models). For compressed models, the categorisation in both  $H_T$  and  $\mathcal{H}_T$  provides additional sensitivity as, unlike the SM backgrounds, such models tend to have  $\mathcal{H}_T$  values near  $H_T$ .

In determining the categorisation, a maximum statistical uncertainty from the simulated events of 50% (corresponding to four unweighted events) is required in each bin of the template in order to ensure a statistically meaningful prediction. In addition, a minimum bin width constraint of 50 GeV is applied in order to reduce bin-by-bin migration due to the finite  $\mathcal{H}_T$  resolution.

### 6.5.5 Summary

In Table 6.2, the lower bounds of the first and final  $H_T$  bins for each jet category are shown. The categories are further binned in  $\mathcal{H}_T$  according to the metric defined in Section 6.5.4.

**Table 6.2:** Summary of the lower bounds of the first and final bins in  $H_T$  (the latter in parentheses) in units of GeV as a function of  $n_{\text{jet}}$  and  $n_b$ . Intermediate  $H_T$  bins are taken from the values shown in Table 6.1.

$n_{\text{jet}} \setminus n_b$	0	1	2	$\geq 3$
<b>Monojet</b>				
1	200 (600)	200 (500)	-	-
<b>Asymmetric</b>				
2	200 (600)	200 (500)	200 (400)	-
3	200 (600)	200 (600)	200 (500)	200 (300)
4	200 (600)	200 (600)	200 (600)	250 (400)
$\geq 5$	250 (600)	250 (600)	250 (600)	300 (500)
<b>Symmetric</b>				
2	200 (800)	200 (800)	200 (600)	-
3	200 (800)	250 (800)	250 (800)	- (250)
4	300 (800)	300 (800)	300 (800)	300 (800)
$\geq 5$	350 (800)	350 (800)	350 (800)	350 (800)

## 6.6 Trigger strategy

### 6.6.1 Hadronic signal and control regions

The trigger strategy is designed to maximise acceptance for an inclusive set of new physics models which may be produced at a low energy scale. A suite of dedicated cross triggers is used at the HLT to achieve efficiencies near 100% for selections on  $H_T$  and  $\mathcal{H}_T$  as low as 200 and 130 GeV respectively.

The HLT triggers used for the signal region are summarised in Table 6.3 as well as the L1 triggers used to seed these paths. In order to reduce the rate sufficiently to allow PF reconstruction at the HLT, a prefilter is required on calorimeter quantities. An event in any category may pass any of the trigger paths; however, each is designed to maximise the efficiency for a particular set of categories.

For the monojet topology, the highest efficiency is achieved with the HLT  $\mathcal{H}_T$ - $E_T$  cross trigger using thresholds of 100 GeV on both quantities. For the symmetric and asymmetric categories, dedicated seeds are used that select events based on the  $\alpha_T$ ,  $H_T$  and the average  $p_T$  of the leading two jets ( $p_T^{(j_1, j_2)}$ ). A selection of  $p_T^{(j_1, j_2)} > 90$  GeV was found to optimise the efficiency across topologies given the rate requirements. The

resultant reduction in efficiency for asymmetric categories is recovered by the use of the  $H_T$ - $E_T$  cross trigger in addition to the dedicated cross triggers. Finally, for bins with  $H_T > 800$  GeV, where there is no  $\alpha_T$  threshold, an HLT seed with a threshold of only  $H_T > 800$  GeV provides efficiency.

**Table 6.3:** Trigger thresholds of the Level-1 and final PF-trigger decision for the HLT paths for the hadronic signal region. Except for those on  $\alpha_T$ , all thresholds are in GeV

L1 seed ( $H_T, E_T'$ )	HLT calo-prefilter ( $H_T, \alpha_T, p_T^{(j1,j2)}, E_T'$ )	HLT PF-filter ( $H_T, \alpha_T, p_T^{(j1,j2)}, E_T'$ )
240, 70	150, 0.540, 70, -	200, 0.570, 90, -
240, 70	200, 0.535, 70, -	250, 0.550, 90, -
240, 70	250, 0.525, 70, -	300, 0.530, 90, -
240, 70	300, 0.520, 70, -	350, 0.520, 90, -
240, 70	370, 0.510, 70, -	400, 0.510, 90, -
240, -	650, -, -, -	800, -, -, -
-, 70	-, -, -, 65	-, -, -, 90

The trigger efficiencies for the signal region are measured using the efficiency for data selected by independent muon and electron ‘reference triggers’ to pass signal region selection. The central value of the trigger efficiency is taken from the measurement using the electron reference trigger. The efficiency in  $H_T$  bins for different  $H_T$  ranges is shown in Figure 6.6. Given the selection of  $H_T > 200$  GeV, an efficiency of  $> 90\%$  is achieved across the signal region.

Biases may be introduced in the trigger efficiency measurement due to contamination in the computation of event variables from the reference object and different treatments between trigger and offline reconstructions. The difference between the measurement of the efficiencies using the muon and electron reference triggers is used to probe this bias and propagated as a systematic uncertainty.

### 6.6.2 Electroweak control regions

The control regions use a trigger requirement on the relevant object in that control region. The  $\mu +$  jets and  $\mu\mu +$  jets regions are selected using a threshold of 22 GeV on the muon  $p_T$  at the HLT. The efficiency is measured in data using the tag and probe method [95]. These efficiencies are applied as appropriate per muon  $p_T$  and  $\eta$ .

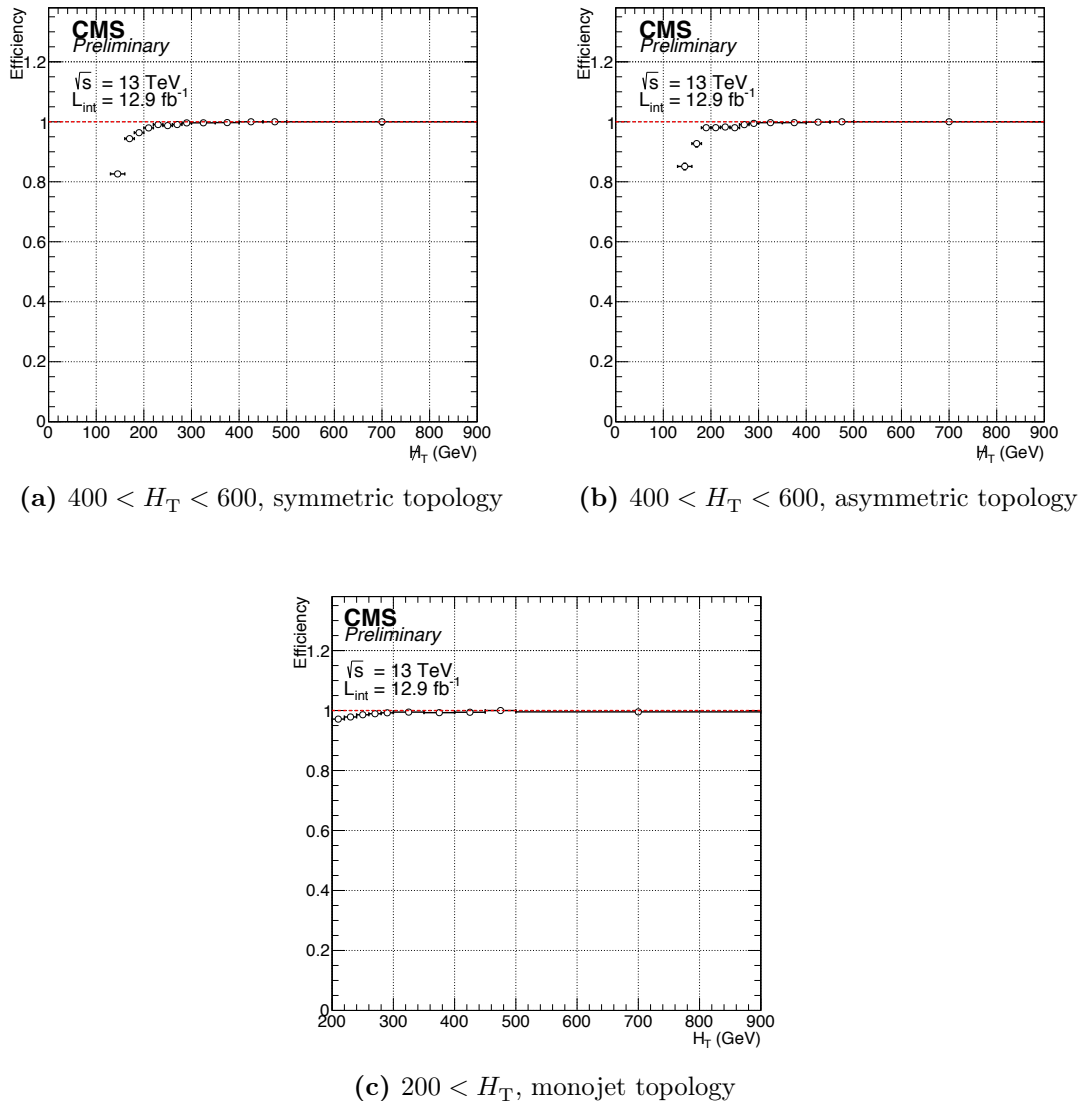


**Figure 6.6:** Signal trigger efficiency in the  $H_T$  dimension measured with a muon sample for a representative category for each topology.

The  $\gamma +$  jets control region is selected using events passing a threshold at the HLT of photon  $p_T > 175$  GeV or  $H_T > 800$  GeV. The efficiency is measured in data using events passing the HLT  $H_T > 800$  GeV requirement that satisfy the  $\gamma +$  jets control region requirements. These efficiencies are shown in Figure 6.7 and are applied per photon  $p_T$ .

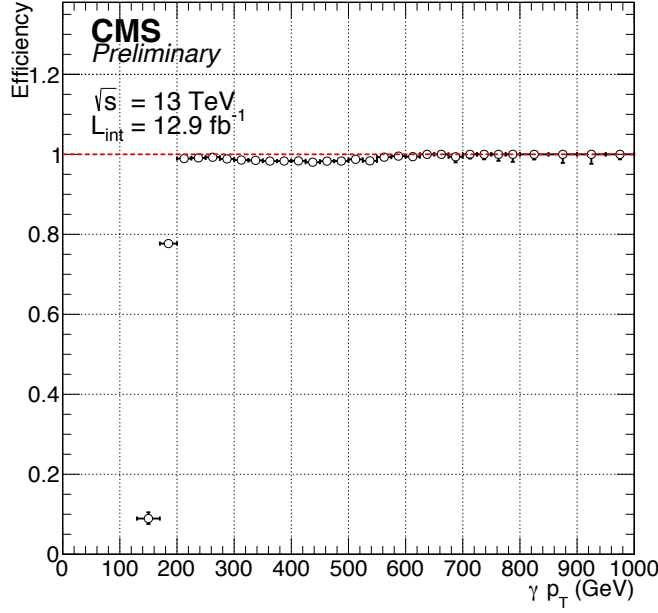


**Figure 6.7:** Trigger efficiency as a function of photon  $p_T$  for an inclusive selection.

## 6.7 Summary

The selections described in this section provide a powerful rejection of the dominant QCD multijet background as well as significantly reducing the electroweak backgrounds. The events falling into the signal region are finely categorised in order to provide inclusive sensitivity to a wide range of BSM models. To extract a possible signal contribution, the residual backgrounds must be robustly estimated, as described in Chapter 7.

# Chapter 7

## Background estimation for the $\alpha_T$ search

The accurate estimation of SM background yields is crucial for a sensitive and robust search for BSM physics. In this section, the data-driven estimations used by the  $\alpha_T$  analysis to predict the QCD multijet and electroweak background components are detailed.

Differences between control region and signal region selection may introduce bias into the background predictions due to discrepancies between simulation and data. The simulated events are therefore reweighted to account for such discrepancies. These corrections and corresponding systematic uncertainties, derived from variations in simulation, are described in Sections 7.2 and 7.4.1 respectively.

The predictions from the control regions are checked for residual bias using tests in data to probe the consistency of the control regions. These tests are discussed in Section 7.4.2 and are used to derive additional uncertainties to cover effects that may not be covered by the systematic uncertainties derived using variations in simulation.

The modelling of the  $H_T$  variable is taken directly from simulation in each  $n_{\text{jet}}$ ,  $n_b$  and  $H_T$  bin. The validation of this modelling and derivation of related systematic uncertainties using data in the control regions is described in Section 7.5. These uncertainties are included in addition to those derived from variations in simulation.

## 7.1 Datasets and simulated samples

The analysis detailed in this thesis uses datasets collected during the 25 ns run of the LHC at 13 TeV during 2016 as well as simulated samples to model the background and signal contributions.

### 7.1.1 Data

The events recorded by CMS are collected and categorised depending on the trigger selections detailed in Section 6.6. For the signal hadronic control regions, data passing the  $\alpha_T$ - $H_T$ ,  $H_T$ - $E_T$  and  $H_T$  triggers are collected into the HTMHT, MET and JetHT ‘primary datasets’ respectively. For the electroweak control regions, data passing the single photon and single muon triggers are collected into the SinglePhoton and SingleMuon primary datasets. These primary datasets are filtered to remove any overlaps. The total integrated luminosity of each dataset is measured as  $12.9 \pm 0.8 \text{fb}^{-1}$ .

### 7.1.2 Simulated samples

Simulated samples are necessary for background and signal prediction. The different ‘generators’ used to produce the processes are detailed below.

The processes with the highest contributions to the signal and control regions, including  $Z \rightarrow \nu\bar{\nu} + \text{jets}$ , Drell-Yan ( $q\bar{q} \rightarrow Z/\gamma^* \rightarrow l^+l^-$ ) + jets,  $\gamma + \text{jets}$ ,  $t\bar{t} + \text{jets}$ ,  $W + \text{jets}$  and QCD multijet events, are generated at leading order (LO) using MADGRAPH5 AMC@NLO [96]. The same generator is used at next-to-leading order (NLO) in the strong coupling constant ( $\alpha_s$ ) to generate samples of s-channel production of single top and  $t\bar{t}V$  events. The t-channel and tW-channel single top samples are generated using POWHEG [97]. The diboson samples, WW, WZ and ZZ, are generated using PYTHIA8 [49]. The full detector response is simulated using the GEANT4 [54] package for these samples.

The signal samples include both gluino-mediated and direct pair production of squarks in association with up to two additional partons. These are generated using MADGRAPH5 AMC@NLO with the sparticle decay performed using PYTHIA8 taking 100% branching fraction to the specified final state. The cross sections are calculated with NLO plus next-to-leading-logarithm (NLL) accuracy [98].

## 7.2 Corrections to simulation

The simulation is corrected to improve the modelling of kinematics and detector effects as they are observed in data. These corrections may be common to many analyses, such as reweighting to correct the pile-up modelling, or derived specifically for the  $\alpha_T$  analysis, such as the evaluation of cross section corrections in the  $\alpha_T$  phase space, and are detailed in this section.

### 7.2.1 Pileup reweighting

The distribution of the pile-up interactions in the simulated events is different from that in the data and is corrected using the ‘pile-up reweighting’ procedure.

The reweighting factors are derived as a function of the number of interactions in the bunch crossing. For data, this is derived by measuring the instantaneous luminosity for each colliding bunch and multiplying by the cross section of the total inelastic p-p interaction (63 mb).

The pile-up reweighting factors are the ratios of the distribution of the number of simulated interactions in data and simulation. These are normalised such that the total number of simulated events is unchanged. The uncertainty in this reweighting is derived by constructing alternative weighting factors for variations of the inelastic p-p cross section of  $\pm 5\%$ .

### 7.2.2 Top $p_T$ reweighting

The top  $p_T$  distribution is significantly different in simulation and data for  $t\bar{t}$  events. A reweighting is carried out based on the result of the CMS measurement of the differential cross section of top quark pair production at 13 TeV [99]. This weighting is carried out on only the  $t\bar{t}$  simulated sample and depends on the  $p_T$  of the top and antitop in the event.

### 7.2.3 Lepton and photon scale factors

Differences in the efficiency for leptons and photons predicted in simulation and measured in data are mitigated by the use of scale factors. Each scale factor corrects a different source of mismodelling, such as object identification, trigger efficiency, tracker efficiency and isolation requirements. These are derived from the ratio of the efficiency measured in data to that in simulation using methods such as tag-and-probe [95]; they are typically dependent on the  $\eta$ ,  $p_T$  and/or  $\phi$  of the relevant object.

### 7.2.4 B tag scale factor correction

The b tag scale factors are computed using the ratio of the efficiency in data for identifying a jet as originating from a bottom quark to the efficiency in simulation. These scale factors depend on simulated jet flavour,  $p_T$  and  $\eta$ .

The simulated samples are corrected by reweighting each event rather than changing the properties of jets within the event. The efficiency for tagging a jet,  $i$ ,  $\epsilon_i^b$ , is measured in simulation per jet  $p_T$ ,  $\eta$  and flavour separately for each of the  $\alpha_T$  signal and control regions. The probability of a particular configuration of b tagged jets in data and simulation is then calculated for each event,

$$P(\text{simulation}) = \prod_{i=\text{tagged}} \epsilon_i^b \prod_{j=\text{not tagged}} (1 - \epsilon_j^b) \quad (7.1)$$

$$P(\text{data}) = \prod_{i=\text{tagged}} SF_i \epsilon_i^b \prod_{j=\text{not tagged}} (1 - SF_j \epsilon_j^b) \quad (7.2)$$

where  $SF_i$  is the scale factor. Using these probabilities the b tag scale factor weighting for the event is determined by

$$w = \frac{P(\text{data})}{P(\text{simulation})}. \quad (7.3)$$

### 7.2.5 Trigger efficiency

The simulated samples are corrected to account for inefficiencies in the selection of muons by the trigger. The muon trigger selection is emulated in the simulation with a scale factor applied as described in Section 7.2.3. The photon trigger efficiencies are not emulated in the simulation and therefore photon  $p_T$  dependent corrections are measured using data.

The efficiencies for the signal triggers are measured using data, as described in Section 6.6, and are  $H_T$ ,  $n_{\text{jet}}$  and  $\mathcal{H}_T$  dependent.

### 7.2.6 Sideband corrections

Given the high- $H_T$ , high- $E_T$  selection used in this search, the normalisations of the simulated samples may not agree with data. This can be due to the kinematic selection as well as missing higher perturbative order corrections to the overall cross section.

The transfer factor method used for background prediction (see Section 7.3.1) is designed to minimise sensitivity to the normalisation of background processes due to the similar composition of the control and signal regions. However, this may not apply to the tests in data described in Section 7.4.2.

In this section, a procedure is described to derive process-dependent corrections ('sideband corrections'). These corrections are determined using a maximum likelihood fit to data in sidebands to the control regions and are derived after all other re-weightings are applied. The sideband corrections are applied and propagated to all the steps of the analysis. No uncertainty is considered for these corrections as this will be covered by the systematics derived through the tests described in Section 7.4.2.

To take advantage of the full phase space of the sidebands, a simultaneous fit is used to derive the corrections for  $\gamma + \text{jets}$ ,  $W + \text{jets}$ ,  $Z + \text{jets}$  and  $t\bar{t}$ , using the  $100 < \mathcal{H}_T < 130$  GeV sideband for the  $\mu + \text{jets}$  and  $\mu\mu + \text{jets}$  control region and an  $\alpha_T$  sideband (inverting the  $\alpha_T$  selection per  $H_T$  bin) for the  $\gamma + \text{jets}$  control region.

The sideband is binned identically to the control region in  $n_{\text{jet}}$ ,  $n_b$  and  $H_T$  and a floating parameter per relevant process encodes the correction for that process (fully correlated across all bins). The normalisations of the  $W + \text{jets}$  and  $t\bar{t}$  processes are mainly constrained by the  $\mu + \text{jets}$  sideband while the normalisations of the  $Z + \text{jets}$  and  $\gamma$

$+ \text{jets}$  processes are constrained by the  $\mu\mu + \text{jets}$  and  $\gamma + \text{jets}$  sidebands respectively. The values of the corrections and their statistical uncertainties given by the fit are shown in Table 7.1. The correction derived for  $Z + \text{jets}$  is must also be applied to the  $Z \rightarrow \nu\bar{\nu}$  sample.

**Table 7.1:** Sideband corrections for SM backgrounds derived with fit to sidebands in data.

Process	Sideband	Selection	Correction
$W + \text{jets}$	$100 < H_T < 130 \text{ GeV}$	$\mu + \text{jets}$	$1.13 \pm 0.01$
$Z + \text{jets}$	$100 < H_T < 130 \text{ GeV}$	$\mu\mu + \text{jets}$	$1.08 \pm 0.01$
$\gamma + \text{jets}$	$0.50 < \alpha_T < 0.52(0.53)$	$\gamma + \text{jets}$	$1.33 \pm 0.03$
$t\bar{t} + \text{jets}$	$100 < H_T < 130 \text{ GeV}$	$\mu + \text{jets}, \mu\mu + \text{jets}$	$0.91 \pm 0.01$

## 7.3 Background estimation

### 7.3.1 Electroweak background prediction

The electroweak backgrounds are predicted using the transfer factor method. The control regions are binned identically to the signal region in  $H_T$ ,  $n_{\text{jet}}$  and  $n_b$ . The data and simulation counts in the control region,  $N_{\text{obs}}^{\text{control}}(n_{\text{jet}}, n_b, H_T)$  and  $N_{\text{sim}}^{\text{control}}(n_{\text{jet}}, n_b, H_T)$ , respectively, as well as the simulation counts in the signal region,  $N_{\text{sim}}^{\text{signal}}(n_{\text{jet}}, n_b, H_T)$  are used to predict the background in the signal region,  $N_{\text{pred}}^{\text{signal}}(n_{\text{jet}}, n_b, H_T)$ . The TF is defined using the ratio of the number of events predicted in simulation in the signal region and control region for the relevant processes,

$$\text{TF}(n_{\text{jet}}, n_b, H_T) = \frac{N_{\text{sim}}^{\text{signal}}(n_{\text{jet}}, n_b, H_T)}{N_{\text{sim}}^{\text{control}}(n_{\text{jet}}, n_b, H_T)}. \quad (7.4)$$

The prediction of the relevant process in the signal region can then be written as

$$N_{\text{pred}}^{\text{signal}}(n_{\text{jet}}, n_b, H_T) = \text{TF}(n_{\text{jet}}, n_b, H_T) \times N_{\text{obs}}^{\text{control}}(n_{\text{jet}}, n_b, H_T). \quad (7.5)$$

The  $\mu + \text{jets}$  control region is used to predict the  $W + \text{jets}$  plus  $t\bar{t}$  backgrounds ( $t\bar{t}/W$ ) while the  $Z + \text{jets}$  background is predicted using the  $\mu + \text{jets}$ ,  $\mu\mu + \text{jets}$  and  $\gamma + \text{jets}$  control regions. The encoding of these predictions within the likelihood used for the  $\alpha_T$  analysis is described in Section 8.1.

The transfer factors account for differences in the cross sections and branching fractions, acceptance and reconstruction efficiencies and kinematic requirements between signal and control regions. The values of the transfer factors for the prediction from the  $\mu + \text{jets}$ ,  $\mu\mu + \text{jets}$  and  $\gamma + \text{jets}$  control regions are shown in Figures A.1-A.2.

The transfer factors are robust against many sources of systematic effects in the modelling of  $H_T$ ,  $n_b$  and  $n_{\text{jet}}$  as they cancel in the ratio of simulation in control and signal region. Residual uncertainties remain due to sources such as theoretical uncertainties (for example in predicting  $Z \rightarrow \nu\bar{\nu}$  using  $\gamma + \text{jets}$  events) and mismodelling of the reconstruction of the objects used in the control region. The determination of these uncertainties using both simulation and tests in data is discussed in detail in Section 7.4.

An example of the robustness of the transfer factor method can be seen in Figure 7.1 in which the relative change in the simulated  $t\bar{t}/W$  background in the signal region is compared to the change in the transfer factor for the  $\mu$  to  $t\bar{t}/W$  prediction under a variation of the uncertainty related to the top  $p_T$  reweighting to  $+1\sigma$ . While the simulation varies by up to 30%, the transfer factor variations are under 10%.

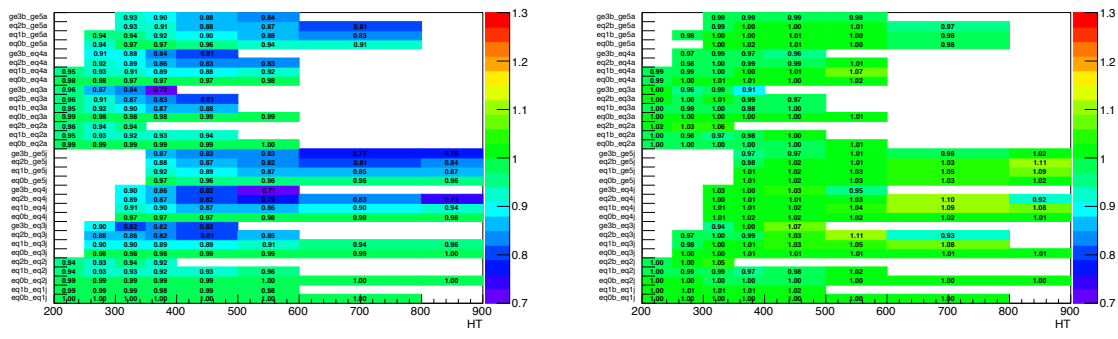


**Figure 7.1:** The relative change in the  $t\bar{t}/W$  simulation compared to the relative change in the  $\mu + \text{jets} \rightarrow (t\bar{t}/W)$  transfer factor when varying the top  $p_T$  uncertainty to  $+1\sigma$ .

### 7.3.2 QCD background prediction

The prediction of the QCD multijet background is particularly challenging as it is non-perturbative and has a very large cross section leading to many final state topologies that can pass selection. A transfer factor method is used, similar to that used for the electroweak backgrounds. The region used for the prediction is the QCD multijet enriched hadronic control region, selected by inverting the signal region selection on  $H_T/\cancel{E}_T$ . Due to the limited statistical power of this sample, predictions are made per  $n_{\text{jet}}$  and  $H_T$  category (inclusive in  $n_b$ ). Figure 7.2 shows the QCD multijet events from simulation in the hadronic control region and signal region and corresponding transfer factors between the regions.

The hadronic control region contains a significant electroweak background component, as shown in Figure 7.2d. This component must be accurately predicted using electroweak enriched control regions (with the  $H_T/\cancel{E}_T$  selection inverted) analogously to the signal region. The remaining QCD multijet contribution in the control region,  $N_{QCD}^{\text{control}}$ , then replaces  $N_{\text{obs}}^{\text{control}}$  in Equation 7.5 to predict the QCD multijet contribution in the signal region.

To determine the electroweak predictions in the hadronic control region transfer factors from the  $H_T/\cancel{E}_T$  electroweak control regions are constructed and a simultaneous fit is carried out, similar to that described in Section 8.1 for the signal region. This fit includes all systematic variations discussed in Section 7.4, derived with the  $H_T/\cancel{E}_T$  selection inverted. An unconstrained contribution in the fit, uncorrelated in each  $n_{\text{jet}}$  and  $H_T$  category, is included to measure the difference between the electroweak prediction and the observation. This is taken as  $N_{QCD}^{\text{control}}$  in each bin and the values per  $n_{\text{jet}}$  and  $H_T$  category, including systematic and statistical uncertainty, are shown in Figure 7.3a.

The signal region prediction is then made by multiplying the QCD multijet component in the hadronic control region by the transfer factors shown in Figure 7.2c. The results of this prediction are shown in Figure 7.3b, with the ratio between the multijet and non-multijet background predictions shown in Figure 7.3c. The multijet component is typically  $\leq 5\%$ .

The distribution of the QCD multijet contribution in  $n_b$  and  $H_T$  in each  $H_T$  and  $n_{\text{jet}}$  category is predicted using the distribution of the electroweak background with the normalisation derived as described above. This approximation is necessary due to the very low QCD multijet event yields for high  $n_b$  and  $H_T$ . As the multijet background is

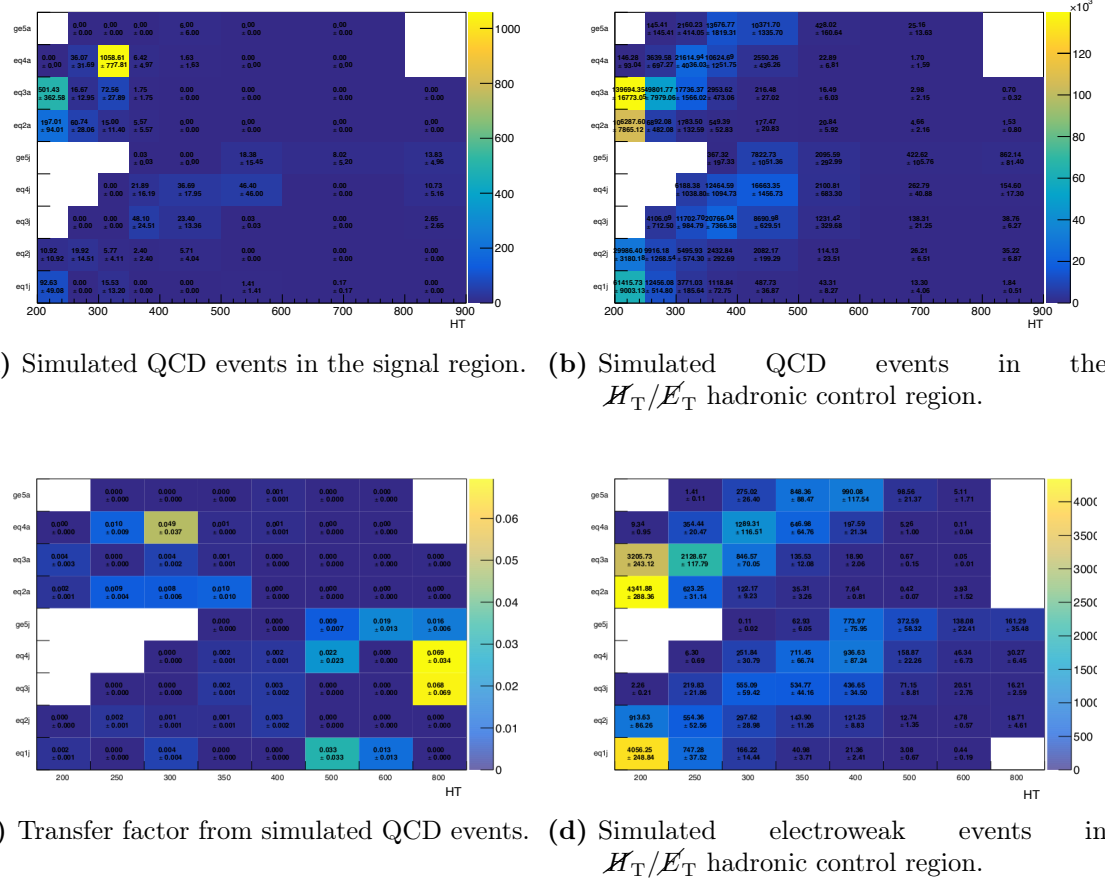
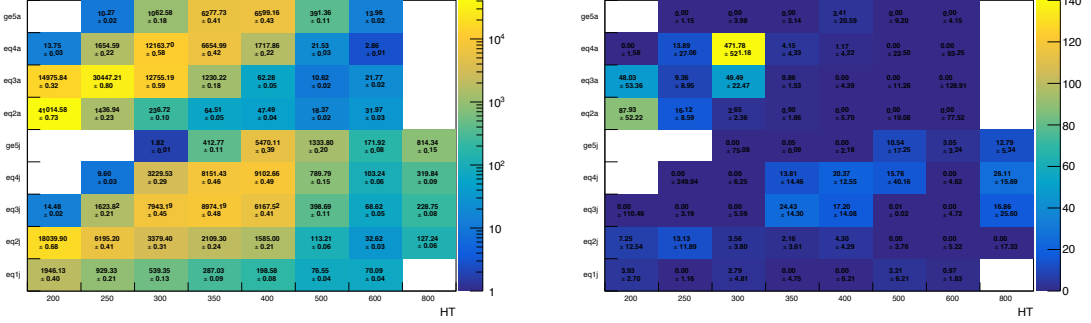


**Figure 7.2:** Expected number of QCD multijet events determined from simulation, binned according to  $n_{jet}$  and  $H_T$ , that (a) satisfy and (b) fail the requirement  $\mathcal{H}_T/\mathcal{E}_T < 1.25$ . Also shown in (c) is the transfer factor for QCD multijets from hadronic control to signal region, again determined from simulation. Finally, (d) shows the expected number of electroweak background events ( $V+jets$  and  $t\bar{t}$ , plus other residual non-multijet backgrounds) that fail the  $\mathcal{H}_T/\mathcal{E}_T < 1.25$  requirement, again determined from simulation and binned according to  $n_{jet}$  and  $H_T$ .

typically  $\leq 1\%$ , deviations from the electroweak shape in these variables have a small effect on the background prediction.

The multijet contribution in the electroweak control regions is small, typically  $\leq 1\%$ , and is therefore taken from simulation.



**(a) Predicted QCD counts in the  $H_T/\cancel{E}_T$  hadronic control region.** **(b) QCD multijet predictions in the signal region.**

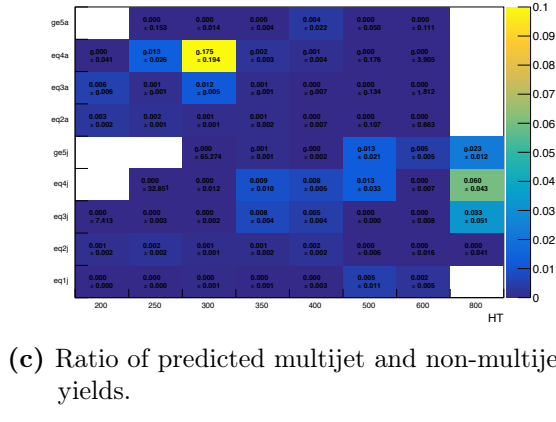
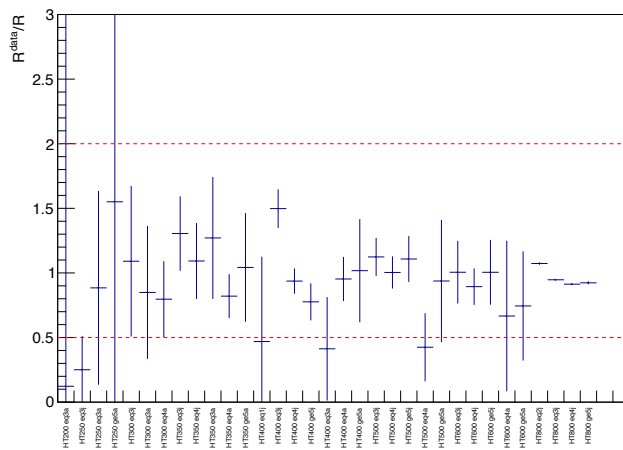


**Figure 7.3:** The QCD yields taken from the simultaneous fit binned according to  $n_{jet}$  and  $H_T$  are shown in (a). Shown in (b) is the result of multiplying the observed multijet events predicted in (a) by the translation factor from the sideband to the signal region determined with simulation (shown in Figure 7.2). This gives a data-driven expectation of the quantity of multijet background events in the signal region. Finally, (c), shows the ratio of expected multijet background events in the signal region divided by non-multijet backgrounds. The multijet background is therefore shown to be at the percent level.

### Validation of the multijet prediction

The QCD multijet prediction relies on an extrapolation in the  $H_T/\cancel{E}_T$  requirement. Significant mismodelling of this variable can bias the QCD prediction and therefore a validation of this extrapolation is carried out using an additional hadronic control region which is defined by inverting the  $\Delta\phi_{min}^* > 0.5$  requirement. The ratio of events passing and failing the requirement  $H_T/\cancel{E}_T < 1.25$  is made in data and simulation,  $\mathcal{R}^{data}$  and  $\mathcal{R}$  respectively, in categories of  $n_{jet}$  and  $H_T$ . The ratio of  $\mathcal{R}^{data}$  to  $\mathcal{R}$  is shown in

Figure 7.4 (excluding bins with insufficient statistics). Given the level of agreement, a fully correlated systematic uncertainty of 100% is included on the QCD contamination. This is included in addition to the systematic uncertainties shown in Figure 7.3c, taken as uncorrelated in each category.



for  $\pm 1 \sigma$  variations, is described in Section 8.1. In this section the systematic variations of the transfer factor for each effect is discussed. The effect of these systematics on the  $H_T$  shape is discussed in Section 7.5.

### Pileup reweighting

The uncertainty on the inelastic p-p cross section of  $\pm 5\%$  is propagated by deriving the pile-up weights for the cross section at the  $\pm 1\%$  sigma values. These weights are used to derive alternative predictions for each variation. Typically the uncertainty introduced by pile-up reweighting is small, up to  $\sim 2\%$  depending on the category.

### Jet energy scale

The energies of jets used in the analysis are corrected as a function of their  $p_T$  and  $\eta$  via the procedure described in Section 4.3.2. The uncertainty on this correction is propagated through the analysis. As the  $H_T$  and jet multiplicity binning is mirrored in signal and control regions, the variation in the transfer factors is small. To avoid statistical fluctuations, the variation is averaged across  $n_b$ . The systematic variations are typically in the range of 1 to 5% depending on the category.

### B-tagging efficiency

Scale factors are applied to simulation to correct for differences in the b tagging efficiencies and misidentifications between simulation and data. Since no extrapolation is performed in the background prediction across different  $n_b$  multiplicities, the analysis is expected to be robust against variations in the b tagging efficiency. The scale factors associated with b and c jets are varied together (since their measurements are correlated), while those associated with light jets are varied separately. The systematic variations are typically in the range of 1 to 3% depending on the category.

### Lepton trigger/identification/isolation efficiency

Leptons out of  $p_T$  and  $\eta$  acceptance, or within detector acceptance but not identified properly by lepton identification or isolation requirements contribute to the lost lepton background. The variation in the lost lepton background is measured using a simulated

sample with no lepton veto. Using this sample, the variation in probability for reconstructing a lepton in the signal region, and the variation for reconstructing a muon for the  $\mu + \text{jets}$  control region is determined with appropriate correlation. The systematic uncertainties from trigger, identification and isolation efficiencies on the muon and electron scale factors are varied separately. An additional uncertainty is considered on the  $\mu + \text{jets}$  control region for the muon tracking scale factor. The systematic variations are typically in the range of 1 to 3% depending on the category.

### Photon trigger uncertainty

The photon trigger correction is derived for the  $\gamma + \text{jets}$  control region. The systematic uncertainty is taken as the size of the measured inefficiency. The systematic variation in the  $\gamma + \text{jets}$  transfer factors is typically under  $\sim 3\%$ .

### Signal trigger uncertainty

The systematic on the signal trigger efficiency is taken as the difference in the efficiency measured using muon and electron reference triggers. This uncertainty affects only the signal region predictions and not the control region predictions. The systematic variation in the transfer factors is typically in the range 1 to 6%.

### Top $p_T$ reweighting

The uncertainty in the top  $p_T$  reweighting is taken as the size of the reweighting applied to each event. The systematic variation in the transfer factors is typically in the range 1 to 7%.

#### 7.4.2 Closure test method

The variations described above cover systematic uncertainties that can be easily assessed from simulation. In addition, the data in the control samples are used to further probe sources of bias in the transfer factors due to limitations in the simulation. The events of one control sample, B, are predicted using events from another control sample, A, using a transfer factor from the ratio in simulation,

$$N_{\text{pred}}^B = N_{\text{sim}}^B / N_{\text{sim}}^A \times N_{\text{data}}^A = TF_{AB} \times N_{\text{data}}^A. \quad (7.6)$$

The agreement between the observation in sample B and the prediction from sample A is measured by the ratio

$$R_{AB} = \frac{N_{\text{data}}^A - N_{\text{pred}}^B}{N_{\text{pred}}^B}. \quad (7.7)$$

The closure between the samples is defined as the significance of the deviation of this ratio from zero considering statistical uncertainties in both observation and simulation in samples A and B. The tests are performed separately per  $n_{\text{jet}}$  and  $H_T$  category to investigate the level of closure. The uncertainties are derived per  $H_T$  bin by merging the  $n_{\text{jet}}$  categories into the symmetric and asymmetric (including monojet) topologies. For each such category, the systematic uncertainty is defined by the value of  $R_{AB}$  added in quadrature to its statistical uncertainty. For tests involving the  $\mu\mu + \text{jets}$  sample, which has lower statistical power, pairs of  $H_T$  bins are merged for the closure tests.

The systematics derived using these tests are applied to the transfer factors. They are considered as uncorrelated per  $H_T$  and jet topology (monojet and asymmetric topologies are correlated) and correlated in other categorisations. The tests carried out and systematic biases probed are discussed below.

### Extrapolation in $\alpha_T$ and $\Delta\phi_{\min}^*$

The extrapolation in  $\alpha_T$  and  $\Delta\phi_{\min}^*$  from the  $\mu + \text{jets}$  and  $\mu\mu + \text{jets}$  control regions and in  $\Delta\phi_{\min}^*$  for the  $\gamma + \text{jets}$  control region to the signal region may introduce bias due to modelling differences in data and simulation. To test the  $\alpha_T$  ( $\Delta\phi_{\min}^*$ ) modelling the  $\mu + \text{jets}$  sample is divided into events with an  $\alpha_T$  ( $\Delta\phi_{\min}^*$ ) requirement and with this requirement inverted. The  $\alpha_T$  requirement is decided by the signal  $H_T$  bin and the  $\Delta\phi_{\min}^*$  requirement is 0.5. The systematic is derived from the  $\alpha_T$  closure tests for bins with  $H_T < 800\text{GeV}$  and from the  $\Delta\phi_{\min}^*$  tests for  $H_T > 800\text{GeV}$ .

The results of these tests are shown in Figure 7.5 as a function of  $H_T$  and  $n_{jet}$ . The grey band is the systematic uncertainty propagated through the analysis. The systematic derived from these tests is in the range 4 to 32%.

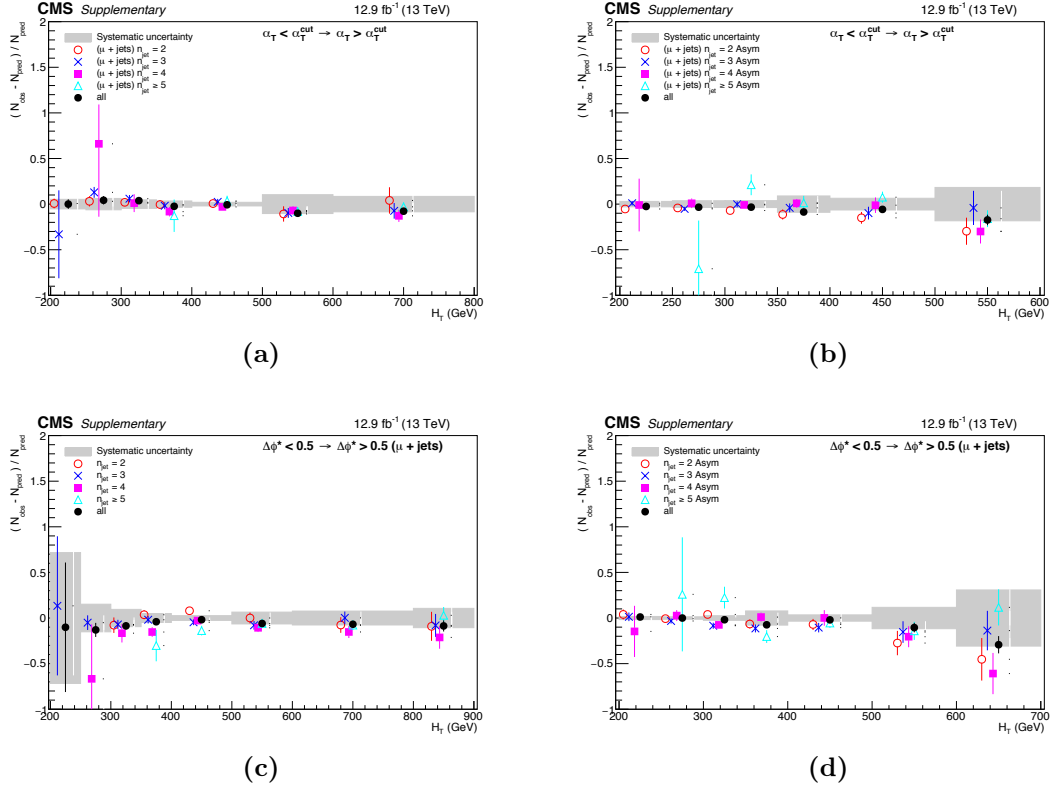


**Figure 7.5:** Tests in data probing the  $\alpha_T$  (top row) and  $\Delta\phi^*$  (bottom row) extrapolation for each  $n_{jet}$  category (open symbols) overlaid on top of the systematic uncertainty estimates used for each of the seven  $H_T$  bins (shaded bands). The symmetric (asymmetric) jet topologies are shown in the left (right) plot.

### Modelling of the W acceptance due to polarisation effects

The high  $p_T$  W bosons produced in p-p collisions are predominantly left-handed [100]. There is no right-handed neutrino and therefore the  $W^+$  bosons preferentially decay to the (left-handed) neutrino along its direction of motion while the lepton points backwards. The  $W^-$  bosons behave oppositely, decaying to the lepton along its direction of motion.

W + jets events typically pass signal region selection due to the presence of a boosted neutrino while such events typically pass  $\mu + \text{jets}$  control region selection due to the presence of a boosted lepton. There is therefore a preponderance of  $W^+$  over  $W^-$  in the

signal region compared to the  $\mu +$  jets control region. This may introduce bias in the prediction and a data-driven test is carried out by splitting the  $\mu +$  jets sample into events with either a  $\mu^+$  or  $\mu^-$ .

The results are shown in Figure 7.6 as a function of  $H_T$  and  $n_{\text{jet}}$ . The grey band is the systematic uncertainty propagated through the analysis. The systematic derived from these tests is in the range 3 to 12%.

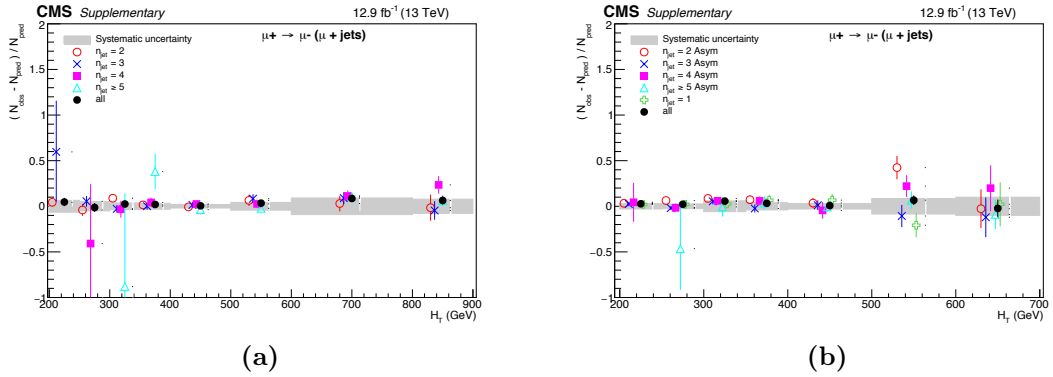


**Figure 7.6:** Data-driven tests probing the W polarisation effects. These are shown for each  $n_{\text{jet}}$  category (open symbols) overlaid on top of the systematic uncertainty estimates used for each of the seven  $H_T$  bins (shaded bands). The symmetric (asymmetric) jet topologies are shown in the left (right) plot.

## Modelling of the W/Z ratio

The  $\alpha_T$  analysis uses  $\mu +$  jets events to predict the Z+jets background. The extrapolation between W+jets and Z+jets events is tested by using the  $\mu +$  jets control region to predict the  $\mu\mu +$  jets control region. These tests probe differences in the modelling of the Z and W bosons, potential acceptance and reconstruction effects (expected to be subdominant) and the effect of the  $t\bar{t}$  contribution to  $\mu +$  jets.

The results are shown in Figure 7.7 as a function of  $H_T$  and  $n_{\text{jet}}$ . The grey band is the systematic uncertainty propagated through the analysis. The systematic derived from these tests is in the range 3 to 20%.

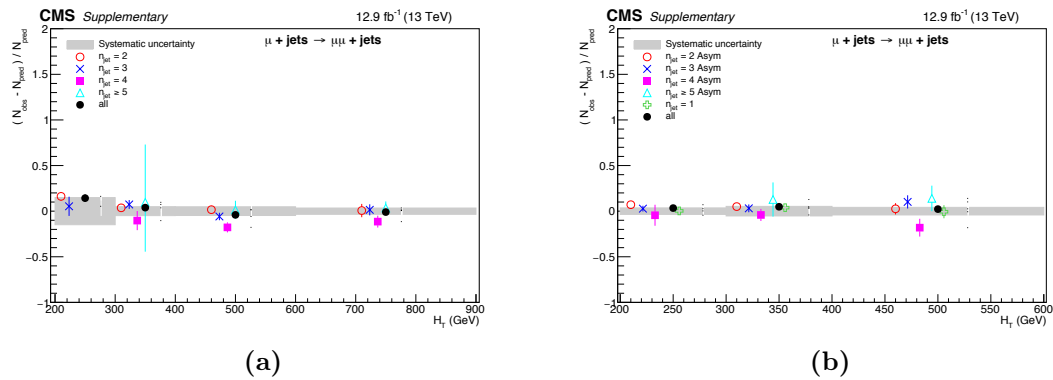


**Figure 7.7:** Data-driven tests probing the use of the  $\mu + \text{jets}$  control sample to predict the  $Z + \text{jets}$  background for each  $n_{\text{jet}}$  category (open symbols) overlaid on top of the systematic uncertainty estimates used for each of the seven  $H_T$  bins (shaded bands). The symmetric (asymmetric) jet topologies are shown in the left (right) plot.

## Modelling of the Z/ $\gamma$ ratio

The  $\alpha_T$  analysis uses  $\gamma + \text{jets}$  events to predict the  $Z + \text{jets}$  background. The extrapolation between  $\gamma$  and  $Z$  is tested by using the  $\gamma + \text{jets}$  control region to predict the  $\mu\mu + \text{jets}$  control region. These tests probe differences in the modelling of the  $Z$  and  $\gamma$  as well as potential acceptance and reconstruction effects for  $\mu$  and  $\gamma$  and the effect of contamination of non-prompt photons.

The results are shown in Figure 7.8 as a function of  $H_T$  and  $n_{\text{jet}}$ . The grey band is the systematic uncertainty propagated through the analysis. The systematic derived from these tests is in the range 7 to 15%.

## Modelling of the W/ $t\bar{t}$ admixture

The  $\mu +$  jets control region is used to predict the  $W +$  jets and  $t\bar{t}$  processes. However, the admixture between these processes may not be identical in the signal and control region. To probe potential bias introduced due to this admixture change, the sample is split into events with 0 and 1 b tag. These tests will also probe uncertainties related to the b tagging efficiency and related scale factors.

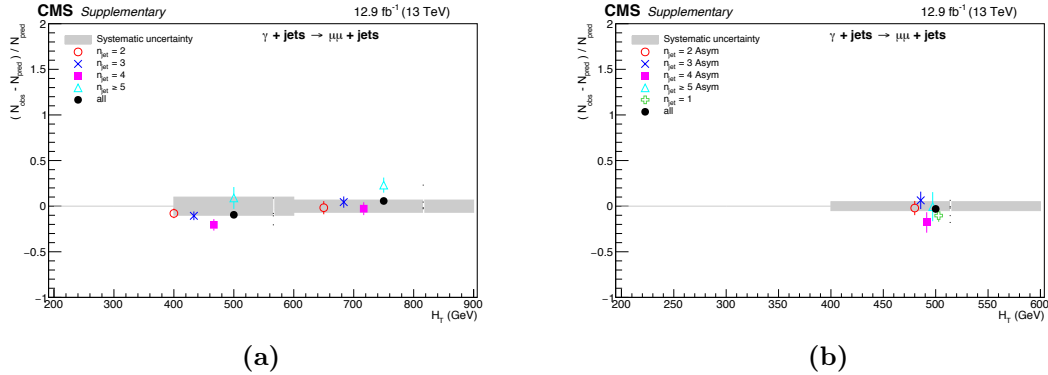


**Figure 7.8:** Data-driven tests probing the  $Z/\gamma$  ratio for each  $n_{\text{jet}}$  category (open symbols) overlaid on top of the systematic uncertainty estimates used for each of the seven  $H_T$  bins (shaded bands). The symmetric (asymmetric) jet topologies are shown in the left (right) plot.

The results are shown in Figure 7.9 as a function of  $H_T$  and  $n_{\text{jet}}$ . The grey band is the systematic uncertainty propagated through the analysis. The systematic derived from these tests is in the range 4 to 25%.

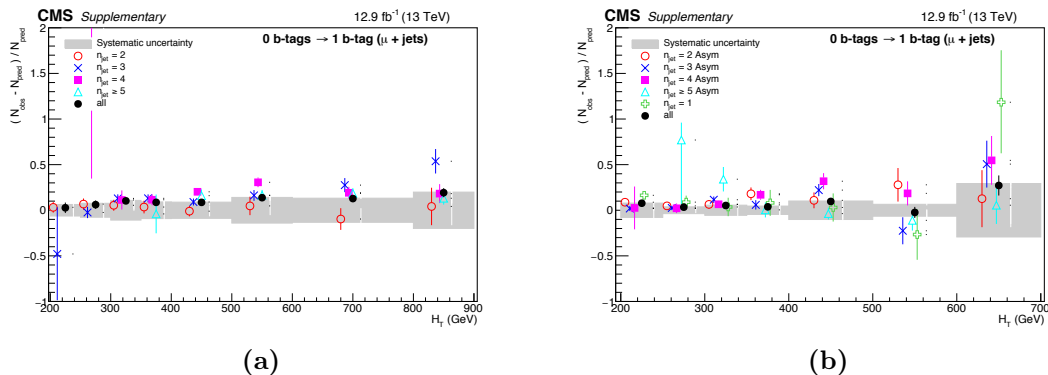


**Figure 7.9:** Data-driven tests probing the W and  $t\bar{t}$  admixture in each  $n_{\text{jet}}$  category (open symbols) overlaid on top of the systematic uncertainty estimates used for each of the seven  $H_T$  bins (shaded bands). The symmetric (asymmetric) jet topologies are shown in the left (right) plot.

### 7.4.3 Summary

The systematic uncertainties derived from the tests using the data control regions and from the variations in simulation are summarised in Table 7.2. Also shown are the

correlation scheme and approximate range in variation in the transfer factor for each systematic uncertainty.

**Table 7.2:** Summary of the systematics on the transfer factors considered in the analysis, with representatives ranges of uncertainties and the correlation assumed, for the predictions of the  $t\bar{t} + \text{jets}$ ,  $W + \text{jets}$  and  $Z \rightarrow \nu\bar{\nu}$  background components.

Systematic	Method	Relative uncertainty on transfer factor						Correlation model
		$\mu + \text{jets} \rightarrow Z \rightarrow \nu\bar{\nu}$	$\mu\mu + \text{jets} \rightarrow Z \rightarrow \nu\bar{\nu}$	$\gamma + \text{jets} \rightarrow Z \rightarrow \nu\bar{\nu}$	$\gamma + \text{jets} \rightarrow Z \rightarrow \nu\bar{\nu}$	$\mu + \text{jets} \rightarrow t\bar{t} + W$	$\mu + \text{jets} \rightarrow t\bar{t} + W$	
$\alpha_T/\Delta\phi_{\text{min}}^*$ extrapolation	tests in data	3 – 30%	3 – 30%	–	–	–	3 – 30%	uncorrelated across $H_T/\text{jet top.}$
W/Z ratio	tests in data	4 – 15%	–	–	–	–	–	uncorrelated across $H_T/\text{jet top.}$
$Z/\gamma$ ratio	tests in data	–	–	–	–	–	–	uncorrelated across $H_T/\text{jet top.}$
$W/t\bar{t}$ admixture	tests in data	–	–	–	–	–	–	uncorrelated across $H_T/\text{jet top.}$
W polarisation	tests in data	2 – 10%	–	–	–	–	2 – 10%	uncorrelated across $H_T/\text{jet top.}$
jet energy scale	simulation variations	1 – 5%	1 – 5%	1 – 5%	1 – 5%	1 – 5%	1 – 5%	fully correlated
b tagging efficiency b and c jets	simulation variations	1 – 3%	1 – 3%	1 – 3%	1 – 3%	1 – 3%	1 – 3%	fully correlated
b tagging efficiency light jets	simulation variations	1 – 3%	1 – 3%	1 – 3%	1 – 3%	1 – 3%	1 – 3%	fully correlated
pileup weights	simulation variations	0 – 2%	0 – 2%	0 – 2%	0 – 2%	0 – 2%	0 – 2%	fully correlated
top $p_T$ weights	simulation variations	1 – 30%	1 – 10%	–	–	1 – 10%	1 – 10%	fully correlated
lepton scale factor	simulation variations	1 – 3%	1 – 3%	–	–	1 – 3%	1 – 3%	fully correlated
signal trigger efficiency	simulation variations	1 – 2%	1 – 2%	1 – 2%	1 – 2%	1 – 2%	1 – 2%	fully correlated
photon trigger efficiency	simulation variations	–	–	–	–	–	–	fully correlated

## 7.5 Systematics on the $H_T$ modelling

The estimate of the number of events per ( $n_{\text{jet}}$ ,  $n_b$ ,  $H_T$ ) bin, integrated over  $H_T$ , is derived from data control samples, with the associated systematic uncertainty determined as described in Section 7.4.2. This section describes the method used to assess the systematic uncertainties in the distribution of events according to  $H_T$ . A data-driven approach is utilised to validate the  $H_T$  modelling using the data in the control regions. The level of closure in the control regions is used to derive alternative templates accounting for systematic uncertainties.

When looking at the  $H_T$  shape inclusively in  $H_T$  there are large theoretical uncertainties that originate from mixing events at different scales. These uncertainties can be mitigated if the events are binned according to a variable, such as  $H_T$ , which is strongly correlated with the scale of the event. After this categorisation is applied, the uncertainty in the distribution of the  $H_T$  variable is expected to be dominated by the modelling of the particle decays and, to a lesser extent, by jet reconstruction effects, such as jet energy scale and resolution. In Section 7.5.1, the mitigation of bias in the  $H_T$  distribution through binning in variables associated to the scale is tested using the control regions. In Section 7.5.2, the procedure used to extract associated systematic uncertainties in the  $H_T$  shape from the control regions is described and the results summarised.

The systematic uncertainties derived from the control regions are included in addition to systematics from variations in simulation. The variation in simulation follows the same procedure as described in Section 7.4.1; a comparison of the different sources of systematic uncertainty is presented in Section 7.5.3.

### 7.5.1 Validation using control regions in data

For each of the three electroweak control regions, the distribution of the ratio between data and simulation in  $H_T$  is fitted to a first order (linear) orthogonal polynomial (OP) to probe potential bias. The  $n^{\text{th}}$  order OP is

$$f_n(x) = \sum_{k=0}^{k=n} (p_k) \times (\bar{x} - x)^k, \quad (7.8)$$

where  $\bar{x}$  is the weighted mean of the distribution [101]. The odd and even  $p_k$  parameters are decorrelated and therefore, for the linear OP, the normalisation changing term ( $p_0$ ) is decorrelated from the shape changing term ( $p_1$ ). The consistency of the  $p_1$  parameter with zero can therefore be used to measure bias in the modelling of  $H_T$ .

In Figure 7.10 the data/simulation distributions against  $H_T$  are shown for the electroweak control region selections inclusive in  $H_T$  and jet categories. In each case, fitting a linear OP shows a large bias in the  $p_1$  parameter. This bias in the data/simulation agreement is expected as events at different scales are mixed.

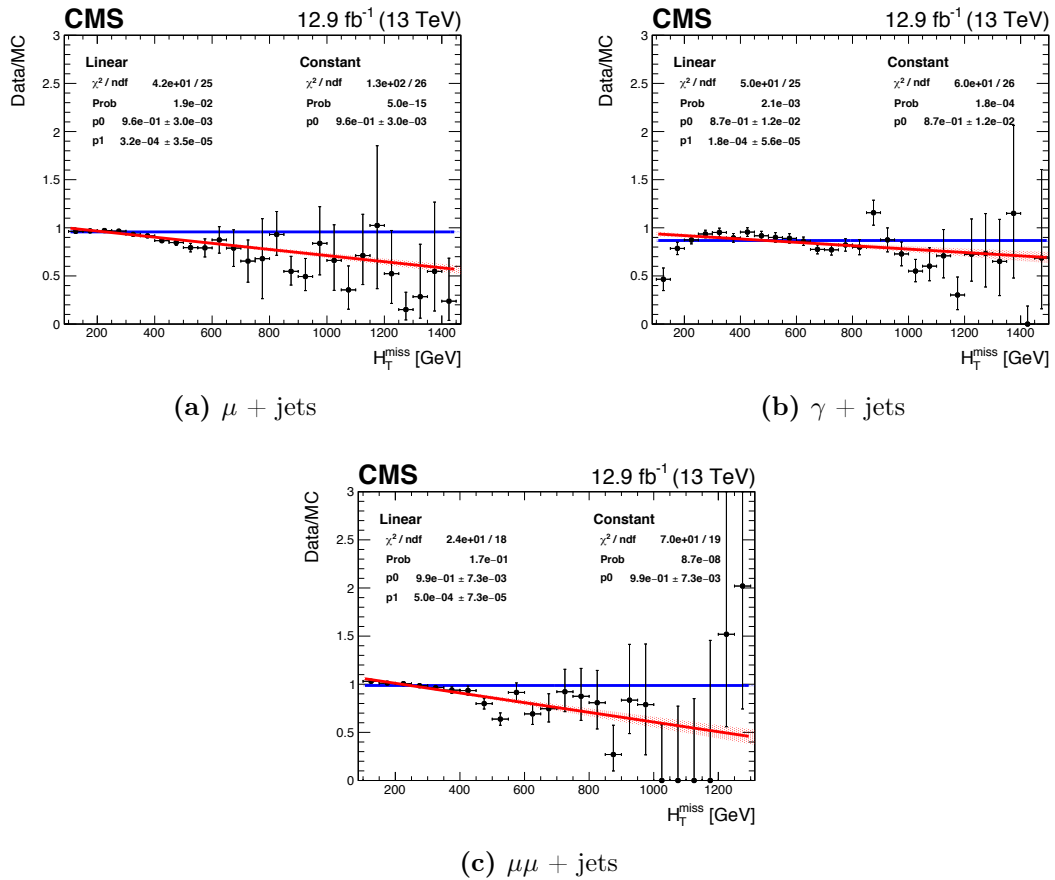


**Figure 7.10:** The data/simulation distribution against  $H_T$  for an inclusive selection on category and  $H_T$  showing the results of a linear fit. A large bias is observed as well as a low p-value for the constant fits.

By binning in  $H_T$ ,  $n_{\text{jet}}$  and  $n_b$ , the bias in the agreement between data and simulation due to mixing events at different scales is mitigated. In Figure 7.11, example fits of an linear OP to the data/simulation ratio are shown for the three control regions. Compared to the inclusive distribution the linear component can be seen to be compatible with

zero. In order to formalise this assertion, the pull of the linear component from zero is calculated. This pull distribution is shown for each of the three control regions in Figure 7.12 and can be seen in each case to have a mean and sigma fairly consistent with zero and one respectively, corresponding to the zero bias hypothesis. In Figure 7.13, the distribution of the pulls in jet category and  $H_T$  bins shows no significant trend across the phase space. Finally, the linear fits to the data/simulation ratio additionally have a p-value following a uniform distribution between 0 and 1 as shown in Figure 7.14.

### 7.5.2 Deriving systematics on the $H_T$ shape

The systematic uncertainty in the  $H_T$  shape is extracted from the statistical precision to which the zero bias hypothesis can be confirmed using the control regions, as described in the following.

Each background in the signal region ( $t\bar{t}/W$  and  $Z_{inv}$ ) is predicted using several control regions. In order to determine the uncertainty in the  $H_T$  shape, a combined linear fit is made over all relevant control regions. A requirement of at least 10 events and a non-trivial number of degrees of freedom is made to ensure a reasonable fit. Where this requirement is not satisfied, the  $H_T$  distribution is not used in the signal region. An  $H_T$  requirement of 130 GeV is made to ensure a similar phase space to the signal region. The uncertainty on the linear parameter from the fit is then used to define the  $\pm 1\sigma$  variations of the nominal template. As a conservative estimate, the systematic uncertainty in each category, and separately for  $Z_{inv}$  and  $t\bar{t}/W$ , is defined using the best fit value of the  $p_1$  parameter from the simultaneous fit to the relevant control regions added in quadrature to its uncertainty.

An additional validation is carried out by comparing expected and observed uncertainties on the linear parameter defining the template variations. The expected uncertainties are derived by using a linear fit to the simulation/simulation ratio where the numerator is treated as data. The relative uncertainties per 100 GeV from the weighted mean of  $H_T$  for  $t\bar{t}/W$  and  $Z_{inv}$  are shown in Figure 7.15 and Figure 7.16 and compared to those observed. These show good agreement, which provides additional motivation for the zero bias hypothesis as well as validating the method for deriving expected uncertainties.

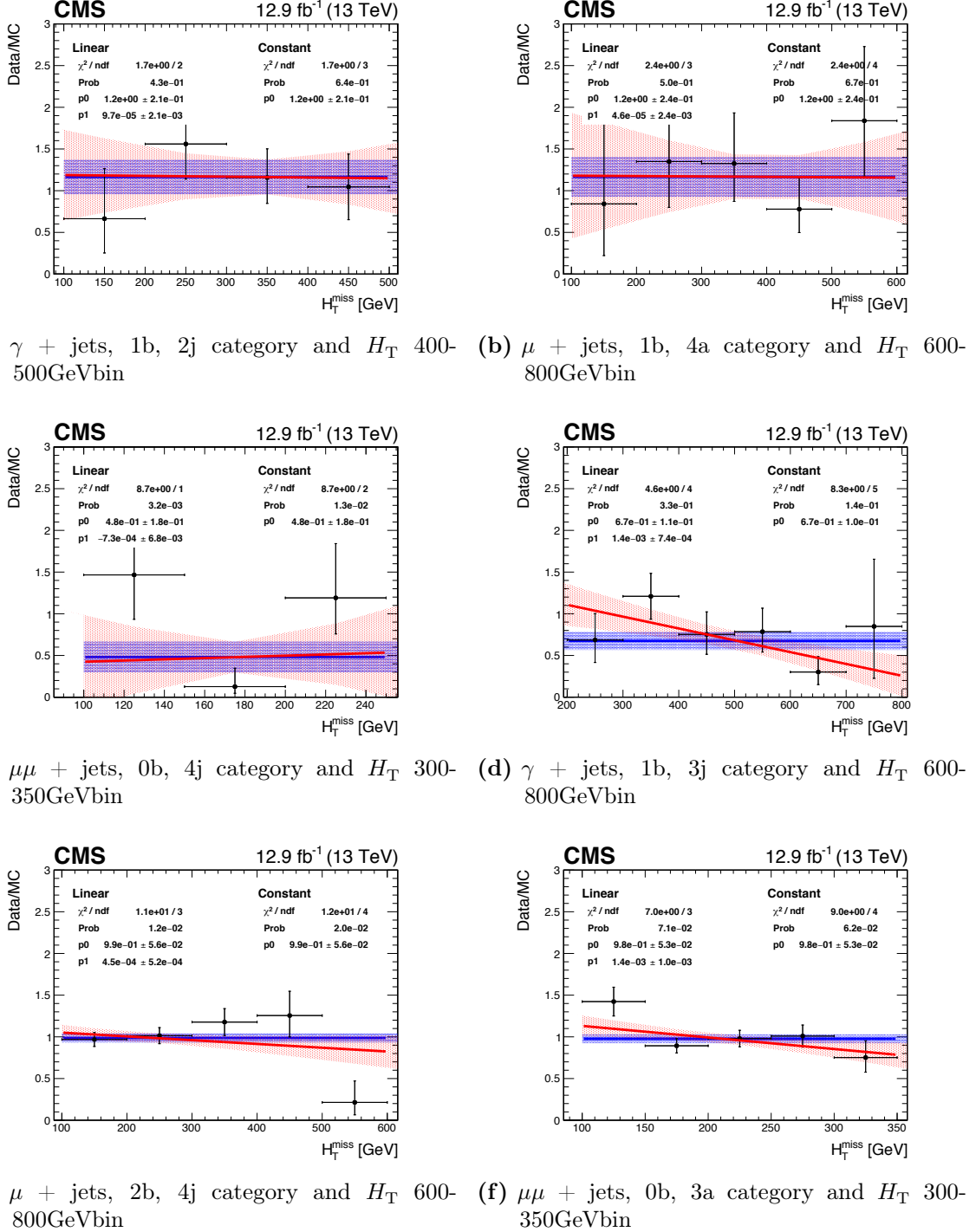


**Figure 7.11:** The data/simulation distribution against  $H_T$  for example categories and control regions. The large bias in the linear component seen in Figure 7.10 is mitigated.

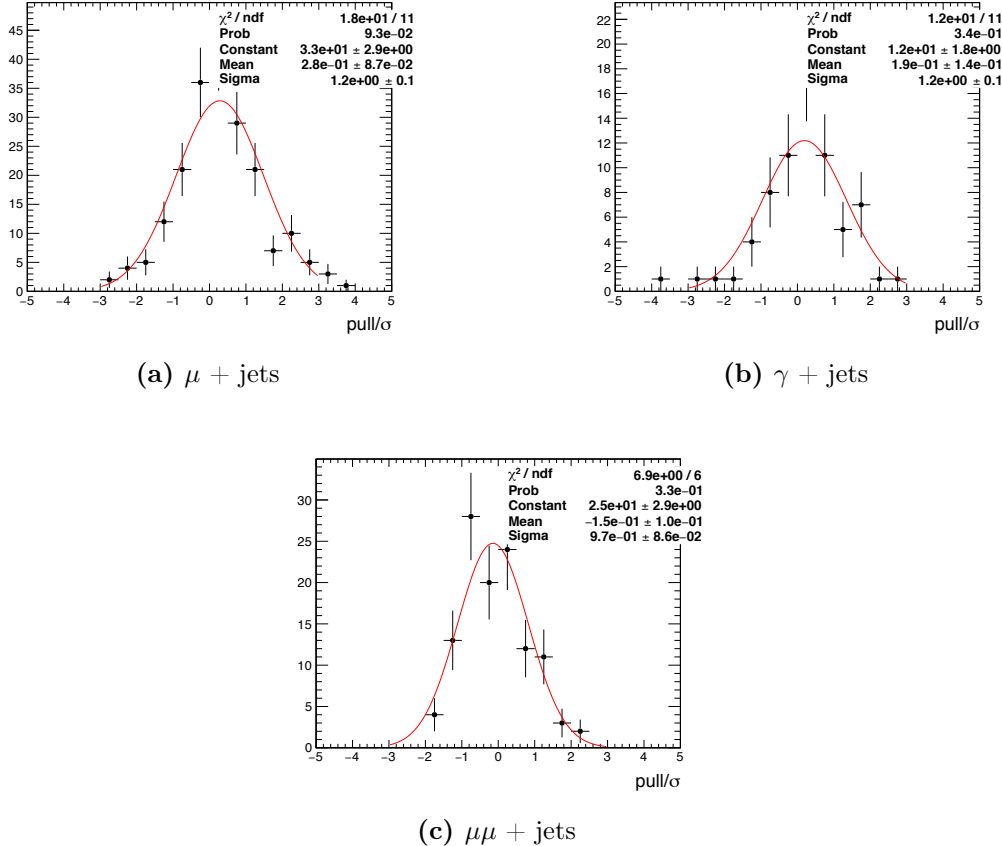


**Figure 7.12:** The pull distribution of the linear parameter from the flat hypothesis showing no significant bias.

### 7.5.3 Inclusion of systematic sources from simulation

The effects on the  $H_T$  shape of the uncertainties derived from variations in simulation (described in Section 7.4.1) are included within the likelihood. In this section, the size of the variation of the  $H_T$  distribution under  $\pm 1\sigma$  shifts of the sources of systematic uncertainty and the linear OP systematic uncertainty described in 7.5.1 are compared. In the likelihood, the  $H_T$  shape and transfer factors are varied simultaneously for each source of uncertainty, as discussed in Section 8.1.

To study the effect of the systematic variations on the  $H_T$  shape, figure 7.17 shows the  $H_T$  variations in two representative  $H_T$  bins and jet categories. The templates for each  $\pm 1\sigma$  variation are normalised to the nominal template such that only the shape is varied.

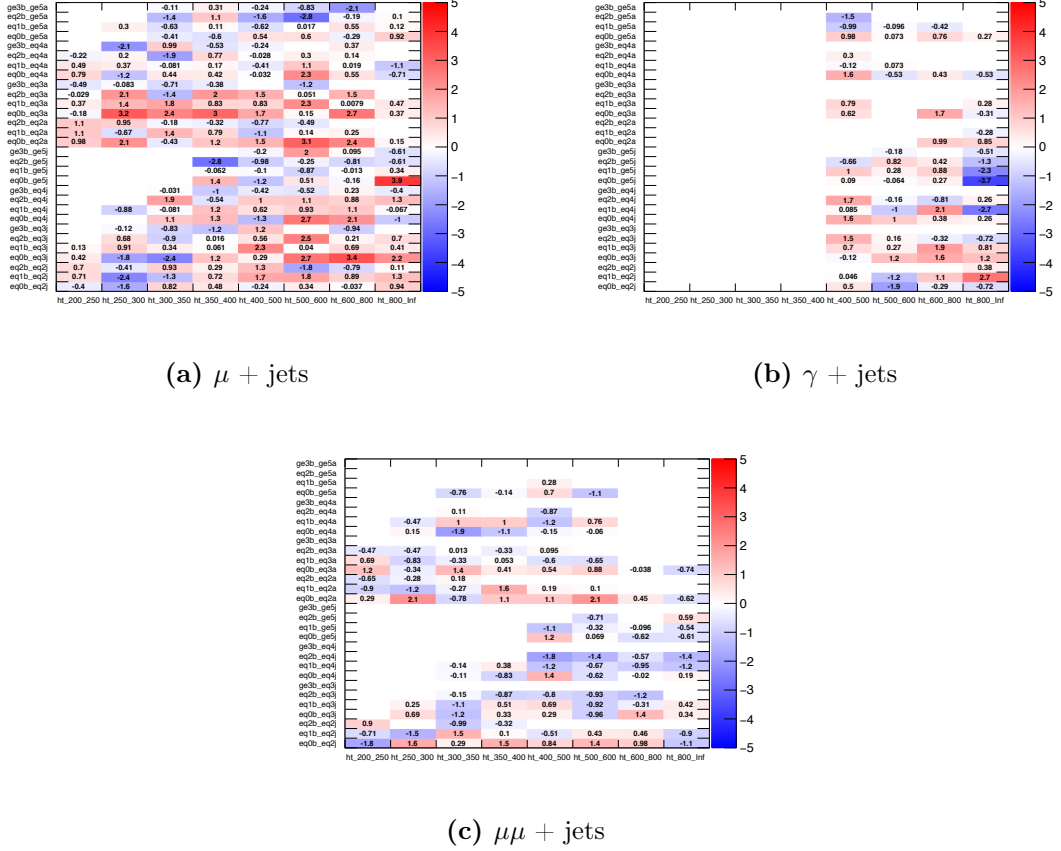


**Figure 7.13:** The pull distribution of the linear parameter from the flat hypothesis across all  $H_T$  bins and categories. There are no significant pulls for the  $H_T$  binned fits while the  $H_T$  inclusive case shows very large pulls as expected.

## 7.6 Summary

The methods described in this section provide a robust estimation of the contributions from both electroweak and QCD multijet background sources as well as the corresponding systematic uncertainties. These predictions must be confronted with the observed data using the likelihood model described in Chapter 8.

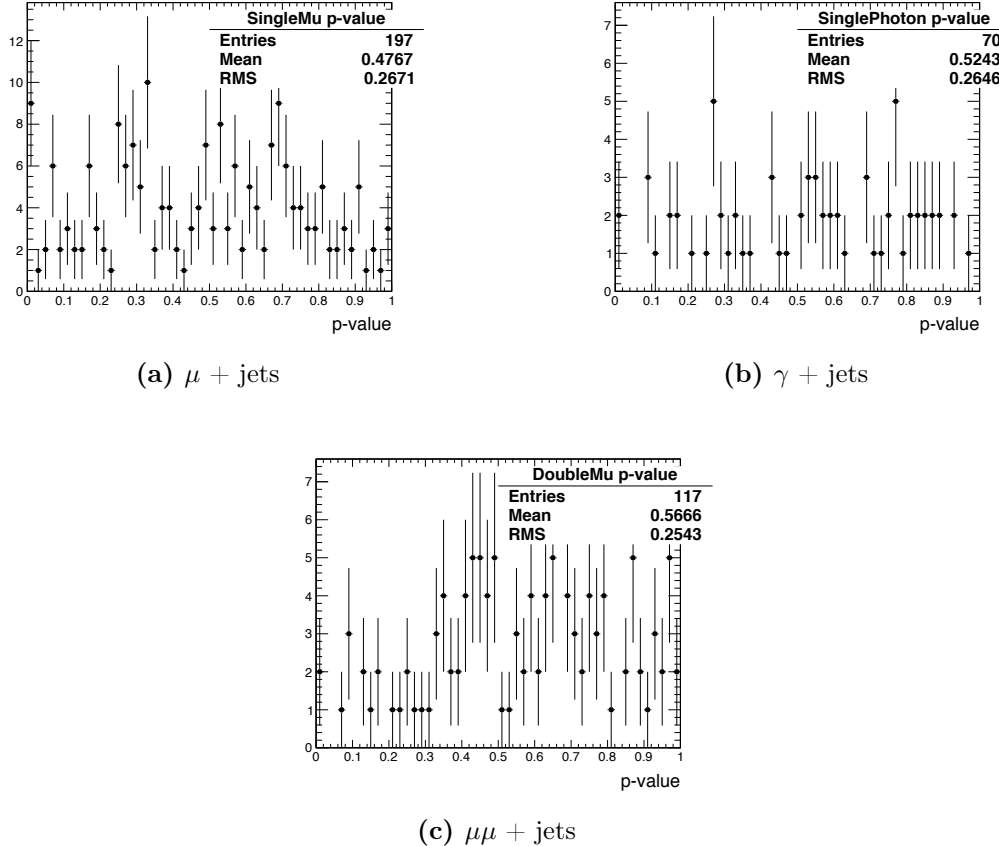


**Figure 7.14:** The distributions of the p-value for the linear fit.

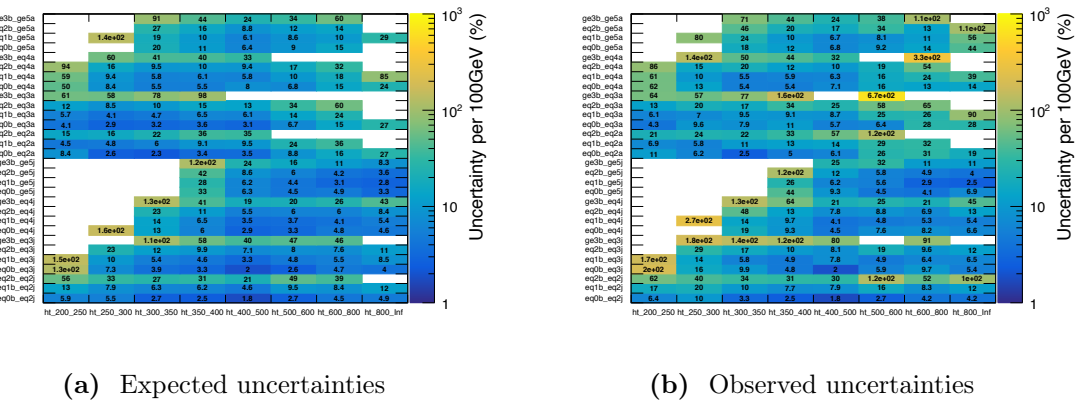


**Figure 7.15:** Expected relative uncertainties per 100 GeV shown for  $t\bar{t}/W$  in (a) are consistent with observed uncertainties shown in (b).

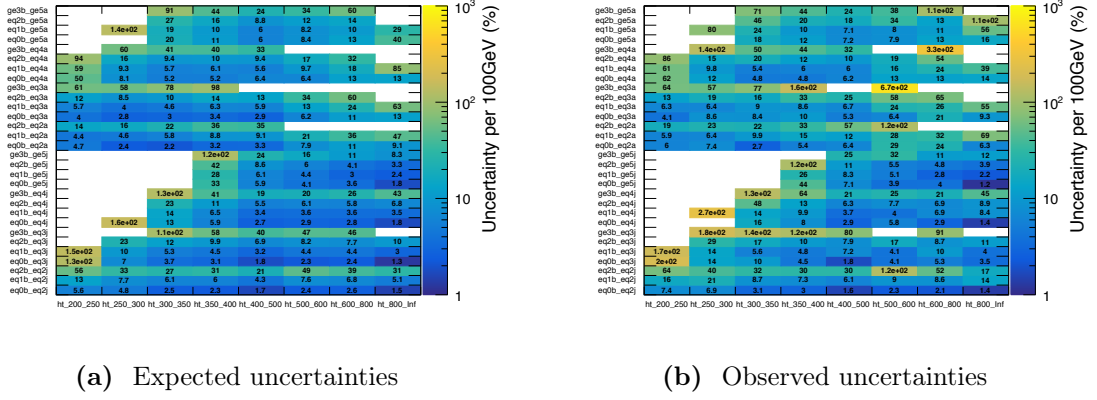


**Figure 7.16:** Expected relative uncertainties per 100 GeV shown for  $Z_{\text{inv}}$  in (a) are consistent with observed uncertainties shown in (b).

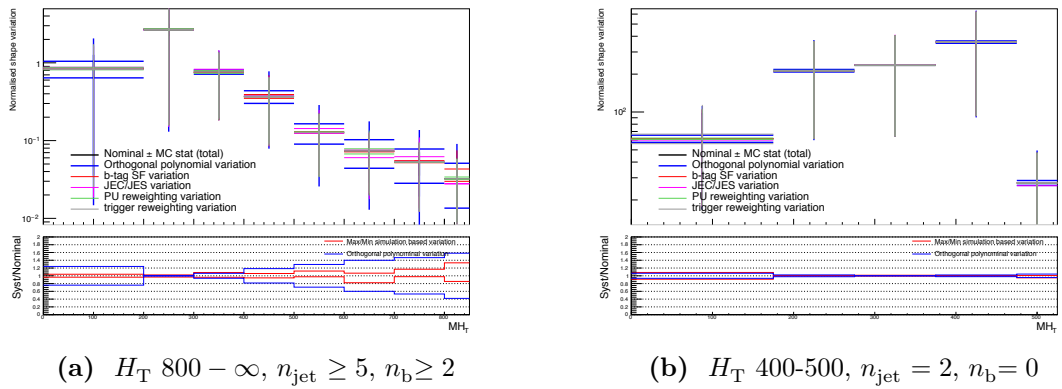


**Figure 7.17:** Simulation derived systematic variations on the  $H_T$  distribution compared to the linear OP data-driven systematic for two representative categories.

# Chapter 8

## Statistical results and interpretation

In this section the statistical results and interpretations are discussed. In Section 8.1 the likelihood model used to interpret the results of the  $\alpha_T$  search is detailed and in Section 8.2 the results of a maximum likelihood fit to the observed data presented. As no significant excess is seen the results are interpreted by setting upper limits at 95% confidence level (CL) on the cross section of supersymmetric simplified models. The procedure for setting the limits and the results are detailed in Sections 8.3.1 and 8.3.3 respectively. In this section the  $Z \rightarrow \nu\bar{\nu}$  background is labelled as  $Z_{\text{inv}}$  while the  $t\bar{t} + \text{jets}$  plus  $W + \text{jets}$  background is labelled as  $t\bar{t}W$ .

### 8.1 Likelihood model

The  $\alpha_T$  analysis relies on control regions to predict the normalisation of each category of  $n_{\text{jet}}$ ,  $n_b$  and  $H_T$  (which are in the following identified with  $H_T^{\text{cat}}$ ) and on simulation to predict the shape of  $\mathcal{H}_T$  within each category. The likelihood model is split into hadronic and control components linked by floating parameters for the prediction. In one  $H_T^{\text{cat}}$  category,  $j$ , the hadronic component may be written as a multiple of Poisson likelihoods for the observation in each  $\mathcal{H}_T$  bin ( $\text{Pois}(n|\lambda) \equiv e^{-n} \frac{\lambda^n}{n!}$ ):

$$\begin{aligned} \mathcal{L}_{\text{had}}^j = \prod_i \mathcal{L}_{\text{had}}^{j,i} &= \prod_i \text{Pois}(n_{\text{had}}^{j,i} | b_{Z_{\text{inv}}, \text{had}}^{j,i}) \times \phi^j(\mu \rightarrow Z_{\text{inv}}) \times a^j \times \rho_{Z_{\text{inv}}, \text{had}}^{j,i} + \\ b_{t\bar{t}W, \text{had}}^{j,i} \times \phi^j(\mu \rightarrow t\bar{t}W) \times a^j \times \rho_{t\bar{t}W, \text{had}}^{j,i} &+ b_{\text{QCD}, \text{had}}^{j,i} \times \omega_{\text{QCD}, \text{had}}^{j,i} + r \times s_{\text{had}}^{j,i} \times \rho_{s, \text{had}}^{j,i} \end{aligned} \quad (8.1)$$

where the product is over each  $\mathcal{H}_T$  bin,  $i$ , in the  $H_T^{\text{cat}}$  category;  $b_{Z_{\text{inv}}/t\bar{t}W,\text{had}}^{j,i}$  are the predicted number of events from simulation for the electroweak backgrounds;  $b_{\text{QCD,had}}^{j,i}$  are the predicted number of events for the QCD multijet component (from the method described in Section 7.3.2); the  $a^j$  parameter is unconstrained and connects the prediction of the signal region to the control regions (see below);  $\phi^j$  contains the systematic uncertainties on the transfer factors from the data-driven tests;  $\rho^{j,i}$  contains the systematics from variations in simulation, the systematics derived from the control regions on the  $\mathcal{H}_T$  shape and the uncertainty from the limited number of simulated events;  $r$  is the unconstrained ‘signal strength’ parameter and  $\omega_{\text{QCD,had}}^{j,i}$  contains the uncertainties on the QCD multijet component.

The component of the likelihood for the  $\mu + \text{jets}$  control region, which is not categorised in  $\mathcal{H}_T$ , can be written as:

$$\mathcal{L}_\mu^j = \text{Pois}(n_\mu^j | b_\mu^j \times a^j \times \rho_\mu^j + b_{\text{QCD},\mu}^j + r \times s_\mu^j \times \rho_{s,\mu}^j) \quad (8.2)$$

similarly to Equation 8.1,  $\rho_\mu^j$  contains the uncertainty in the  $H_T^{\text{cat}}$  from variations in simulation. The signal contamination in the control region is encoded by  $s_\mu^j$ , which is small by design. The connection between the control and signal region is included by the unconstrained  $a^j$  parameter and the subdominant QCD component,  $b_{\text{QCD},\mu}^j$ , is taken from simulation.

The  $Z_{\text{inv}}$  component in the signal region is also predicted using the  $\gamma + \text{jets}$  and  $\mu\mu + \text{jets}$  regions. By rewriting  $\phi^j(\mu \rightarrow Z_{\text{inv}}) \times a^j$  and  $\phi^j(\mu \rightarrow t\bar{t}W) \times a^j$  as  $a'(\mu \rightarrow Z_{\text{inv}})$  and  $a'(\mu \rightarrow t\bar{t}W)$  respectively, the connections to the  $\gamma + \text{jets}$  and  $\mu\mu + \text{jets}$  regions may be written as:

$$\mathcal{L}_{\mu\mu}^j = \text{Pois}(n_{\mu\mu}^j | b_{\mu\mu}^j \times \left(a'^j / \phi^j(\mu\mu \rightarrow Z_{\text{inv}})\right) \times \rho_{\mu\mu}^j + b_{\text{QCD},\mu\mu}^j + r \times s_{\mu\mu}^j \times \rho_{s,\mu\mu}^j) \quad (8.3)$$

$$\mathcal{L}_\gamma^j = \text{Pois}(n_\gamma^j | b_\gamma^j \times \left(a'^j / \phi^j(\gamma \rightarrow Z_{\text{inv}})\right) \times \rho_\gamma^j + b_{\text{QCD},\gamma}^j + r \times s_\gamma^j \times \rho_{s,\gamma}^j) \quad (8.4)$$

where parameters are defined as in Equations 8.1 and 8.2. In these equations the connection between the control and signal region is inverted and so  $\phi^j$  appears on the denominator.

The modifier and constraint terms of the parameters representing the systematic uncertainties and connections between control and signal regions are summarised below:

- The transfer factor systematics and uncertainties on the QCD multijet contribution are taken to be ‘log normal’ uncertainties such that the logarithm of the variable has a Gaussian (normal) constraint [102]. These uncertainties are correlated per topology and  $H_T$  bin (pair of  $H_T$  bins for uncertainties derived using  $\mu\mu + \text{jets}$ )
- The systematic uncertainties from variations in simulation and those derived on the  $H_T$  shape from the control regions are included using ‘vertical template morphing’ [102]. For vertical template morphing, the yield in each bin is interpolated quadratically between the  $\pm 1\sigma$  variations for each source of uncertainty and extrapolated linearly beyond this range. The constraint term is Gaussian with mean 0 and width 1. The uncertainties from simulation and those derived from the control regions are fully correlated and uncorrelated across all categories respectively.
- The Poisson uncertainty due to the limited number of simulated events is approximated using two parameters per bin that multiply the total background and signal contributions and are Gaussian constrained. These uncertainties are fully uncorrelated across all categories.

The total likelihood (including the constraint terms in  $\mathcal{L}_{\text{constraint}}$ ) can be written as a product over all  $H_T^{\text{cat}}$  bins:

$$\mathcal{L} = \mathcal{L}_{\text{constraint}} \times \prod_{j \in H_T^{\text{cat}}} \mathcal{L}_{\text{had}}^j \times \mathcal{L}_{\mu\mu}^j \times \mathcal{L}_\gamma^j \times \mathcal{L}_\mu^j \quad (8.5)$$

## 8.2 Results of the fit to data

The expected number of events from the SM backgrounds are determined from a simultaneous fit over all parameters using data from the control regions only, ‘CR-only fit’ as well as using data from all regions, ‘full fit’. The CR-only fit provides the best representation of the background predictions of the  $\alpha_T$  search from the control regions.

In Figures 8.1, 8.2 and 8.3 the results of the CR-only fit and the full fit are presented in all  $H_T$ ,  $n_{\text{jet}}$  and  $n_b$  categories under a SM-only hypothesis ( $r = 0$ ) for the monojet, asymmetric and symmetric categories respectively. No significant tension is observed between the predictions and data. Additionally, in Figure 8.4, the distribution in  $H_T$

for representative categories of  $H_T$ ,  $n_{\text{jet}}$  and  $n_b$ , sensitive to hadronic SUSY models with TeV scale squarks and gluinos, shows good agreement between prediction and data.

The fine binned categorisation can complicate the comprehension of the global agreement between data and prediction across the signal region. In Section 9.1 the result is presented using ‘aggregated regions’ in which the categorisation is merged.

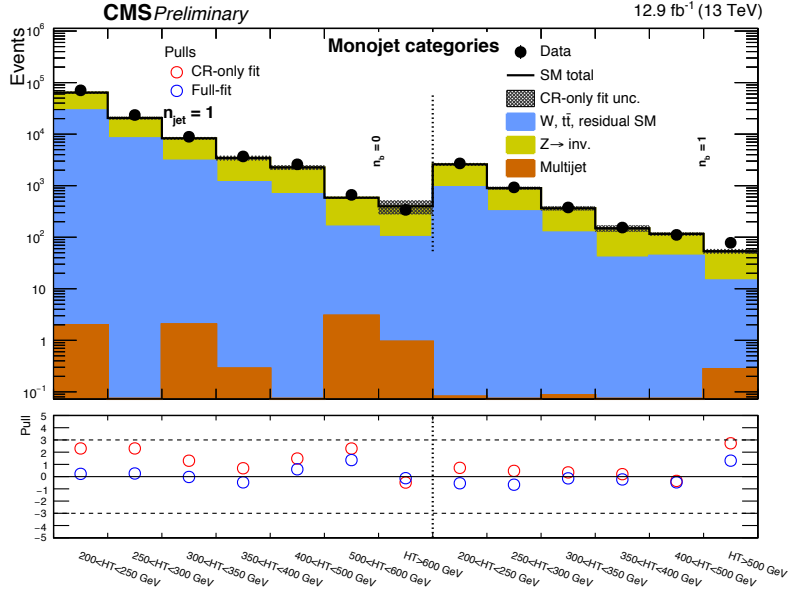


**Figure 8.1:** Top panel: event yields observed in data (solid circles) with their associated Poisson uncertainties represented by error bars are compared to SM predictions with associated uncertainties (black histogram with shaded band) from a CR-only fit as a function of  $n_b$  and  $H_T$  for the monojet topology in the signal region. Bottom panel: the significance of deviations (pulls) observed in data with respect to the SM expectations from the CR-only (red circles) and full fit (blue circles). The pulls are indicative only and cannot be considered independently.

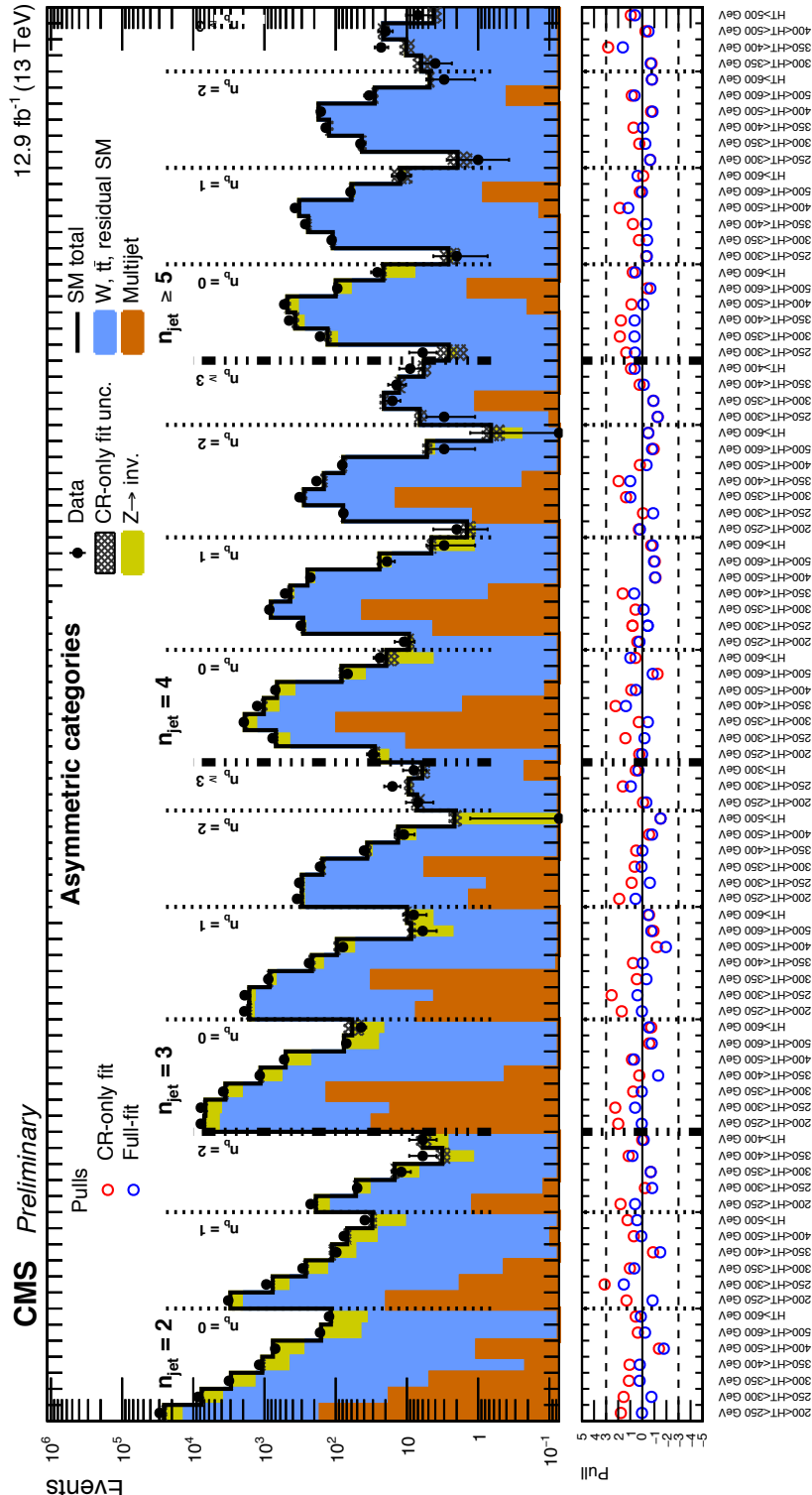


**Figure 8.2:** Top panel: event yields observed in data (solid circles) with their associated Poisson uncertainties represented by error bars are compared to SM predictions with associated uncertainties (black histogram with shaded band) from a CR-only fit as a function of  $n_{jet}$ ,  $n_b$  and  $H_T$  for the asymmetric topology in the signal region. Bottom panel: the significance of deviations (pulls) observed in data with respect to the SM expectations from the CR-only (red circles) and full fit (blue circles). The pulls are indicative only and cannot be considered independently.

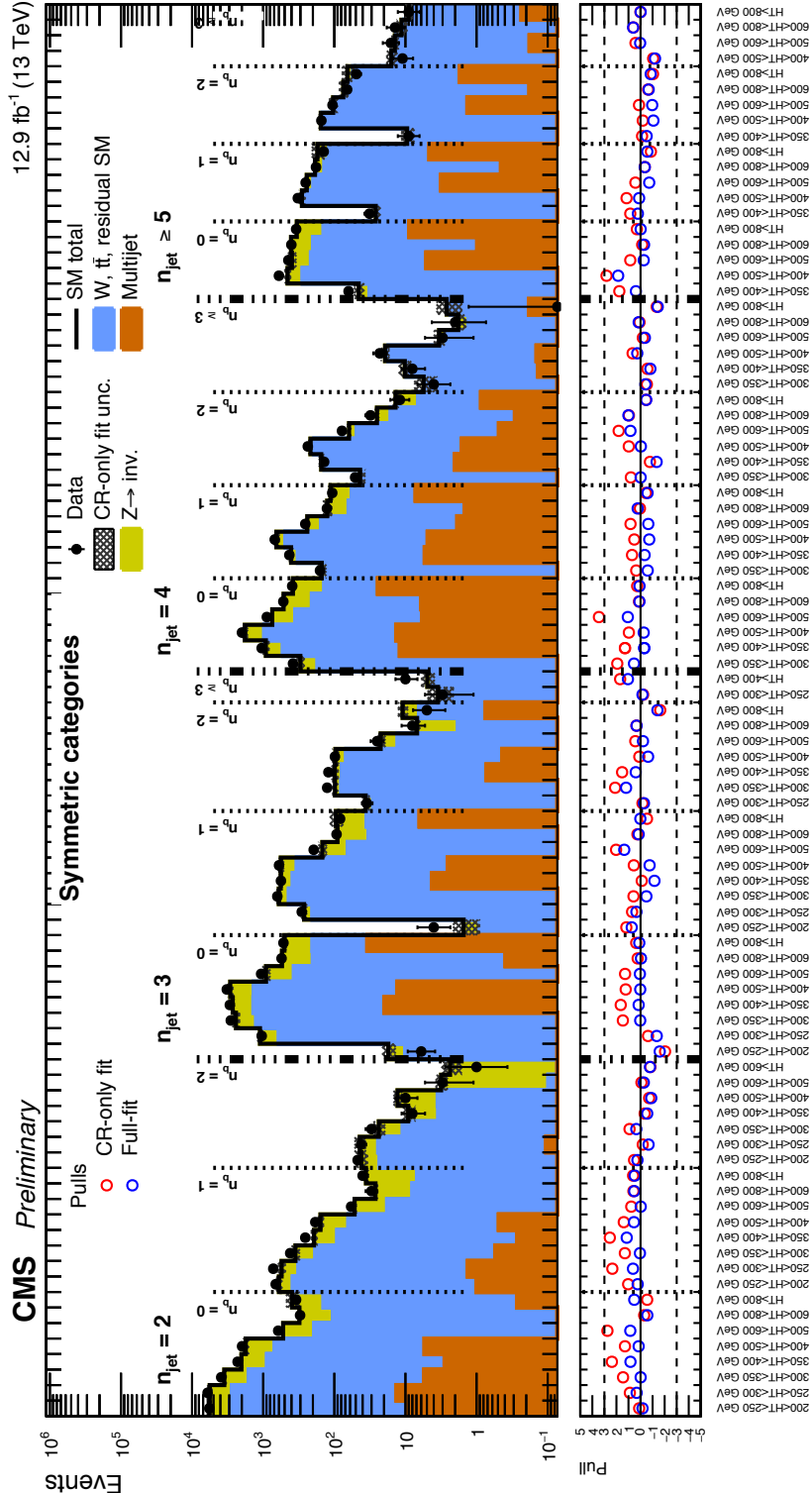


**Figure 8.3:** Top panel: event yields observed in data (solid circles) with their associated Poisson uncertainties represented by error bars are compared to SM predictions with associated uncertainties (black histogram with shaded band) from a CR-only fit as a function of  $n_{jet}$ ,  $n_b$  and  $H_T$  for the symmetric topology in the signal region. Bottom panel: the significance of deviations (pulls) observed in data with respect to the SM expectations from the CR-only (red circles) and full fit (blue circles). The pulls are indicative only and cannot be considered independently.

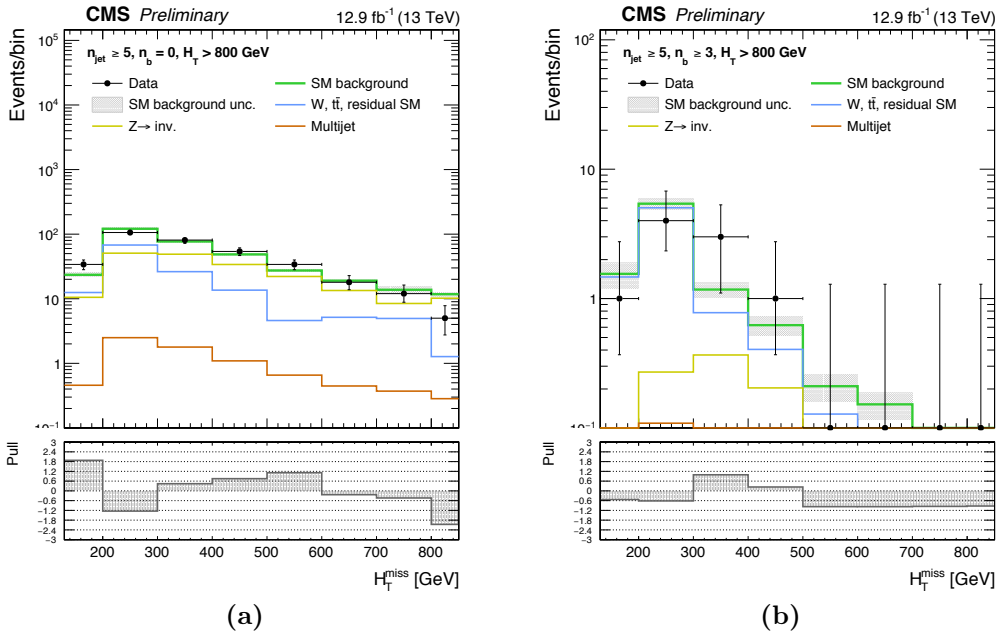


**Figure 8.4:** Event yields observed in data (solid circles) and SM expectations from the CR-only fit with their associated uncertainties (green histogram with shaded band) as a function of  $H_T$  for events in the signal region that satisfy  $n_{\text{jet}} \geq 5$ ,  $H_T > 800 \text{ GeV}$ , and (a)  $n_b = 0$  or (b)  $n_b \geq 3$ . The final bin is the overflow bin. The bottom panels indicate the significance of the deviations (pulls) observed in data with respect to the SM expectations, expressed in terms of the total uncertainty in the SM expectations. The pulls are indicative only and cannot be considered independently.

## 8.3 Interpretation

Given the agreement between prediction and results presented in Section 8.2, no evidence for BSM physics is observed. The results are therefore used to constrain the parameter space of simplified supersymmetric models. The simplified models considered are the gluino-mediated and direct production of both bottom and top squark pairs. The  $\alpha_T$  search is expected to be particularly sensitive to such topologies due to the significant hadronic activity, bottom quarks, jet multiplicity and  $H_T$  that may be present in the final state. Limits at 95% confidence level (see Section 8.3.1) are set on the production cross section of each model.

### 8.3.1 Procedure for deriving limits

This section outlines the procedure for deriving the upper limits on the signal strength at 95% confidence level. A more comprehensive treatment can be found in [103].

In the following section, the signal strength is considered to be the parameter of interest and all other parameters in the fit are termed the ‘nuisance parameters’ ( $\boldsymbol{\theta}$ ). Considering the likelihood defined in Equation 8.5, the profile likelihood ratio can be defined as

$$q(r) = \frac{\mathcal{L}(r, \hat{\boldsymbol{\theta}}(r))}{\mathcal{L}(\hat{r}, \hat{\boldsymbol{\theta}})}, \quad (8.6)$$

where  $\hat{\boldsymbol{\theta}}$  and  $\hat{r}$  are the values of  $\boldsymbol{\theta}$  and  $r$  that maximise  $\mathcal{L}$ , maximum-likelihood (ML) estimators, while  $\hat{\boldsymbol{\theta}}(r)$  is the value of  $\boldsymbol{\theta}$  that maximises  $\mathcal{L}$  for the specified value of  $r$ .

Given that  $r < 0$  is unphysical the profile likelihood is modified to

$$\tilde{q}(r) = \begin{cases} q(0) & r \leq 0, \\ q(r) & r > 0. \end{cases} \quad (8.7)$$

The test statistic used to derive the upper limit on  $r$  can then be defined as

$$t_r = \begin{cases} -2 \ln \tilde{q}(r) & \hat{r} \leq r, \\ 0 & \hat{r} > r. \end{cases} \quad (8.8)$$

Considering Equation 8.6,  $t_r$  will be zero at the ML value of  $r$ . Increasing values of  $t_r$  represent lesser compatibility of that value of  $r$  with the observed data. The test statistic is set to zero for  $\hat{r} > r$  as values of  $r$  less than  $\hat{r}$  are not part of the ‘rejection region’ for upper limits.

The probability density function,  $f(t_r|r)$ , for  $t_r$  may be built by generating pseudo-experiments or approximated using the asymptotic formulae detailed in [103]. The  $\alpha_T$  analysis uses the asymptotic approximation for  $f(t_r|r)$ . The  $p$ -value,  $p_r$ , is defined as

$$p_r = \int_{t_{r,obs}}^{\infty} f(t_r|r) dt_r, \quad (8.9)$$

where  $t_{r,obs}$  is the observed value of the test statistic. Finally, the CLs is defined as

$$\text{CLs}(r) = \frac{p_r}{1 - p_0}. \quad (8.10)$$

The upper limit on  $r$  is defined as the value of  $r$  which corresponds to  $\text{CLs}(r) = 0.05$  ( $r_{95}$ ). Values of  $r$  greater than this are said to be excluded at 95% confidence level.

The expected limit on a given signal strength,  $r_{95}^{exp}$ , is defined by the median value of the distribution of  $r_{95}$  built from pseudo-datasets generated with no signal contribution ( $r = 0$ ). The variation in the expected limit may be extracted from the relevant quantiles of this distribution. For the  $\alpha_T$  analysis, the value and  $\pm 1\sigma$  variations of  $r_{95}^{exp}$  are approximated using the asymptotic formulae detailed in [103].

### 8.3.2 Signal model contribution and systematic uncertainties

The experimental efficiency times acceptance ( $\epsilon \times A$ ) in both the signal and control regions is derived independently for each signal model for each gluino or squark mass

( $m_{\text{SUSY}}$ ) and neutralino mass ( $m_{\tilde{\chi}^0}$ ). As for the background processes, the simulated events for the signal contribution are corrected for jet energy corrections, b tag scale factors, lepton scale factors, pile-up modelling and trigger efficiencies. In addition, a correction is made to account for differences observed in the initial state radiation modelling between data and simulation. Systematic uncertainties are included on each of these corrections, analogously to the systematic uncertainties on the background processes derived from variations in simulation. The signal contribution cannot be predicted using data and therefore the overall normalisation contains an uncertainty from the luminosity measurement of 6.2%. All systematics are summarised in Table 8.1, including typical magnitudes for direct bottom squark production.

**Table 8.1:** Representative magnitudes of systematic uncertainties in the experimental acceptance for a simplified model that assumes the pair production of bottom squarks and their decay to a b quark and a  $\tilde{\chi}^0$ .

Systematic source	Correlated	Typical magnitude (%)
Luminosity	Yes	6.2
Monte Carlo statistics	No	1–50
Jet energy scale	Yes	3–10
B tag efficiency scale factors	Yes	5–40
Lepton scale factors	Yes	1–5
Pileup	Yes	0–5
Trigger efficiency	Yes	0–4
Initial state radiation	Yes	1–20

### 8.3.3 Upper limits on signal production cross section

In Figure 8.5 the upper limits at 95% CL set on the production cross section are shown in the ( $m_{\text{SUSY}}, m_{\tilde{\chi}^0}$ ) plane for the models considered. Also shown are the expected and observed contours of  $r_{95} = 1$ , the  $\pm 1$  and  $2 \sigma$  variations in the expected limit, and the observed limit under  $\pm 1 \sigma$  variations in the theoretical cross section uncertainty. Models with  $r_{95} < 1$  are ‘excluded’ at 95% CL.

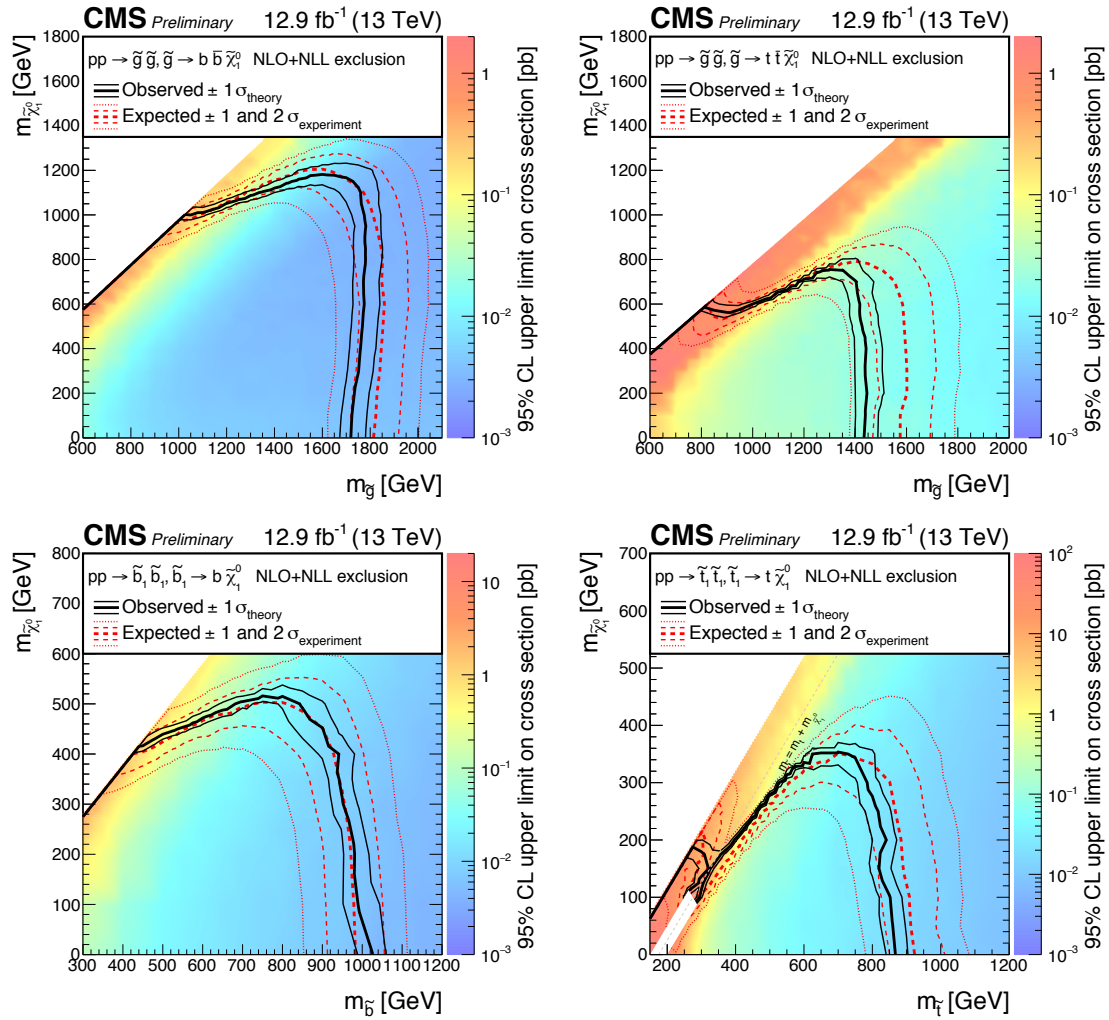


**Figure 8.5:** Observed upper limit in cross section at 95% confidence level (indicated by the colour scale) for simplified models that assume the (Top) gluino-mediated or (Bottom) direct production of (Left) bottom or (Right) top squark pairs, as a function of the gluino or squark mass and the  $\tilde{\chi}_1^0$  mass. The black solid thick (thin) line indicates the observed mass exclusion regions assuming the nominal ( $\pm 1\sigma$  theory uncertainty) production cross section. The red dashed thick (thin) line indicates the median ( $\pm 1\sigma$  experimental uncertainty) expected mass exclusion regions.

**Table 8.2:** Summary of the mass limits obtained for the four classes of simplified models. The limits indicate the strongest observed (expected) mass exclusions for the gluino or squarks, and  $\chi_1^0$  [23].

Production mode	Squark	Strongest obs. (exp.) mass exclusion [GeV]			
		$\alpha_T$ (13 TeV)		Run 1 (7 TeV + 8 TeV)	
		Gluino or squark	$\chi_1^0$	Gluino or squark	$\chi_1^0$
Gluino-mediated	Bottom	1775 (1850)	1175 (1200)	1375	725
Gluino-mediated	Top	1450 (1600)	750 (800)	1325	625
Direct	Bottom	1025 (975)	525 (500)	725	325
Direct	Top	875 (925)	350 (350)	775	300

## 8.4 Summary

The results of the  $\alpha_T$  analysis with  $12.9 \text{ fb}^{-1}$  of p-p collision data have shown no significant evidence of BSM physics. Upper limits at 95% CL have therefore been set on a range of supersymmetric simplified models. In Table 8.2, the highest mass of squark or gluino and  $\chi_1^0$  excluded at 95% confidence level are shown for each model and compared to the highest values excluded by searches on the full 7 and 8 TeV Run 1 CMS datasets. A significant increase in reach of 100 to 400 GeV in the squark/gluino mass and 50 to 425 GeV in the mass of the  $\chi_1^0$  is achieved.

The improvements in sensitivity are driven by both the increase in the centre of mass energy and by improvements in the analysis strategy. Such improvements include the addition of the  $H_T$  dimension and the use of the  $\mu + \text{jets}$  control region to predict  $Z_{\text{inv}}$ .

The results presented in this section may be used to derive limits on BSM physics models not considered for this thesis. Such ‘re-interpretations’ of the  $\alpha_T$  search are discussed in Chapter 9.

# Chapter 9

## Facilitating re-interpretation

The results of the  $\alpha_T$  search have been interpreted using limits on simplified model spectra which allow the sensitivity of the search to different topologies to be benchmarked. The search will be sensitive to a wide range of BSM models and can be re-interpreted by those outside the CMS collaboration to provide constraints on such models.

The  $\alpha_T$  search, like many searches for BSM physics with the CMS detector, uses a fine categorisation to separate background from signal contributions. To re-interpret such a search the signal yield is typically evaluated using an event generator such as PYTHIA8 followed by a simulation of the detector response and resolution using tools such as DELPHES [104] or using published efficiencies for generator level quantities (both methods are used in [22, 105, 106]). The background contributions to the search regions and the associated systematic uncertainties often rely on simplifying assumptions which can lead to inaccuracies in the re-interpretation.

In this section, a procedure for re-interpreting BSM physics searches by approximating the full background model and the associated systematic uncertainties is presented. The procedure involves techniques both to simplify the categorisation of the search ('aggregation') and to use a reduced set of information to describe the background model and the correlations between different search regions ('simplified likelihood'), minimising the loss of sensitivity. The  $\alpha_T$  search is used to validate and illuminate the use of such techniques; however, they are applicable for a wide range of searches and a general treatment may be found in [107].

## 9.1 Aggregation

The  $\alpha_T$  analysis uses a fine categorisation in  $n_{\text{jet}}$ ,  $n_b$ ,  $H_T$ , and  $\mathcal{H}_T$  to provide sensitivity to a wide range of BSM physics models. This categorisation makes re-interpreting the results of the search too computationally intensive to be feasible. The simplest method to reduce the complexity of the search is to take only the most sensitive categories for the BSM physics model; however, this breaks the correlation model for the search and can significantly reduce the sensitivity due to the loss of indirect constraints from the neglected bins.

In this section, the definition of aggregated regions using the full likelihood is presented. The aggregated regions allow the categorisation to be simplified without breaking the background model.

### 9.1.1 The aggregated region likelihood

Consider the hadronic component of the likelihood defined in Equation 8.1. The aggregated region likelihood is defined by summing the contributions within the Poisson for each  $\mathcal{H}_T$ ,  $H_T$ ,  $n_b$  and  $n_{\text{jet}}$  category which is to be aggregated as:

$$\begin{aligned} \mathcal{L}_{\text{had}}^{\text{agg}} = \prod_{\text{agg}_k} L_{\text{had}}^{\text{agg}_k} = \text{Pois}\left(\sum_{i,j \in \text{agg}_k} n_{\text{had}}^{j,i} \mid \sum_{i,j \in \text{agg}_k} b_{Z_{\text{inv}},\text{had}}^{j,i} \times \phi^j(\mu \rightarrow Z_{\text{inv}}) \times a^j \times \rho_{Z_{\text{inv}},\text{had}}^{j,i} + \right. \\ \left. b_{t\bar{t}W,\text{had}}^{j,i} \times \phi^j(\mu \rightarrow t\bar{t}W) \times a^j \times \rho_{t\bar{t}W,\text{had}}^{j,i} + b_{\text{QCD},\text{had}}^{j,i} \times \omega_{\text{QCD},\text{had}}^{j,i} \right. \\ \left. + r \times s_{\text{had}}^{j,i} \times \rho_{s,\text{had}}^{j,i}\right). \quad (9.1) \end{aligned}$$

The control region component of the likelihood is unchanged such that the prediction model is maintained from the full likelihood. This allows, for example, events at different scales to be included within the same aggregated region without introducing bias from mixing events at different scales.

### 9.1.2 Definition of aggregated regions

The categorisation used for the full likelihood is summarised in Section 6.5. The large number of categories provides generic sensitivity but is not optimal for re-interpretation.

The thirty-one jet categories are therefore reduced to eight aggregated jet categories while the (up to) eight  $H_T$  bins are merged into one bin ( $H_T \geq 200$  GeV). The final categories are shown in Table 9.1. These are defined to be disjoint, contiguous and to cover the full signal region such that in combination the regions reflect the sensitivity of full signal region phase space.

**Table 9.1:** To define the aggregated regions for the  $\alpha_T$  search the  $H_T$  dimension is merged to  $\geq 200$  GeV and  $n_b$  to two categories of  $n_b < 2$  and  $\geq 2$ . The merged  $n_{jet}$  categories are summarised in this table. Each category is further binned using eight  $H_T$  bins with lower bounds from 100 to 800 GeV.

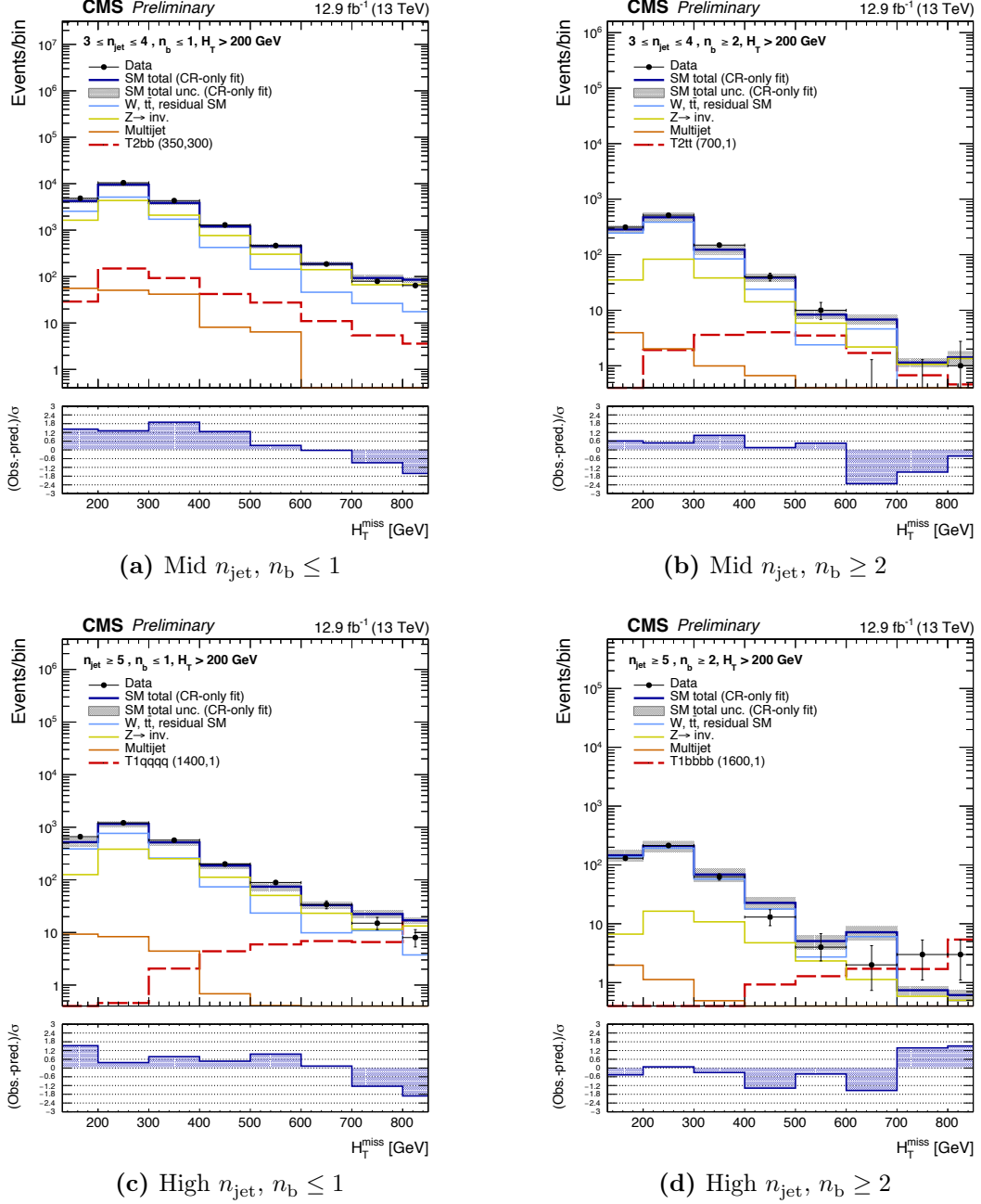
$n_{jet}$ topology	Merged jet categories		
	Monojet	Asymmetric	Symmetric
Monojet-like	1	2	2
Asymmetric high $n_{jet}$	-	3, 4, $\geq 5$	-
Mid $n_{jet}$	-	-	3, 4
High $n_{jet}$	-	-	$\geq 5$

The jet categories are merged into four separate categories motivated by their sensitivity to different BSM physics topologies. For example, the monojet-like topology is targeted towards compressed spectra while the high  $n_{jet}$  topology targets uncompressed gluino and squark models. The  $n_b$  categories are combined as  $n_b = 0, 1$  and  $n_b \geq 2$ , targeted at light and heavy flavour BSM physics respectively. Finally, the  $H_T$  dimension is entirely merged as the  $H_T$  dimension generally provides better sensitivity for BSM physics models. The use of the aggregated regions ensures that the backgrounds are still predicted by the nominal, finely binned regions (with appropriate systematics).

### 9.1.3 Results using aggregated regions for the $\alpha_T$ analysis

The aggregated regions provide an easily comprehensible overview of the signal region when compared to the results of the nominal signal bins. Figure 9.1 shows the post-fit predictions in the mid and high  $n_{jet}$  categories for the aggregated regions compared to the observed data.

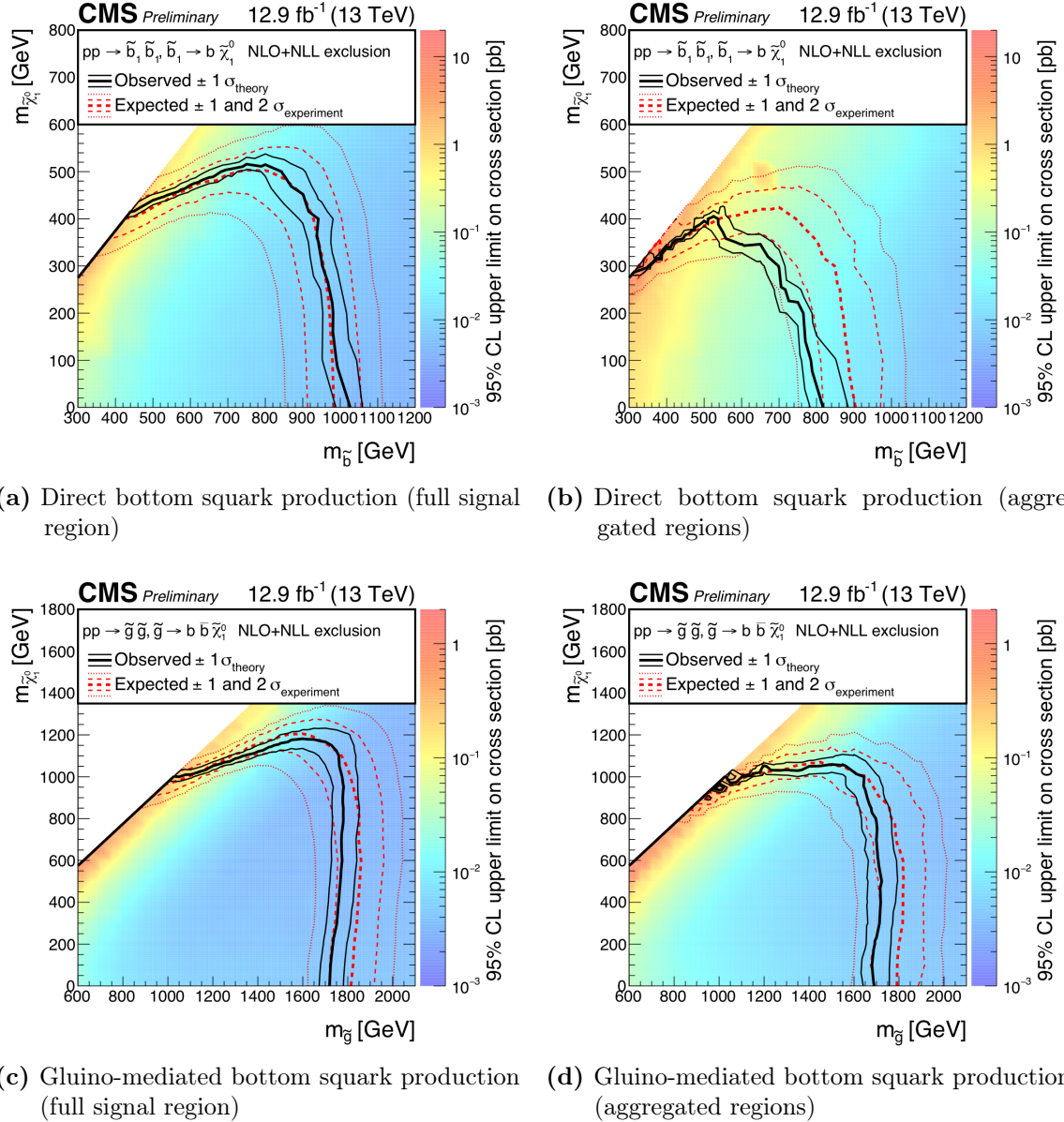
**Figure 9.1:** Signal region predictions and data observations for the aggregated regions. The predictions are made using a fit to the control region only.



To evaluate the effect of using aggregated regions on the sensitivity of the  $\alpha_T$  analysis, the expected and observed 95% upper limit on the signal strength for the full signal region is compared to the limits derived using the aggregated regions. The limits are shown side by side in Fig 9.2 for the simplified models of direct and gluino mediated

bottom squark production. Where the mass splittings are small the expected limits typically reduce by  $\sim 100$  GeV compared to the full signal region.

**Figure 9.2:** Limit planes shown for both the full signal regions (left) and the aggregated regions (right).



## 9.2 Simplified likelihood

In this section a method for simplifying the likelihood by approximating the nuisance parameters using a multivariate Gaussian is described. The approximations and areas of applicability are discussed and a validation shown using the  $\alpha_T$  search.

### 9.2.1 Definition of the simplified likelihood

The form of the likelihood (either aggregated or full) used by the  $\alpha_T$  analysis (product of Poisson terms for the observation in each bin given the prediction and uncertainties) is typical of searches for BSM physics. Neglecting uncertainties on the signal contribution, the likelihood may be written as

$$\mathcal{L}(r, \boldsymbol{\theta}) = p(\tilde{\boldsymbol{\theta}}|\boldsymbol{\theta}) \times \prod_{i=1}^N Pois(n_i|r \cdot s_i + b_i + \theta_i). \quad (9.2)$$

where the product is over all categories (with total  $N$ ), all nuisance parameters have been included in the absolute variation in the total background in each category,  $\theta_i$ , and  $p(\tilde{\boldsymbol{\theta}}|\boldsymbol{\theta})$  is the probability density function for the measured values of the nuisances ( $\tilde{\boldsymbol{\theta}}$ ). The simplified likelihood is the approximation of the full probability density function as a multivariate Gaussian using the covariance between the categories. This approximation relies on the following (as detailed in [107]):

- The constraints on the background contributions are Gaussian such that the distribution of the total number of background events is symmetric about the expectation,  $b_i$ , with a variance independent of  $\boldsymbol{\theta}$ . For the  $\alpha_T$  search, as for many analyses, this assumption is valid because the background contributions are estimated using control regions in data with large sample sizes.
- The covariance, and therefore only the linear correlation, between the background contribution in each region is sufficient to approximate  $p(\tilde{\boldsymbol{\theta}}|\boldsymbol{\theta})$  at least for values of  $\boldsymbol{\theta}$  that are close to  $\tilde{\boldsymbol{\theta}}$ .
- The systematic uncertainties in the signal model can be neglected. The validity of this assumption will strongly depend on the specific BSM physics model being considered. Systematic uncertainties on the signal could be accounted for by adding appropriate nuisance parameters with Gaussian constraints (as for the background contributions), however, their derivation is not feasible for those outside the CMS collaboration.

Under these assumptions,  $p(\tilde{\boldsymbol{\theta}}|\boldsymbol{\theta})$  can be modelled as a multivariate Gaussian distribution with the mean vector identified with external measurements of  $\tilde{\boldsymbol{\theta}} = 0$ . The simplified likelihood can be expressed as

$$\mathcal{L}_S(r, \boldsymbol{\theta}) = \prod_{i=1}^N \frac{(r \cdot s_i + b_i + \theta_i)^{n_i} e^{-(r \cdot s_i + b_i + \theta_i)}}{n_i!} \cdot \exp\left(-\frac{1}{2} \boldsymbol{\theta}^T \mathbf{V}^{-1} \boldsymbol{\theta}\right), \quad (9.3)$$

where  $\mathbf{V}$  represents the covariance matrix for the expected background contributions across the search regions and is defined as

$$V_{ij} = E[\theta_i \times \theta_j], \quad (9.4)$$

where  $E[x]$  is the expectation value of  $x$ . The expectations and covariance must be derived following the fit over the control regions as these are not included when re-interpreting the search. The covariance matrix is determined using pseudo-experiments to sample the nuisance parameters.

As shown in [107], the covariance matrix may also be used to combine categories into aggregated regions with appropriate covariance between the bins. These aggregated regions and covariance may then be used to define the simplified likelihood.

### 9.2.2 Results for the $\alpha_T$ analysis

The covariance and predictions in the aggregated regions discussed in Section 9.1 are used to define and validate the simplified likelihood. Figure 9.3 (a) shows the value of  $q(r)$  as a function of  $r$  for a simplified model with direct bottom squark production and  $m_{\text{SUSY}} = 800 \text{ GeV}$  and  $m_{\chi^0} = 200 \text{ GeV}$ . The values of  $q(r)$  are compared to those derived using the full likelihood and using the simplified likelihood, ignoring correlations between the background expectations. The results using an Asimov dataset, assuming a signal strength of  $r = 0$ , are also shown as these are used to calculate limits using the asymptotic approximations detailed in Ref. [103]. The simplified likelihood, considering correlations, is shown to be in good agreement with the full likelihood while the agreement is worsened when correlations are neglected.

In Figure 9.3 (b) the ratio between the observed  $r_{95}$  for the simplified and the full likelihood is shown in the  $(m_{\text{SUSY}}, m_{\chi^0})$  plane for the simplified model of direct production of bottom squarks. The expected and observed contours of  $r = 1$  excluded at 95% for the

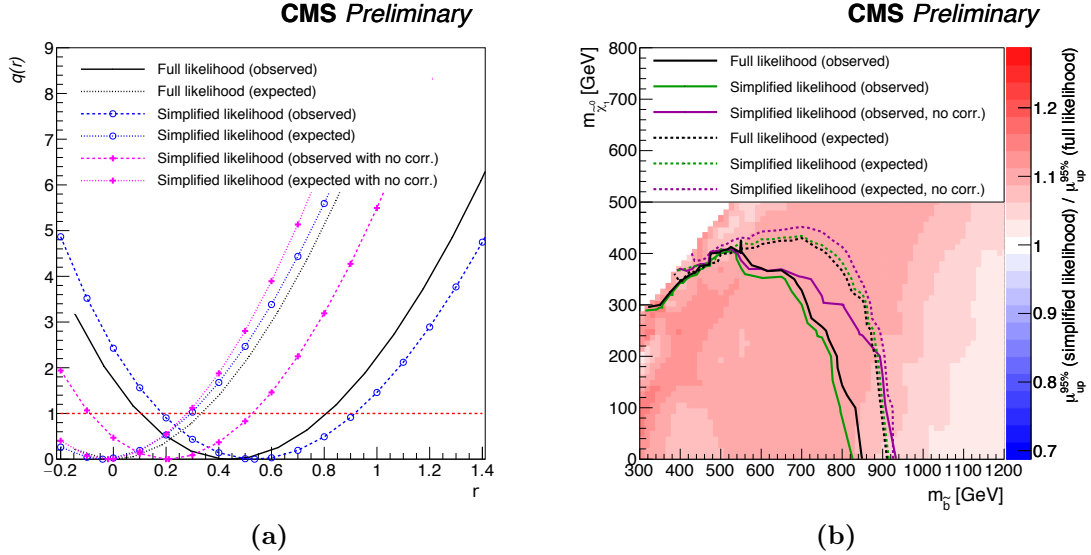


**Figure 9.3:** (a) The value of  $q(r)$  for the  $\alpha_T$  search derived with the simplified likelihood using the full covariance matrix, derived with the simplified likelihood assuming no correlations between the background yields and derived with the full likelihood. (b) Expected and observed exclusion contours for the  $\alpha_T$  search derived with the simplified likelihood using the full covariance matrix, derived with the simplified likelihood assuming no correlations between the background yields and derived with the full likelihood. The colour scale shows the ratio of  $r_{95}$  calculated derived with the simplified likelihood using the full covariance matrix to the value using the full likelihood.

full likelihood, the simplified likelihood and the simplified likelihood where correlations are neglected are overlaid. The results using the full and simplified likelihoods are seen to agree well when the correlations between bins are considered.

### 9.3 Summary

To re-interpret the  $\alpha_T$  search requires the background model and associated systematic uncertainties to be approximated. The categorisation may be robustly simplified through the use of aggregated search regions while the simplified likelihood method uses a multivariate Gaussian to approximate the systematic uncertainties. The simplified likelihood is shown to give comparable upper limits at 95% confidence level for a representative signal model. These methods may be applied to a wide range of searches for BSM physics; a general treatment is presented in [107].



# Chapter 10

## Conclusions

The  $\alpha_T$  search for SUSY has been presented using a  $12.9 \text{ fb}^{-1}$  dataset of  $13 \text{ TeV}$  p-p collisions collected by the CMS experiment. The search uses a hadronic final state containing jets and significant  $\cancel{E}_T$  to achieve sensitivity to a wide range of SUSY models. Dedicated variables, including  $\alpha_T$  and  $\Delta\phi_{\min}^*$ , are used to mitigate backgrounds and remaining contributions are robustly estimated using simulation and control regions in data. The results of the  $\alpha_T$  search following the strategy described in this thesis has been published using a  $2.3 \text{ fb}^{-1}$  dataset collected in 2015 [108] while the results of a search using the full  $36 \text{ fb}^{-1}$  dataset collected by CMS in 2016 is being prepared for submission.

Earlier incarnations of the  $\alpha_T$  analysis have been carried out on datasets of  $8 \text{ TeV}$  p-p collisions. The analysis has been fully updated and extended for the results presented in this thesis. In particular, the addition of the  $\cancel{H}_T$  dimension has robustly improved the sensitivity of the search. No evidence for BSM physics is observed and the results are therefore interpreted using simplified SUSY models. As shown in Chapter 8, the regions of parameter space excluded for both gluino mediated and direct bottom and top squark production have been significantly extended.

The  $\alpha_T$  search is sensitive to models not considered in the interpretations presented in this thesis. Such models include complete models of SUSY and generic models of dark matter. A procedure for facilitating the re-interpretation of the results of the search to evaluate the impact on such models has been presented. This procedure may be applied to a wide range of searches for BSM physics [107].

The L1 trigger jet and energy sum algorithms have been developed to take advantage of the upgraded L1 trigger hardware. These provide improved performance in jet identification, reconstruction and pileup mitigation. The upgraded algorithms have been

in use for the full 2016 dataset and have been exploited by the  $\alpha_T$  analysis in designing inclusive signal region selections.

No evidence has been found for BSM physics in the  $\alpha_T$  analysis or any search at CMS. The improvements to the analysis and substantial increase in centre of mass energy has provided significant gains in the excluded parameter space. The LHC will continue to provide data up to a luminosity of  $\sim 3000 \text{ fb}^{-1}$  over the remainder of its lifetime. The best opportunity for discovery of BSM physics is likely to come through exploiting this dataset using sophisticated analysis techniques as well as targeted searches for new types of signatures.

## Appendix A

## Transfer factors

The nominal values of the transfer factors from the control regions to the signal region are shown in Figures A.1 -A.2. Missing entries do not meet the requirement of statistical uncertainty from simulated events of less than 50%.

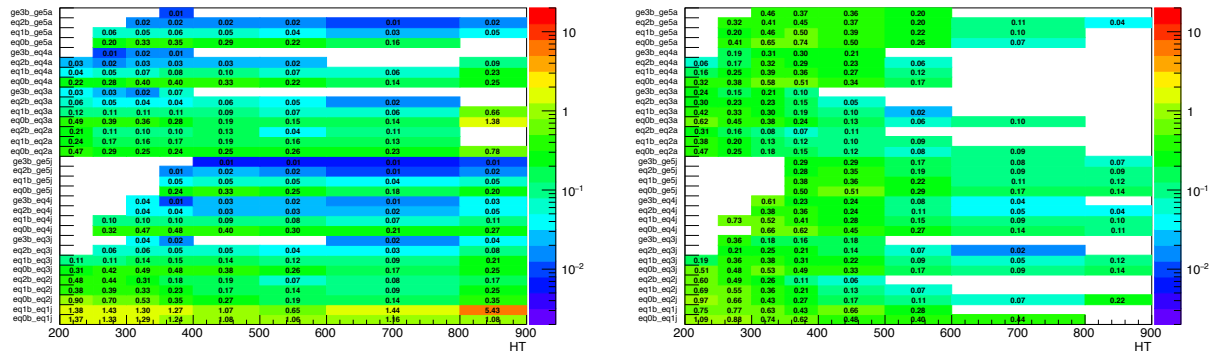


**Figure A.1:** The  $\mu +$  jets transfer factors as a function of  $H_T$  and jet category.

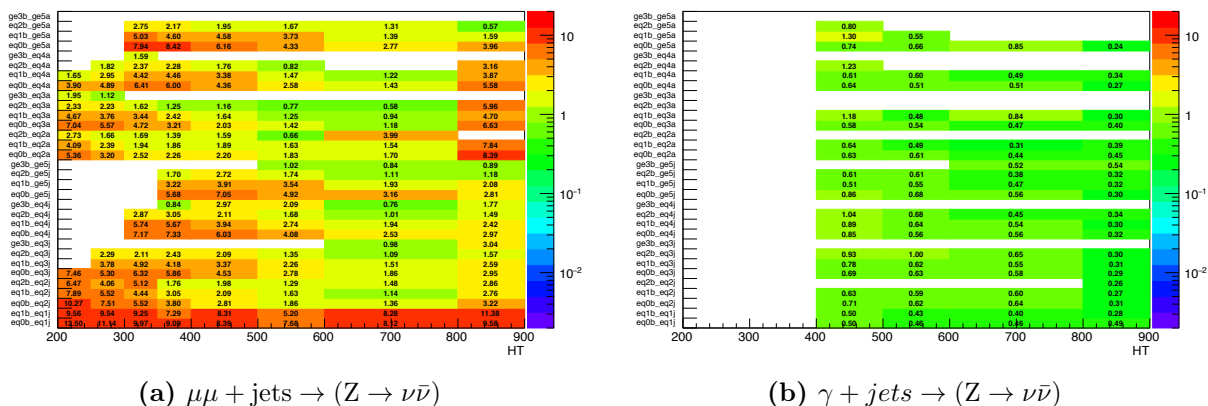


**Figure A.2:** The  $\mu\mu + \text{jets}$  and  $\gamma + \text{jets}$  transfer factors as a function of  $H_T$  and jet category.

# Bibliography

- [1] A. Shomer, “A Pedagogical explanation for the non-renormalizability of gravity”, [arXiv:0709.3555](https://arxiv.org/abs/0709.3555).
- [2] L. Bergstrom, “Dark Matter Evidence, Particle Physics Candidates and Detection Methods”, *Annalen Phys.* **524** (2012) 479–496, doi:[10.1002/andp.201200116](https://doi.org/10.1002/andp.201200116), [arXiv:1205.4882](https://arxiv.org/abs/1205.4882).
- [3] W. Buchmuller and C. Ludeling, “Field Theory and Standard Model”, in *High-energy physics. Proceedings, European School, Kitzbuehel, Austria, August 21-September, 2005.* 2006. [arXiv:hep-ph/0609174](https://arxiv.org/abs/hep-ph/0609174).
- [4] Particle Data Group Collaboration, “Review of Particle Physics”, *Chin. Phys. C* **40** (2016), no. 10, 100001, doi:[10.1088/1674-1137/40/10/100001](https://doi.org/10.1088/1674-1137/40/10/100001).
- [5] A. Pich, “The standard model of electroweak interactions”, in *High-energy physics. Proceedings, European School, Aronsborg, Sweden*, pp. 1–49. 2007. [arXiv:0705.4264](https://arxiv.org/abs/0705.4264).
- [6] J. Wei and E. Norman, “Lie algebraic solution of linear differential equations”, *Journal of Mathematical Physics* **4** (1963), no. 4, 575–581.
- [7] D. J. Gross and F. Wilczek, “Ultraviolet Behavior of Non-Abelian Gauge Theories”, *Phys. Rev. Lett.* **30** (Jun, 1973) 1343–1346, doi:[10.1103/PhysRevLett.30.1343](https://doi.org/10.1103/PhysRevLett.30.1343).
- [8] M. Cacciari, G. P. Salam, and G. Soyez, “The anti- $k_t$  jet clustering algorithm”, *JHEP* **04** (2008) 063.
- [9] S. Dawson, “Introduction to electroweak symmetry breaking”, in *Proceedings, Summer School in High-energy physics and cosmology: Trieste, Italy, June 29-July 17, 1998*, pp. 1–83. 1998. [arXiv:hep-ph/9901280](https://arxiv.org/abs/hep-ph/9901280).
- [10] Super-Kamiokande Collaboration, “Evidence for oscillation of atmospheric neutrinos”, *Phys. Rev. Lett.* **81** (1998) 1562–1567,

- doi:[10.1103/PhysRevLett.81.1562](https://doi.org/10.1103/PhysRevLett.81.1562), arXiv:[hep-ex/9807003](https://arxiv.org/abs/hep-ex/9807003).
- [11] R. N. Mohapatra and A. Y. Smirnov, “Neutrino Mass and New Physics”, *Ann. Rev. Nucl. Part. Sci.* **56** (2006) 569–628,  
doi:[10.1146/annurev.nucl.56.080805.140534](https://doi.org/10.1146/annurev.nucl.56.080805.140534), arXiv:[hep-ph/0603118](https://arxiv.org/abs/hep-ph/0603118).
- [12] A. Santamaria, “Masses, mixings, Yukawa couplings and their symmetries”, *Phys. Lett.* **B305** (1993) 90–97, doi:[10.1016/0370-2693\(93\)91110-9](https://doi.org/10.1016/0370-2693(93)91110-9), arXiv:[hep-ph/9302301](https://arxiv.org/abs/hep-ph/9302301).
- [13] A. Padilla, “Lectures on the Cosmological Constant Problem”, arXiv:[1502.05296](https://arxiv.org/abs/1502.05296).
- [14] F. Quevedo, S. Krippendorf, and O. Schlotterer, “Cambridge Lectures on Supersymmetry and Extra Dimensions”, arXiv:[1011.1491](https://arxiv.org/abs/1011.1491).
- [15] S. R. Coleman and J. Mandula, “All Possible Symmetries of the S Matrix”, *Phys. Rev.* **159** (1967) 1251–1256, doi:[10.1103/PhysRev.159.1251](https://doi.org/10.1103/PhysRev.159.1251).
- [16] S. P. Martin, “A Supersymmetry primer”, doi:[10.1142/9789812839657\\_0001](https://doi.org/10.1142/9789812839657_0001), doi:[10.1142/9789814307505\\_0001](https://doi.org/10.1142/9789814307505_0001), arXiv:[hep-ph/9709356](https://arxiv.org/abs/hep-ph/9709356).
- [17] A. Djouadi, “The Higgs particles in the MSSM”, in *Proceedings, Ecole de GIF, LAPP Annecy, France*. 2001.
- [18] Super-Kamiokande Collaboration, “Search for proton decay via  $p \rightarrow e^+ \pi^0$  and  $p \rightarrow \mu^+ \pi^0$  in 0.31 megaton years exposure of the Super-Kamiokande water Cherenkov detector”, *Phys. Rev.* **D95** (2017), no. 1, 012004, doi:[10.1103/PhysRevD.95.012004](https://doi.org/10.1103/PhysRevD.95.012004), arXiv:[1610.03597](https://arxiv.org/abs/1610.03597).
- [19] M. Kramer, A. Kulesza, R. van der Leeuw et al., “Supersymmetry production cross sections in  $pp$  collisions at  $\sqrt{s} = 7$  TeV”, arXiv:[1206.2892](https://arxiv.org/abs/1206.2892).
- [20] D. Ghosh, M. Guchait, S. Raychaudhuri et al., “How Constrained is the cMSSM?”, *Phys. Rev.* **D86** (2012) 055007, doi:[10.1103/PhysRevD.86.055007](https://doi.org/10.1103/PhysRevD.86.055007), arXiv:[1205.2283](https://arxiv.org/abs/1205.2283).
- [21] CMS Collaboration, “Interpretation of Searches for Supersymmetry with simplified Models”, *Phys. Rev.* **D88** (2013), no. 5, 052017, doi:[10.1103/PhysRevD.88.052017](https://doi.org/10.1103/PhysRevD.88.052017), arXiv:[1301.2175](https://arxiv.org/abs/1301.2175).

- [22] M. Papucci, K. Sakurai, A. Weiler et al., “Fastlim: a fast LHC limit calculator”, *Eur. Phys. J.* **C74** (2014), no. 11, 3163, doi:10.1140/epjc/s10052-014-3163-1, arXiv:1402.0492.
- [23] A. Askew, “Searches for supersymmetry with the CMS detector at the LHC”, in *Journal of Physics: Conference Series*, volume 455, p. 012022, IOP Publishing. 2013.
- [24] CMS Collaboration, “Projected Performance of an Upgraded CMS Detector at the LHC and HL-LHC: Contribution to the Snowmass Process”, in *Proceedings, Community Summer Study 2013: Snowmass on the Mississippi (CSS2013): Minneapolis, MN, USA, July 29-August 6, 2013*. 2013. arXiv:1307.7135.
- [25] ALICE Collaboration, “The ALICE experiment at the CERN LHC”, *JINST* **3** (2008) S08002, doi:10.1088/1748-0221/3/08/S08002.
- [26] ATLAS Collaboration, “The ATLAS Experiment at the CERN Large Hadron Collider”, *JINST* **3** (2008) S08003, doi:10.1088/1748-0221/3/08/S08003.
- [27] CMS Collaboration, “The CMS experiment at the CERN LHC”, *Journal of Instrumentation* **3** (2008), no. 08, S08004.
- [28] LHCb Collaboration, “The LHCb Detector at the LHC”, *JINST* **3** (2008) S08005, doi:10.1088/1748-0221/3/08/S08005.
- [29] L. Evans and P. Bryant, “LHC Machine”, *Journal of Instrumentation* **3** (2008), no. 08, S08001.
- [30] CMS Collaboration, “Observation of a new boson at a mass of 125 GeV with the CMS experiment at the LHC”, *Phys. Lett.* **B716** (2012) 30–61, doi:10.1016/j.physletb.2012.08.021, arXiv:1207.7235.
- [31] ATLAS Collaboration, “Observation of a new particle in the search for the Standard Model Higgs boson with the ATLAS detector at the LHC”, *Phys. Lett.* **B716** (2012) 1–29, doi:10.1016/j.physletb.2012.08.020, arXiv:1207.7214.
- [32] CMS Collaboration, “CMS Luminosity Measurements for the 2016 Data Taking Period”, Technical Report CMS-PAS-LUM-17-001, CERN, Geneva, (2017).
- [33] CMS Collaboration, “Interactive Slice of the CMS detector”. CMS Document 4172-v2.

- 
- [34] CMS Collaboration, “Operation and performance of the CMS tracker”, *JINST* **9** (2014) C03005, doi:10.1088/1748-0221/9/03/C03005, arXiv:1402.0675.
  - [35] CMS Collaboration, C. Collaboration, “CMS, tracker technical design report”. 1998.
  - [36] V. Halyo, P. LeGresley, and P. Lujan, “Massively Parallel Computing and the Search for Jets and Black Holes at the LHC”, *Nucl. Instrum. Meth.* **A744** (2014) 54–60, doi:10.1016/j.nima.2014.01.038, arXiv:1309.6275.
  - [37] CMS Collaboration, “The CMS electromagnetic calorimeter project: Technical Design Report”. Technical Design Report CMS. CERN, Geneva, 1997.
  - [38] CMS Collaboration, “Energy Calibration and Resolution of the CMS Electromagnetic Calorimeter in  $pp$  Collisions at  $\sqrt{s} = 7$  TeV”, *JINST* **8** (2013) P09009, doi:10.1088/1748-0221/8/09/P09009, arXiv:1306.2016.
  - [39] A. Benaglia, “The CMS ECAL performance with examples”, *Journal of Instrumentation* **9** (2014), no. 02, C02008.
  - [40] CMS Collaboration, “The CMS hadron calorimeter project: Technical Design Report”. Technical Design Report CMS. CERN, Geneva, 1997.
  - [41] CMS Collaboration, “The CMS barrel calorimeter response to particle beams from 2 to 350 GeV”, *The European Physical Journal C* **60** (2009), no. 3, 359–373, doi:10.1140/epjc/s10052-009-0959-5.
  - [42] CMS Collaboration, “The CMS muon project: Technical Design Report”. Technical Design Report CMS. CERN, Geneva, 1997.
  - [43] CMS Collaboration, “The performance of the CMS muon detector in proton-proton collisions at  $\sqrt{s} = 7$  TeV at the LHC”, *JINST* **8** (2013) P11002, doi:10.1088/1748-0221/8/11/P11002, arXiv:1306.6905.
  - [44] CMS Collaboration, “CMS The TriDAS Project: Technical Design Report, Volume 2: Data Acquisition and High-Level Trigger. CMS trigger and data-acquisition project”. Technical Design Report CMS. CERN, Geneva, 2002.
  - [45] D. Trocino, “The CMS High Level Trigger”, *Journal of Physics: Conference Series* **513** (2014), no. 1, 012036.

- [46] C. Eck, J. Knobloch, L. Robertson et al., “LHC computing Grid: Technical Design Report. Version 1.06 (20 Jun 2005)”. Technical Design Report LCG. CERN, Geneva, 2005.
- [47] A. Buckley et al., “General-purpose event generators for LHC physics”, *Phys. Rept.* **504** (2011) 145–233, doi:10.1016/j.physrep.2011.03.005, arXiv:1101.2599.
- [48] A. D. Martin, W. J. Stirling, R. S. Thorne et al., “Parton distributions for the LHC”, *Eur. Phys. J.* **C63** (2009) 189–285, doi:10.1140/epjc/s10052-009-1072-5, arXiv:0901.0002.
- [49] T. Sjöstrand, S. Mrenna, and P. Skands, “A brief introduction to PYTHIA 8.1”, *Comput. Phys. Commun.* **178** (2008), no. 11, 852 – 867, doi:/10.1016/j.cpc.2008.01.036.
- [50] J. Alwall, M. Herquet, F. Maltoni et al., “MadGraph 5 : Going Beyond”, *JHEP* **06** (2011) 128, doi:10.1007/JHEP06(2011)128, arXiv:1106.0522.
- [51] G. Corcella, I. G. Knowles, G. Marchesini et al., “HERWIG 6: An Event generator for hadron emission reactions with interfering gluons (including supersymmetric processes)”, *JHEP* **01** (2001) 010, doi:10.1088/1126-6708/2001/01/010, arXiv:hep-ph/0011363.
- [52] N. Davidson, G. Nanava, T. Przedzinski et al., “Universal Interface of TAUOLA Technical and Physics Documentation”, *Comput. Phys. Commun.* **183** (2012) 821–843, doi:10.1016/j.cpc.2011.12.009, arXiv:1002.0543.
- [53] W. Beenakker, R. Hopker, and M. Spira, “PROSPINO: A Program for the production of supersymmetric particles in next-to-leading order QCD”, arXiv:hep-ph/9611232.
- [54] S. Agostinelli, J. Allison, K. Amako et al., “Geant4, a simulation toolkit”, *Nuclear Instruments and Methods in Physics Research Section A: Accelerators, Spectrometers, Detectors and Associated Equipment* **506** (2003), no. 3, 250 – 303, doi:[http://dx.doi.org/10.1016/S0168-9002\(03\)01368-8](http://dx.doi.org/10.1016/S0168-9002(03)01368-8).
- [55] A. Giammanco, “The fast simulation of the CMS experiment”, in *Journal of Physics: Conference Series*, volume 513, p. 022012, IOP Publishing. 2014.

- [56] CMS Collaboration, “CMS Tracking Performance Results from early LHC Operation”, *Eur. Phys. J.* **C70** (2010), no. CERN-PH-EP-2010-019, CMS-TRK-10-001, 1165–1192, doi:10.1140/epjc/s10052-010-1491-3, arXiv:1007.1988.
- [57] CMS Collaboration, “Measurement of Tracking Efficiency”, Technical Report CMS-PAS-TRK-10-002, CERN, 2010. Geneva, (2010).
- [58] CMS Collaboration, “Description and performance of track and primary-vertex reconstruction with the CMS tracker”, *JINST* **9** (2014), no. 10, P10009, doi:10.1088/1748-0221/9/10/P10009, arXiv:1405.6569.
- [59] R. Fruehwirth, W. Waltenberger, and P. Vanlaer, “Adaptive Vertex Fitting”, Technical Report CMS-NOTE-2007-008, CERN, Geneva, (Mar, 2007).
- [60] CMS Collaboration, “Tracking and Primary Vertex Results in First 7 TeV Collisions”, Technical Report CMS-PAS-TRK-10-005, CERN, 2010. Geneva, (2010).
- [61] HCAL Calibration Group Collaboration, O. Kodolova, “HCAL calibration in high luminosity environment”, in *Proceedings, CMS Workshop: Perspectives on Physics and on CMS at Very High Luminosity, HL-LHC: Alushta, Crimea, Ukraine, May 28–31, 2012*, pp. 169–175. 2013.
- [62] CMS Collaboration, “Reconstruction and identification of  $\tau$  lepton decays to hadrons and  $\nu_\tau$  at CMS”, Technical Report arXiv:1510.07488. CMS-TAU-14-001. CERN-PH-EP-2015-261, CERN, Geneva, (Oct, 2015).
- [63] CMS Collaboration, “Electron and photon measurement with the CMS detector”, *Conf. Proc.* **C0908171** (2009) 448–450, doi:10.3204/DESY-PROC-2010-04/P16.
- [64] CMS Collaboration, “Performance of CMS muon reconstruction in  $pp$  collision events at  $\sqrt{s} = 7$  TeV”, *JINST* **7** (2012) P10002, doi:10.1088/1748-0221/7/10/P10002, arXiv:1206.4071.
- [65] CMS Collaboration, “Performance of CMS muon reconstruction in cosmic-ray events”, *Journal of Instrumentation* **5** (2010), no. 03, T03022.
- [66] CMS Collaboration, F. Beaudette, “The CMS Particle Flow Algorithm”, in *Proceedings, International Conference on Calorimetry for the High Energy Frontier (CHEF 2013): Paris, France, April 22-25, 2013*, pp. 295–304. 2013.

- arXiv:1401.8155.
- [67] CMS Collaboration, “Particle-Flow Event Reconstruction in CMS and Performance for Jets, Taus, and MET”, Technical Report CMS-PAS-PFT-09-001, CERN, 2009. Geneva, (Apr, 2009).
  - [68] M. Cacciari, G. P. Salam, and G. Soyez, “FastJet User Manual”, *Eur. Phys. J.* **C72** (2012) 1896, doi:10.1140/epjc/s10052-012-1896-2, arXiv:1111.6097.
  - [69] M. Cacciari and G. P. Salam, “Pileup subtraction using jet areas”, *Phys. Lett.* **B659** (2008) 119–126, doi:10.1016/j.physletb.2007.09.077, arXiv:0707.1378.
  - [70] J. Tseng and H. Evans, “Sequential recombination algorithm for jet clustering and background subtraction”, *Phys. Rev.* **D88** (2013) 014044, doi:10.1103/PhysRevD.88.014044, arXiv:1304.1025.
  - [71] CMS Collaboration, “Determination of jet energy calibration and transverse momentum resolution in CMS”, *JINST* **6** (2011) 11002, doi:10.1088/1748-0221/6/11/P11002, arXiv:1107.4277.
  - [72] A. Santocchia, “Jet energy correction in CMS”, in *2009 IEEE Nuclear Science Symposium Conference Record (NSS/MIC)*, pp. 2299–2307. Oct, 2009. doi:10.1109/NSSMIC.2009.5402040.
  - [73] CMS Collaboration, “Jet energy scale and resolution performances with 13TeV data”, Technical Report CMS-DP-2016-020, CERN, Geneva, (June, 2016).
  - [74] CMS Collaboration, “Identification of b quark jets at the CMS Experiment in the LHC Run 2”, Technical Report CMS-PAS-BTV-15-001, CERN, Geneva, (2016).
  - [75] CMS Collaboration, “Performance of b-Tagging Algorithms in Proton Collisions at 13 TeV using the 2016 Dataset”, Technical Report CMS-DP-2016-042, (Jul, 2016).
  - [76] CMS Collaboration, “Performance of missing energy reconstruction in 13 TeV pp collision data using the CMS detector”, Technical Report CMS-PAS-JME-16-004, CERN, Geneva, (2016).
  - [77] CMS Collaboration, “Performance and upgrade of the CMS electromagnetic calorimeter trigger for Run II”, Technical Report CMS-CR-2014-068, CERN, Geneva, (May, 2014).

- [78] CMS Collaboration, “The CMS Level-1 Tau algorithm for the LHC Run II”, Technical Report CMS-CR-2015-214, CERN, Geneva, (Oct, 2015).
- [79] M. Jeitler, J. Lingemann, D. Rabady et al., “Upgrade of the CMS Global Muon Trigger”, *IEEE Transactions on Nuclear Science* **62** (June, 2015) 1104–1109, doi:10.1109/TNS.2015.2435060.
- [80] A. Tapper, J. Brooke, C. Foudas et al., “Commissioning and performance of the CMS Global Calorimeter Trigger”, in *2008 IEEE Nuclear Science Symposium Conference Record*, pp. 1871–1873. Oct, 2008.  
doi:10.1109/NSSMIC.2008.4774755.
- [81] CMS Collaboration, “Run 2 Upgrades to the CMS Level-1 Calorimeter Trigger”, *JINST* **11** (2016), no. 01, C01051, doi:10.1088/1748-0221/11/01/C01051, arXiv:1511.05855.
- [82] G. Hall, D. Newbold, M. Pesaresi et al., “A time-multiplexed track-trigger architecture for CMS”, *Journal of Instrumentation* **9** (2014), no. 10, C10034.
- [83] K. Compton, S. Dasu, A. Farmahini-Farahani et al., “The MP7 and CTP-6: multi-hundred Gbps processing boards for calorimeter trigger upgrades at CMS”, *Journal of Instrumentation* **7** (2012), no. 12, C12024.
- [84] M. Baber, “Search for supersymmetry in the first  $\sqrt(s) = 13$  TeV pp-collisions using the  $\alpha_T$  variable with the CMS detector”. PhD thesis, Imperial College, London, 2016. Presented 2016.
- [85] M. Cacciari, J. Rojo, G. P. Salam et al., “Jet Reconstruction in Heavy Ion Collisions”, *Eur. Phys. J.* **C71** (2011) 1539,  
doi:10.1140/epjc/s10052-011-1539-z, arXiv:1010.1759.
- [86] J. Brooke, B. Mathias, A. Tapper, N. Wardle, “Calibration and Performance of the Jets and Energy Sums in the Level-1 Trigger”, Technical Report CMS-IN-2013/006, (2013).
- [87] CMS Collaboration, “Level-1 Jets and Sums Trigger Performance”, Technical Report CMS-DP-2016-034, (Jun, 2016).
- [88] CMS Collaboration, “Search for supersymmetry in hadronic final states with missing transverse energy using the variables  $\alpha_T$  and b-quark multiplicity in pp collisions at  $\sqrt{s} = 8$  TeV”, *Eur. Phys. J.* **C73** (2013), no. 9, 2568,

- doi:10.1140/epjc/s10052-013-2568-6, arXiv:1303.2985.
- [89] CMS Collaboration, “Search for supersymmetry in final states with missing transverse energy and 0, 1, 2, or at least 3 b-quark jets in 7 TeV pp collisions using the variable alphaT”, *JHEP* **01** (2013) 077, doi:10.1007/JHEP01(2013)077, arXiv:1210.8115.
- [90] CMS Collaboration, “Search for Supersymmetry at the LHC in Events with Jets and Missing Transverse Energy”, *Phys. Rev. Lett.* **107** (2011) 221804, doi:10.1103/PhysRevLett.107.221804, arXiv:1109.2352.
- [91] V. Khachatryan, “Search for supersymmetry in pp collisions at 7 TeV in events with jets and missing transverse energy”, *Physics Letters B* **698** (2011), no. 3, 196 – 218, doi:<http://dx.doi.org/10.1016/j.physletb.2011.03.021>.
- [92] ATLAS Collaboration, “Measurement of the Inelastic Proton-Proton Cross Section at  $\sqrt{s} = 13$  TeV with the ATLAS Detector at the LHC”, *Phys. Rev. Lett.* **117** (2016), no. 18, 182002, doi:10.1103/PhysRevLett.117.182002, arXiv:1606.02625.
- [93] CMS Collaboration, K. Stifter, “The CMS Beam Halo Monitor Detector System”, in *Proceedings, Meeting of the APS Division of Particles and Fields (DPF 2015): Ann Arbor, Michigan, USA, 4-8 Aug 2015*. 2015. arXiv:1511.00264.
- [94] L. Randall and D. Tucker-Smith, “Dijet Searches for Supersymmetry at the LHC”, *Phys. Rev. Lett.* **101** (2008) 221803, doi:10.1103/PhysRevLett.101.221803, arXiv:0806.1049.
- [95] CMS Collaboration, “Performance of CMS muon reconstruction in  $pp$  collision events at  $\sqrt{s} = 7$  TeV”, *JINST* **7** (2012) P10002, doi:10.1088/1748-0221/7/10/P10002, arXiv:1206.4071.
- [96] J. Alwall, R. Frederix, S. Frixione et al., “The automated computation of tree-level and next-to-leading order differential cross sections, and their matching to parton shower simulations”, *JHEP* **07** (2014) 079, doi:10.1007/JHEP07(2014)079, arXiv:1405.0301.
- [97] S. Alioli, P. Nason, C. Oleari et al., “A general framework for implementing NLO calculations in shower Monte Carlo programs: the POWHEG BOX”, *JHEP* **06** (2010) 043, doi:10.1007/JHEP06(2010)043, arXiv:1002.2581.

- [98] C. Borschensky, M. Kramer, A. Kulesza et al., “Squark and gluino production cross sections in pp collisions at  $\sqrt{s} = 13, 14, 33$  and  $100$  TeV”, *Eur. Phys. J.* **C74** (2014), no. 12, 3174, doi:10.1140/epjc/s10052-014-3174-y, arXiv:1407.5066.
- [99] CMS Collaboration, “Measurement of differential cross sections for top quark pair production using the lepton+jets final state in proton-proton collisions at  $13$  TeV”, *Submitted to: Phys. Rev. D* (2016) arXiv:1610.04191.
- [100] Z. Bern, G. Diana, L. J. Dixon et al., “Left-handed  $W$  bosons at the LHC”, *Phys. Rev. D* **84** (Aug, 2011) 034008, doi:10.1103/PhysRevD.84.034008.
- [101] J. Cohen, P. Cohen, S. G. West et al., “Applied multiple regression/correlation analysis for the behavioral sciences”. Routledge, 2013.
- [102] CERN, “PHYSTAT 2011 Workshop on Statistical Issues Related to Discovery Claims in Search Experiments and Unfolding”. CERN, Geneva, (2011).
- [103] G. Cowan, K. Cranmer, E. Gross et al., “Asymptotic formulae for likelihood-based tests of new physics”, *Eur. Phys. J.* **C71** (2011) 1554, doi:10.1140/epjc/s10052-011-1554-0, arXiv:1007.1727.
- [104] DELPHES 3 Collaboration, “DELPHES 3, A modular framework for fast simulation of a generic collider experiment”, *JHEP* **02** (2014) 057, doi:10.1007/JHEP02(2014)057, arXiv:1307.6346.
- [105] M. Drees, H. Dreiner, D. Schmeier et al., “CheckMATE: Confronting your Favourite New Physics Model with LHC Data”, *Comput. Phys. Commun.* **187** (2015) 227–265, doi:10.1016/j.cpc.2014.10.018, arXiv:1312.2591.
- [106] K. J. de Vries et al., “The pMSSM10 after LHC Run 1”, *Eur. Phys. J.* **C75** (2015), no. 9, 422, doi:10.1140/epjc/s10052-015-3599-y.
- [107] CMS Collaboration, “Simplified likelihood for the re-interpretation of public CMS results”, Technical Report CMS-NOTE-2017-001. CERN-CMS-NOTE-2017-001, CERN, Geneva, (Jan, 2017).
- [108] CMS Collaboration, “A search for new phenomena in pp collisions at  $\sqrt{s} = 13$  TeV in final states with missing transverse momentum and at least one jet using the  $\alpha_T$  variable”, *The European Physical Journal C* **77** (2017), no. 5, 294, doi:10.1140/epjc/s10052-017-4787-8.